Search for Supersymmetry at the Tevatron using the Trilepton signature

BY SOURABH DUBE

A dissertation submitted to the

Graduate School—New Brunswick

Rutgers, The State University of New Jersey

in partial fulfillment of the requirements

for the degree of

Doctor of Philosophy

Graduate Program in Physics and Astronomy

Written under the direction of

Professor Sunil Somalwar

and approved by

New Brunswick, New Jersey

October, 2008

ABSTRACT OF THE DISSERTATION

Search for Supersymmetry at the Tevatron using the Trilepton signature

by Sourabh Dube

Dissertation Director: Professor Sunil Somalwar

This dissertation describes a search for the associated production of the supersymmetric particles, the chargino and the neutralino, through their R-parity conserving decays to three leptons and missing energy. This search is carried out using the data collected at the CDF experiment at the Tevatron $\sqrt{s} = 1.96$ TeV $p\bar{p}$ collider at Fermilab. The results are obtained by combining five independent channels with varying signal to background ratio. Overall, a total of 6.4 ± 1.1 background events from standard model processes and 11.4 ± 1.1 signal events for a particular choice of mSUGRA model parameters are expected. The observation of 7 events in data is consistent with the standard model background expectation, and the mSUGRA model is constrained. Limits are set on the cross section of Chargino-Neutralino pair production, and a limit on the mass of the chargino is extracted. A method of obtaining model-independent results is also discussed.

Acknowledgements

I feel the deepest respect for my advisor Sunil Somalwar. I want to thank him for being a friend, a philosopher, and a guide in the truest sense of those words. Without him, I would not love particle physics; it is as simple as that.

Alex and Julian have been the best fellow-culprits I could have hoped for; smart and hard-working. This analysis has a lot of their sweat and toil as well. Thanks guys, I wish you the very best.

I want to thank the entire Rutgers group (past and present): The faculty members Tom Devlin, Terry Watts, Amit Lath, Eva Halkiadakis, Scott Thomas and Matt Strassler for their constant encouragement and guidance, the postdocs Fedor Ratnikov, and Anton Anastassov for the time they spent on even the most mundane queries on my part, and the students Dongwook Jang, Zongru Wan, Paul Dituro, Daryl Hare, and Jared Yamaoka for being there for everything else. Jared, thanks for the thesis template, you know how much it helped! I would like to especially thank John Zhou, he held my hand as I took my baby steps in this field and he taught me to walk on my own. Thanks also to Pieter Jacques, John Doroshenko, and Bob Stone who made sure that the computers work, the CAF runs smoothly and helped me with the day-to-day questions to which I wouldn't know where to find answers. Thanks to Nancy DeHaan for shielding me from the administrative quicksands.

The trilepton analysis would not be any fun without Anadi, Else, Giulia, John, and Vadim. Working with them ensured that even the most annoying tasks were enjoyable. I want to thank them for all their guidance, scripts, code, and conversations. The convenors at CDF also deserve a special mention; Ben, Chris, Dave and Monica. They taught me to think carefully, do a good analysis, give a good talk and much more.

Tim Koeth and Rouven Essig helped to make Batavia and Piscataway as much of a home as Pune is; for that I'm grateful. Between them, I'm sure they will cover the best of experiment and theory and it is a privilege to know them.

The last two years have been made special by Aditya and Sarika, Amit and Diptee, Mandar and Shreya, Pankaj and Prajakta, Shreedhar and Meenal, and Salil. The good times we have had together has made sure that the evenings I had for my own were well spent. They have been a sounding board for my wildest ideas, and they have been patient with me. Consider this a payback!

I want to thank Mrs. Dattagupta, and Mrs. Honwad who made sure that my instinct to question and understand was nurtured; they are the first teachers who mattered. I am grateful to them.

I can never thank the "moonriders" enough; Anand, Harshal, Nikhil (and Richa), Raviraj, Rohit, Saurabh, Shrirang, and Ketan. They make sure that I remember to value some things more than ntuples and limits. They are the best, and I'm incredibly fortunate to have them. I have missed their daily company these six years, but they have made sure I stayed true.

Finally I want to thank my parents, Koustubh, and Shraddha, for everything; no words will suffice to express my feelings for them. They are the wind beneath my wings.

For

Shi, Shu,

& Shr

and fulfilling dreams

Table of Contents

List of Tables

List of Figures

Chapter 1

Introduction : Experimental High Energy Physics

At its simplest level, high energy physics (or HEP[1] in the business) deals with answering "What is the world around us made of?". A related and equally important question is about how the world around us came to be the way it is. Answering these questions however, is far from simple.

Identifying the constituents of matter and the way they interact with each other forms the core of this field. These studies can be divided into theoretical and experimental ones, with the theorists dealing primarily with developing new theories and models to explain phenomena in nature and the experimentalists dealing with either confirming, or refuting these theories and models. Of course, it is not as black and white as that. For example, certain phenomena are observed in experiments, which must be explained and incorporated by theory (such as β decay) and sometimes theory will predict effects much before experiment verifies it (existence of antiparticles).

At present, a wonderful collection of theories known as the standard model describes all the known elementary particles and their interactions. This model has been tested to a high degree of precision by various experiments. However, as we shall see, it does not appear to be complete. There are various questions that the Standard Model fails to address. Supersymmetry is a possible candidate theory for addressing some of the significant questions. Supersymmetry is a proposed symmetry between fermions and bosons and in Chapter 2 we shall discuss the idea and implications of such a symmetry.

[1]The field is replete with acronyms, and they are used fast and furiously. Best to get used to acronyms right at the beginning.

This dissertation is the search for the associated production of two supersymmetric particles, the chargino($\widetilde{\chi}_1^{\pm}$) and the neutralino($\widetilde{\chi}_2^0$), when they decay to leptons. In Chapter 3, I shall describe the tools used for this search, the Tevatron accelerator and the CDF detector, following which we will discuss the specifics of the analysis in Chapter 4. In Chapter 7, I shall present the results from this search for the chargino and the neutralino.

To begin, let us discuss a simple, yet powerful equation in particle physics.

$$N = \mathcal{L} \times \sigma \times \mathrm{BR} \times A \times \epsilon \tag{1.1}$$

where N is the number of events expected to be observed, $\mathcal{L}$ is the integrated luminosity (as described below), σ is the process cross section, BR is the branching ratio to the channel of interest, A is the (geometric) acceptance, and ϵ is the efficiency. The integrated luminosity $\mathcal{L}$ is a measure of amount of data collected, and it is measured in units of inverse cross section. The units used here are usually inverse picobarns pb^{-1}, where 1 barn = 10^{-28} m^2. For the specific case of the chargino-neutralino search presented in this dissertation, N will the number of $\widetilde{\chi}_1^{\pm}\widetilde{\chi}_2^0$ events expected to be seen in data in the $3l$ channel if

1. $\mathcal{L}$ is the amount of data,
2. σ is the cross section for $p\bar{p} \to \widetilde{\chi}_1^{\pm}\widetilde{\chi}_2^0$,
3. BR is the branching ratio of $\widetilde{\chi}_1^{\pm}\widetilde{\chi}_2^0 \to 3l$,
4. A is the geometric acceptance of the produced events in the detector, and
5. ϵ is the efficiency of selecting the produced events.

The σ and BR are obtained from theoretical predictions. A is accounted for by making the same geometric requirements in the simulated samples as in the data, and ϵ is measured using independent data samples. The amount of data used here is 2 fb^{-1} collected by the CDF experiment at the Tevatron $\sqrt{s} = 1.96$ TeV $p\bar{p}$ collider. The other details will become clear as we work through the following chapters.

Chapter 2

The Standard Model and Supersymmetry

2.1 The Standard Model

The standard model (SM) is a quantum field theory that emerged in the 1970's out of the work of Glashow, Weinberg and Salam. It describes three fundamental forces of nature (the electromagnetic, the weak and the strong) and the particles that form matter, and is a gauge theory based on $SU(3) \times SU(2) \times U(1)$. The SM has been extremely successful at describing phenomena up to the scale of the top quark (~ 172 GeV/c^2); a large number of experimental results confirm SM predictions.

The discussion here follows Ref. [2]. The particle content of the SM is summarized in Fig 2.1. The particles are split in to those that form matter, the fermions; and those which describe the interactions, the bosons. The fermions are further split in to two, the quarks and the leptons based on the interactions in which they take part. The leptons do not take part in strong interactions, but interact via the electroweak interactions. The quarks interact via strong and electroweak interactions. The first generation of fermions, the electron and electron neutrino, the up and down quarks make up all the stable matter in the universe. The bosons are the mediators of the different interactions. The photon mediates the electromagnetic interaction, the $W^{\pm}$ and Z bosons mediate the weak interaction, and the gluon mediates the strong interaction. Some properties of the particles in the SM are summarized in Table 2.2 for fermions and Table 2.1 for bosons.

The SM theory is constructed under the expectation of local gauge invariance, i.e it is

Name	Symbol	Charge	Mass (MeV)
Photon	γ	0	0
	$W^{\pm}$	± 1	80.2×10^3
	Z	0	91.2×10^3
gluon	g	0	0
Higgs	h	0	?

Table 2.1: The table shows some properties of the standard model bosons. The Higgs boson is undiscovered so far.

Name	Symbol	Baryon Number B	Lepton Number L	Charge	Mass (MeV)
Leptons	l				
electron	e	0	1	-1	0.511
electron neutrino	ν_e	0	1	0	$< 2 \times 10^{-6}$
muon	μ	0	1	-1	106
muon neutrino	ν_μ	0	1	0	$< 2 \times 10^{-6}$
tau	τ	0	1	-1	1777
tau neutrino	ν_τ	0	1	0	$< 2 \times 10^{-6}$
Quarks	q				
up	u	1	0	$+2/3$	1.5 to 3.3
down	d	1	0	$-1/3$	3.5 to 6
charm	c	1	0	$+2/3$	1270
strange	s	1	0	$-1/3$	104
top	t	1	0	$+2/3$	1.71×10^5
bottom	b	1	0	$-1/3$	4.2×10^3

Table 2.2: The table shows some properties of the standard model fermions. Each particle has spin 1/2.

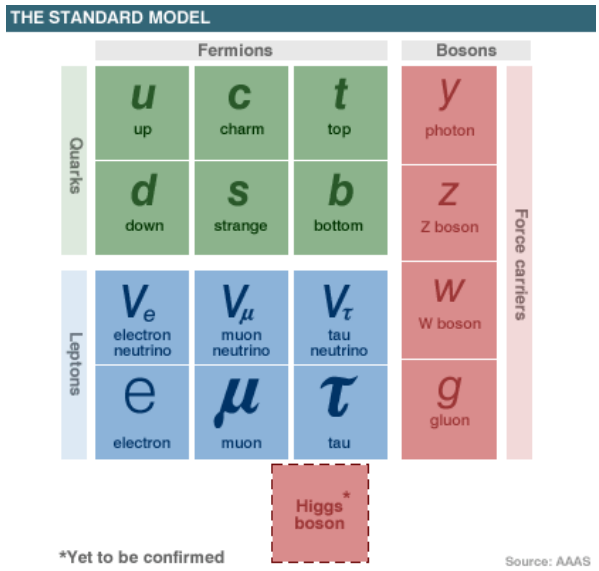

Figure 2.1: The figure shows the different particles in the standard model. The Higgs boson is undiscovered so far.

a theory which is symmetric under gauge transformations of the form

$$\psi(x) \to e^{i\alpha(x)}\psi(x) \tag{2.1}$$

for the $U(1)$ abelian group[1]. Imposing this invariance for the $U(1)$ group which represents electromagnetic interactions requires the covariant derivative to replace ∂_μ in the Lagrangian. The covariant derivative is defined as

$$D_\mu \equiv \partial_\mu - ieA_\mu \tag{2.2}$$

where A_μ is a vector field which transforms as

$$A_\mu \to A_\mu + \frac{1}{e}\partial_\mu \alpha \tag{2.3}$$

It follows that this invariance is only possible if the new field A_μ (understood as the physical photon field) is massless and the Lagrangian has no terms such as $\frac{1}{2}m^2 A_\mu A^\mu$. Similar arguments follow for the non-abelian $SU(3)$ group on which the structure of quantum chromodynamics is based; the gluon must also be massless.

[1]The transformations for $SU(3)$ and $SU(2)$ are slightly different.

However, the bosons governing the weak interaction, the $W^{\pm}, Z$ are massive. Mass terms such as $M^2 W_\mu W^\mu$ can be introduced, but this leaves a theory which is unrenormalizable and thus meaningless.

There is a way that allows the local gauge invariance to be maintained, while still generating masses for the W, Z bosons. This is the Higgs mechanism. The local gauge symmetry of the $SU(2)$ is spontaneously broken. The resulting massless scalars which occur according to the Goldstone theorem are incorporated in to the degrees of freedom of the gauge particles and give them longitudinal polarization. Consider a potential of the form

$$V(\phi) = \mu^2 \phi^\dagger \phi + \lambda (\phi^\dagger \phi)^2 \tag{2.4}$$

Choosing $\mu^2 < 0$ and $\lambda > 0$ gives two minima of the potential, which are at

$$\pm\sqrt{\frac{-\mu^2}{2\lambda}} \equiv v/\sqrt{2} \tag{2.5}$$

The potential $V(\phi)$ can be considered as the Higgs field, with the ground state chosen such that it spontaneously breaks the $SU(2) \times U(1)$ symmetry, giving three massive states (W, Z bosons) and one massless state (the photon). The vacuum expectation value (vev) v of the Higgs field is determined from the masses of the gauge bosons to be $v = 246$ GeV.

In general, the SM Lagrangian has the following form :

$$\begin{aligned}
\mathcal{L} = &\text{ (boson kinetic energies and self-interactions)} \\
&+ \text{ (fermion kinetic energies and their interactions with the bosons)} \\
&+ \text{ (mass terms for the bosons, Higgs and their couplings)} \\
&+ \text{ (fermion mass terms and their coupling to the Higgs)}
\end{aligned}$$

where the fermion mass terms originate from interactions with the Higgs fields by means of the Yukawa couplings.

2.1.1 Issues with the standard model

Despite the success of the standard model, there remain many unanswered questions in the SM [3, 4]. The unknown origin of electroweak symmetry breaking, the mass hierarchies of particles; the freedom of choice of masses of the fermions themselves, and the absence of description of gravity are some of them.

A notable issue is the "fine-tuning" problem. As described above, v is the vev of the neutral Higgs fields, and it sets the masses of the particles in the SM. At tree level, the minimum of the potential described in Eq. 2.4 is at $|\mu| = v\sqrt{\lambda}$. Since the standard model is renormalizable, finite results are expected at all higher-order (loop) corrections, even if the virtual momenta that are considered go up to ∞. Thus

$$\int^{\Lambda} d^4k f(k, \text{external momenta}) \tag{2.6}$$

must not diverge. In reality, Λ is not expected to be ∞. The SM model is expected to need modification at the Planck scale (10^{19} GeV) where gravitational effects will become important.

The four-boson interaction term in the potential, $(\phi^\dagger\phi)^2$, at the one-loop order gives corrections to the $\phi^\dagger\phi$ term corresponding to Fig. 2.2 which are proportional to

Figure 2.2: Quantum corrections to the Higgs (mass)^2

$$\lambda \int^{\Lambda} d^4k \frac{1}{k^2 - M_H^2} \tag{2.7}$$

This correction diverges. The physical value of μ^2 corrected at the one loop level is given by

$$\mu^2_{phys} = \mu^2 + 4\lambda\Lambda^2 \tag{2.8}$$

which along the with the phenomenological value of $v \approx 246$ GeV, gives $|\mu_{phys}| \approx 246\sqrt{\lambda}$ GeV. To be able to treat the Higgs coupling perturbatively, λ must not be too greater than 1, implying that μ_{phys} is of the order of few hundred GeV.

If $\Lambda \sim 10^{19}$ GeV, then to obtain the correct μ_{phys} value, the Langrangian parameter μ^2 would have to be equally large. It is "unnatural" for the two large terms to cancel and give a small number with the correct value. This fine-tuning of the subtraction to get the correct answer is the fine-tuning or hierarchy problem.

2.2 Supersymmetry

The details of the theoretical framework of supersymmetry (SUSY) and a thorough description of its motivations can be found in Refs. [5, 6, 7]. Consider the Higgs field coupling to a fermion f with mass m_f as shown in Fig. 2.2, with a term in the Lagrangian $-\lambda_f \bar{H}\bar{f}f$[2]. This gives a correction to μ^2 that is proportional to $-|\lambda_f|^2\Lambda^2 + \ldots$. The correction will be very large for large values of Λ^2, which is the scale of new physics. Although quantum corrections to the quark, lepton and gauge boson masses in the SM are not quadratically sensitive, they depend on the vev of the Higgs field, and so are indirectly sensitive to Λ.

Now if there exists a complex scalar S with mass m_S, Fig. 2.2, it couples to the Higgs with a term $-\lambda_S|H|^2|S|^2$. The correction to μ^2 is then given by a terms such as $\lambda_S\Lambda^2 + \ldots$ Studying the two corrections, and the relative minus sign between them, one sees that the fermion and boson loop contributions can (modulo certain conditions) systematically cancel each other, if there existed a symmetry between fermions and bosons. Enter supersymmetry.

Supersymmetry posits the existence of a symmetry between fermions and bosons. A

[2] H is the complex scalar field associated with the neutral part of the SM Higgs field.

supersymmetric transformation generated by the operator Q turns a bosonic state into a fermionic state, and vice versa,

$$Q|\text{Boson}> \;=\; |\text{Fermion}>; \qquad Q|\text{Fermion}> \;=\; |\text{Boson}>$$

$Q, Q^\dagger$ are anticommutating spinors, and are fermionic operators which carry spin angular momentum. The operators satisfy an algebra which looks like

$$\{Q, Q^\dagger\} = P^\mu \tag{2.9}$$

$$\{Q, Q\} = \{Q^\dagger, Q^\dagger\} = 0 \tag{2.10}$$

$$[P^\mu, Q] = [P^\mu, Q^\dagger] = 0 \tag{2.11}$$

where P^μ is the momentum generator, and the spinor indices have been suppressed. Note that supersymmetry is a spacetime symmetry.

The single-particle states of the theory are grouped into supermultiplets, which contain both fermions and bosons. The supersymmetry generators $Q, Q^\dagger$ commute with the generators of gauge transformations and thus all the particles in the same multiplet have the same electric charge, weak isospin and color charge. Moreover all particles in the same supermultiplet also have equal masses.

The simplest supermultiplet consists of one Weyl fermion with two helicity states, and one complex scalar field. This is a chiral supermultiplet. A gauge or vector supermultiplet has a spin-1 vector boson (massless for now), and a massless spin-1/2 Weyl fermion. In a gauge multiplet, the fermions must have the same gauge transformation properties for left-handed and right-handed components.

All SM particles thus have individual superpartners which have the same quantum numbers except spin, which differs by 1/2 unit. The superpartners of the spin-0 partners of the SM quarks and leptons are called squarks and sleptons. Thus the partner of a spin-1/2 electron is a spin-0 selectron. The symbols for the supersymmetric particles are denoted by a tilde. Thus a SM muon, μ, has a superpartner smuon, $\tilde{\mu}$. The names of the fermionic

superpartners of the gauge bosons, or the Higgs boson are constructed by adding a '-ino' after the name. Thus gauginos, higgsino, gluino are superpartners of the gauge bosons, the Higgs boson, and the gluon respectively.

Aside from superpartners of the discovered SM particles, we need two chiral supermultiplets for the Higgs bosons to avoid triangle gauge anomalies. The two supermultiplets have different weak hypercharge $Y = \pm 1/2$. The $Y = 1/2$ has the right Yukawa couplings to give masses to the (charge=2/3) up type quarks, while the $Y = -1/2$ Higgs supermultiplets gives masses to the (charge=$-1/3$) down type quarks.

Superpartners have not been discovered at the same masses as the SM particles. This must mean that if supersymmetry exists, then it is a broken symmetry. For the rest of this chapter, we shall discuss the minimal supersymmetric extension of the standard model (MSSM) and its constrained version mSUGRA.

2.3 MSSM and mSUGRA

The superpotential for the MSSM is given by

$$W_{\text{MSSM}} = \bar{u}\mathbf{y_u}QH_u - \bar{d}\mathbf{y_d}QH_d - \bar{e}\mathbf{y_e}LH_d + \mu H_u H_d \tag{2.12}$$

and supersymmetry breaking is achieved by means of soft supersymmetry breaking terms, i.e. mass terms and couplings with positive mass dimension. H_u,H_d,Q,L,$\bar{u}$,$\bar{d}$, and $\bar{e}$ are the chiral superfields, and $\mathbf{y_u}$, $\mathbf{y_d}$, and $\mathbf{y_e}$ are the dimensionless Yukawa coupling parameters. The $\mathbf{y}$ terms imply Higgs-quark-quark, Higgs-lepton-lepton, squark-Higgsino-quark, and slepton-Higgsino-lepton interactions. The MSSM respects the same $SU(3) \times SU(2) \times U(1)$ gauge symmetries as the SM, and the effective Lagrangian is given by

$$\mathcal{L} = \mathcal{L}_{\text{SUSY}} + \mathcal{L}_{soft} \tag{2.13}$$

where $\mathcal{L}_{\text{SUSY}}$ terms preserve the supersymmetry invariance, and $\mathcal{L}_{soft}$ are soft supersymmetry breaking terms. Tables 2.3 and 2.4 show the chiral and gauge supermultiplets in the MSSM.

Name	Symbol	Spin-0	Spin-1/2	$SU(3)_C, SU(2)_L, U(1)_Y$
squarks, quarks	Q	$(\tilde{u}_L\ \tilde{d}_L)$	$(u_L\ d_L)$	$\mathbf{3}, \mathbf{2}, \frac{1}{6}$
squarks, quarks	$\bar{u}$	$\tilde{u}_R^*$	$u_R^\dagger$	$\bar{\mathbf{3}}, \mathbf{1}, -\frac{2}{3}$
squarks, quarks	$\bar{d}$	$\tilde{d}_R^*$	$u_R^\dagger$	$\bar{\mathbf{3}}, \mathbf{1}, \frac{1}{3}$
sleptons, leptons	L	$(\tilde{\nu}\ \tilde{e}_L)$	$(\nu\ e_L)$	$\mathbf{1}, \mathbf{2}, -\frac{1}{2}$
sleptons, leptons	$\bar{e}$	$\tilde{e}_R^*$	$e_R^\dagger$	$\mathbf{1}, \mathbf{1}, 1$
Higgs, higgsinos	H_u	$(H_u^+\ H_u^0)$	$(\tilde{H}_u^+\ \tilde{H}_u^0)$	$\mathbf{1}, \mathbf{2}, +\frac{1}{2}$
Higgs, higgsinos	H_d	$(H_d^0\ H_d^-)$	$(\tilde{H}_d^0\ \tilde{H}_d^-)$	$\mathbf{1}, \mathbf{2}, -\frac{1}{2}$

Table 2.3: The table shows the chiral supermultiplets in the MSSM ([6]).

After electroweak symmetry breaking, and SUSY breaking, the superpartners of the SM particles are not necessarily mass eigenstates. The most relevant example here is that the electroweak gauginos and the higgsinos mix to give charginos $\tilde{\chi}^{\pm}$'s and neutralinos $\tilde{\chi}^0$'s.

Before we move to discussing mSUGRA and its phenomenology, the last relevant aspect of the MSSM is the definition of R-parity R_p [8]. In the MSSM Lagrangian, terms which violate lepton number and baryon number can be included. Considering the bounds on lifetime of proton decay, these terms would cause a problem for the MSSM. This problem is circumvented by the introduction of a new symmetry called as R-parity, and mutiplicatively conserved quantum number R_p defined for each particle as

$$R_p = (-1)^{3(B-L)+2s} \tag{2.14}$$

where B, L, s are the baryon number, lepton number and spin of the particle respectively. All the SM particles have $R_p = +1$; all superpartners have $R_p = -1$.

Name	Spin-1/2	Spin-0	$SU(3)_C, SU(2)_L, U(1)_Y$
gluino, gluon	$\tilde{g}$	g	$\mathbf{8}, \mathbf{1}, 0$
winos, W boson	$\tilde{W}^{\pm}\ \tilde{W}^0$	$W^{\pm}\ W^0$	$\mathbf{1}, \mathbf{3}, 0$
bino, B boson	$\tilde{B}^0$	B^0	$\mathbf{1}, \mathbf{1}, 0$

Table 2.4: The table shows the gauge supermultiplets in the MSSM ([6]).

The conservation of R_p has important experimental consequences

- At colliders, supersymmetric particles will be produced in even numbers, mostly pairs.
- The lightest supersymmetric particle (LSP) will be stable. If the LSP is weakly

interacting, then it is an attractive candidate for cold dark matter.

- All sparticles aside from the LSP will decay to a final state which contains an odd number of LSP's , usually just one.

2.3.1 mSUGRA

mSUGRA [9] stands for minimal supergravity; a constrained form of the MSSM model. The spontaneous supersymmetry breaking takes place in a "hidden sector" of particles which has no direct couplings to the "visible sector" chiral supermultiplets of the MSSM. The hidden sector communicates to the visible sector by means of gravitational interactions. There are over 100 free parameters in the unconstrained MSSM. Now the soft terms in $\mathcal{L}_{soft}^{\mathrm{MSSM}}$ can be written in terms of just four parameters. All other parameters can them be expressed in terms of these

$$M_3 = M_2 = M_1 = m_{1/2} \tag{2.15}$$

$$\mathbf{m_Q^2} = \mathbf{m_{\bar{u}}^2} = \mathbf{m_{\bar{d}}^2} = \mathbf{m_L^2} = \mathbf{m_{\bar{e}}^2} = m_0^2\mathbf{1};\ m_{H_u}^2 = m_{H_d}^2 = m_0^2 \tag{2.16}$$

where M_3, M_2, M_1 are the gluino, wino and bino mass terms.

$$\mathbf{a_u} = A_0\mathbf{y_u};\quad \mathbf{a_d} = A_0\mathbf{y_d};\quad \mathbf{a_e} = A_0\mathbf{y_e}; \tag{2.17}$$

where the $\mathbf{a}$'s are the trilinear couplings, and the $\mathbf{y}$'s are the Yukawa couplings.

These equations are applied as renormalization group (RG) boundary conditions at the Planck scale M_P. The RG evolution down to the EWK scale then allows the prediction of all masses and couplings in terms of just five parameters, see Fig. 2.3. Usually the boundary conditions are run down from the unification scale of $M_U \approx 2 \times 10^{16}$ GeV (GUT scale). The five parameters are usually taken in mSUGRA to be

- m_0 : a common scalar mass.
- $m_{1/2}$: a common gaugino mass.
- A_0 : a common trilinear coupling value.

- $\tan\beta$: the ratio of the vev's of the two Higgs doublets, $< H_u > / < H_d >$.

- sign(μ) : the sign of the Higgsino mass parameter.

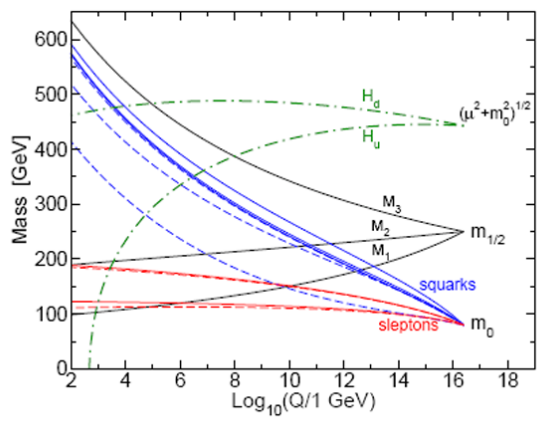

Figure 2.3: Evolution of masses in mSUGRA from GUT scale to EWK scale.

The gauginos are fermions, and consequently their masses are determined primarily by $m_{1/2}$. The sleptons and squarks of the first two generations have masses dependent on m_0 as well as $m_{1/2}$, and the following relations are approximately true

$$m^2_{\tilde{l}_L} \sim m_0^2 + 0.5 \cdot m^2_{1/2}; \quad m^2_{\tilde{l}_R} \sim m_0^2 + 0.15 \cdot m^2_{1/2}; \tag{2.18}$$

$$m^2_{\tilde{q}_L} \sim m_0^2 + 6 \cdot m^2_{1/2}; \quad m^2_{\tilde{q}_R} \sim m_0^2 + 5 \cdot m^2_{1/2}; \tag{2.19}$$

The charginos (two, $\widetilde{\chi}_1^{\pm}$ and $\widetilde{\chi}_2^{\pm}$) are the mass eigenstates of the mixtures of the charged $SU(2)_L$ gauginos and the charged higgsinos. The neutralinos (four, $\widetilde{\chi}_1^0$, $\widetilde{\chi}_2^0$, ...) are mixtures of the bino $\tilde{B}$, the neutral wino $\tilde{W}$, and the two neutral higgsinos. Within mSUGRA, the following relations are approximately true

$$m(\widetilde{\chi}_1^{\pm}) \simeq m(\widetilde{\chi}_2^0) \simeq 2 \cdot m(\widetilde{\chi}_1^0) \tag{2.20}$$

The golden signature for mSUGRA is the "trilepton" signature [10][3], which is described in the next section. Before delving into the phenomenology of the trilepton signature and

[3]The discovery reach for supersymetry at the Tevatron described in this reference is slightly outdated, but the ideas presented are very much applicable.

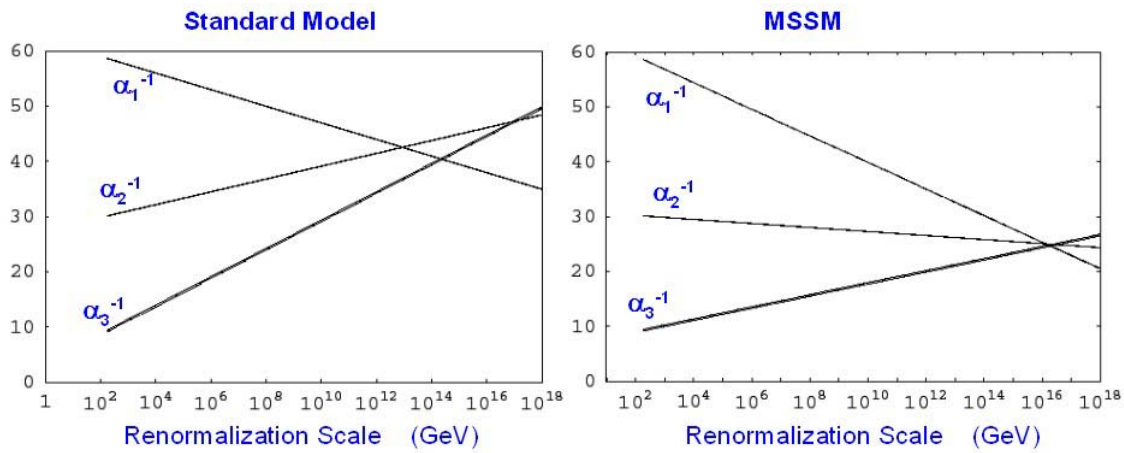

Figure 2.4: Figure shows the running of the inverse gauge couplings with $\ln Q^2$. The gauge couplings which hint at unifying in the SM, unify very well in the MSSM.

mSUGRA, some numerical indications that supersymmetry may be the valid model of physics beyond the standard model are

- The precision data from measurements of electroweak parameters indicates that at 99% C.L. the mass of the Higgs boson $m_H \lesssim 200$ GeV. While the SM has no theoretical constraint on m_H, in the MSSM the lightest higgs particle is expected to be $\lesssim 140$ GeV.

- At one loop order, the inverse gauge couplings run with $\ln Q^2$. In the SM, these couplings hint at unifying at some value, but they do not converge. In the MSSM, if the superpartners are of order 100 GeV to 10 TeV, the gauge couplings unify extremely well (see Fig. 2.4, courtesy of Prof. Scott Thomas).

2.4 The Trilepton Signature

In the following text, nominal signal point refers to this choice of the mSUGRA parameters $m_0 = 60$ GeV, $m_{1/2} = 190$ GeV, $tan(\beta) = 3$, $\mu > 0$, and $A_0 = 0$. This choice is indicative of the mSUGRA parameter region to which this analysis is sensitive. The masses of some of the SUSY particles, and other relevant numbers are summarized in Table 2.5. An important

detail for the plots presented in this section is the software used. The mass spectrum of sparticles is obtained by using ISAJET V7.72 [11]. The cross section for $p\bar{p} \rightarrow \widetilde{\chi}_1^{\pm}\widetilde{\chi}_2^0$ is obtained using PROSPINO2 [12].

Property	Value
$\sigma(p\bar{p} \rightarrow \widetilde{\chi}_1^{\pm}\widetilde{\chi}_2^0)$	0.5 pb
BR($\widetilde{\chi}_1^{\pm}\widetilde{\chi}_2^0 \rightarrow 3l$)	0.937
m($\widetilde{\chi}_1^{\pm}$)	122 GeV/c^2
m($\widetilde{\chi}_2^0$)	124 GeV/c^2
m($\widetilde{\chi}_1^0$), LSP	66 GeV/c^2
m($\widetilde{\tau}_1$)	100 GeV/c^2
m($\tilde{g}$)	477 GeV/c^2
m($\tilde{u}_R$)	421 GeV/c^2

Table 2.5: The table shows some properties of the nominal point with mSUGRA parameters $m_0 = 60$ GeV, $m_{1/2} = 190$ GeV, $tan(\beta) = 3$, $\mu > 0$, and $A_0 = 0$.

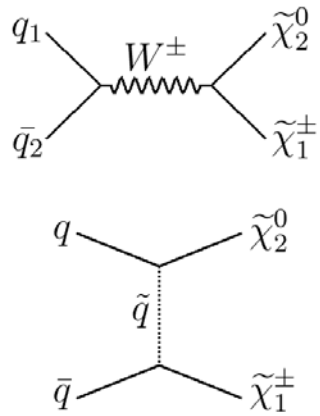

Figure 2.5: The production of $\widetilde{\chi}_1^{\pm}\widetilde{\chi}_2^0$ takes place via the s-channel (top) with destructive interference from the t-channel(bottom).

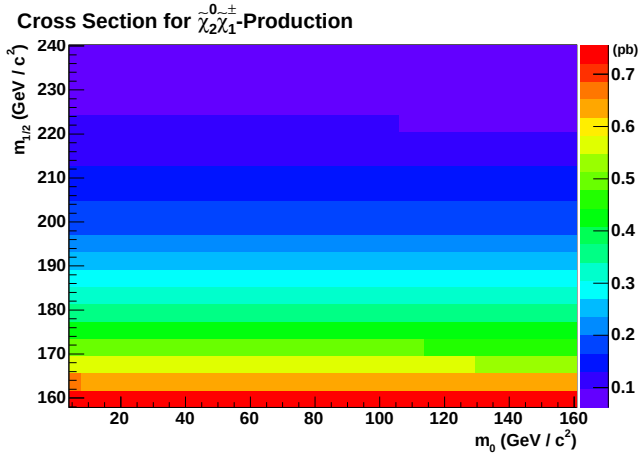

Figure 2.6: The figure shows the cross section of $\widetilde{\chi}_1^\pm\widetilde{\chi}_2^0$ production ($p\bar{p} \rightarrow \widetilde{\chi}_1^\pm\widetilde{\chi}_2^0$)in the m_0-$m_{1/2}$ plane. The other mSUGRA parameters are kept constant at $\tan\beta = 3$, $A_0 = 0$, $\mu > 0$. The $\sigma(\widetilde{\chi}_1^\pm\widetilde{\chi}_2^0)$ is a smooth function of $m_{1/2}$, i.e of the $\widetilde{\chi}_1^\pm$ mass.

2.4.1 Production of $\widetilde{\chi}_1^\pm\widetilde{\chi}_2^0$

We search for the associated production of the lightest chargino and the next-to-lightest neutralino. The production cross-section for $p\bar{p} \rightarrow \widetilde{\chi}_1^\pm\widetilde{\chi}_2^0$ is much higher than say for $\widetilde{\chi}_1^\pm\widetilde{\chi}_1^0$ production. The only comparable cross-section is for associated production of $\widetilde{\chi}_1^\pm\widetilde{\chi}_1^\pm$; however the resulting dilepton state in this case suffers from large backgrounds. The production of $\widetilde{\chi}_1^\pm\widetilde{\chi}_2^0$ proceeds via the s-channel (Fig. 2.5, top) with destructive interference from the t-channel (Fig. 2.5, bottom). The production cross section σ is a function of the mass of the $\widetilde{\chi}_1^\pm$ or $\widetilde{\chi}_2^0$. In Fig. 2.6, the cross section is shown as a function of m_0 and $m_{1/2}$, while keeping the other mSUGRA parameters the same as the nominal point.

In Fig. 2.7, the dependence of m($\widetilde{\chi}_1^\pm$) on m_0 is shown (left). The other mSUGRA parameters are fixed as for the nominal point. As a consequence of the slight increase in m($\widetilde{\chi}_1^\pm$) with increasing m_0, $\sigma(\widetilde{\chi}_1^\pm\widetilde{\chi}_2^0)$ decreases slightly (right-hand figure). The branching ratio, BR($\widetilde{\chi}_1^\pm\widetilde{\chi}_2^0 \rightarrow 3l$), on the other hand has a dramatic decline. The reason for this will be evident once the decays of the $\widetilde{\chi}_1^\pm$ and $\widetilde{\chi}_2^0$ are understood. Before moving the the decays, we examine the behavior of $\sigma(\widetilde{\chi}_1^\pm\widetilde{\chi}_2^0)$ for the other mSUGRA parameters. In Fig. 2.8, we show the variation of m($\widetilde{\chi}_1^\pm$) (left) and $\sigma(\widetilde{\chi}_1^\pm\widetilde{\chi}_2^0)$ (right) with $\tan\beta$. Figure 2.9 shows the

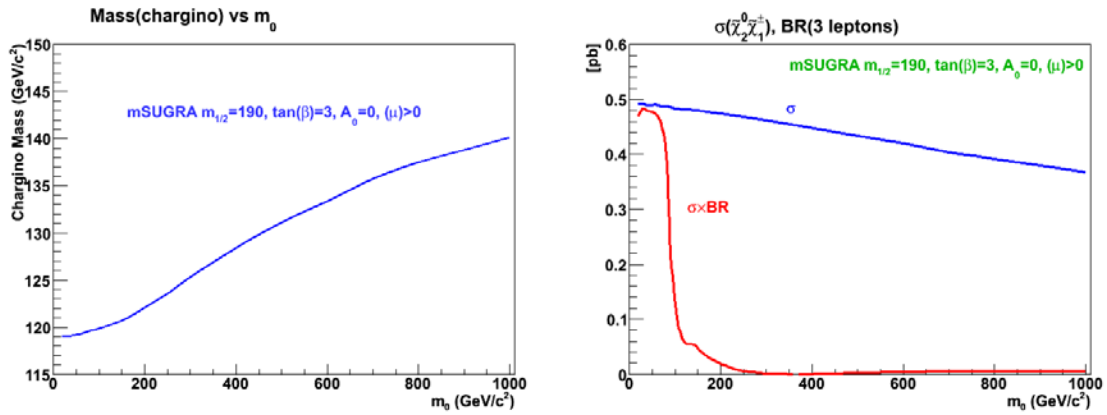

Figure 2.7: Figure shows m($\widetilde{\chi}_1^{\pm}$) (left) and $\sigma(p\bar{p} \to \widetilde{\chi}_1^{\pm}\widetilde{\chi}_2^0)$ as a function of m_0. Other mSUGRA parameters are fixed at the values chosen for the nominal point.

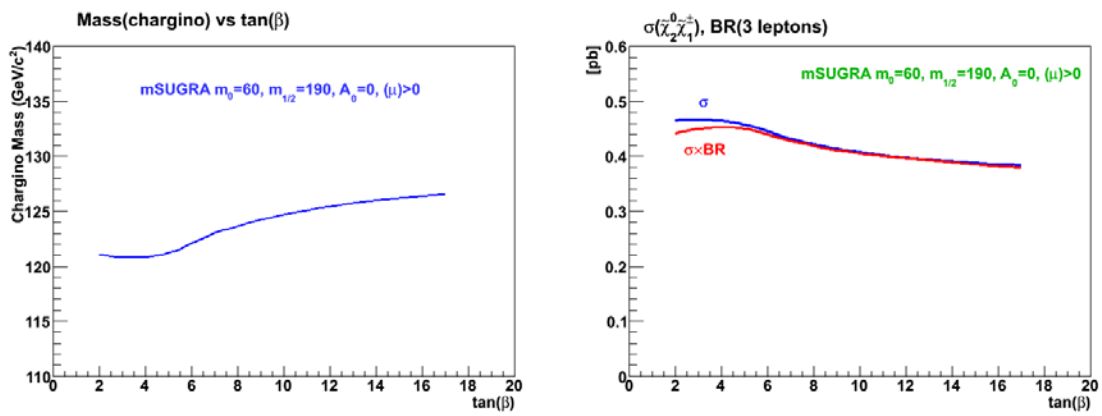

Figure 2.8: Figure shows m($\widetilde{\chi}_1^{\pm}$) (left) and $\sigma(p\bar{p} \to \widetilde{\chi}_1^{\pm}\widetilde{\chi}_2^0)$ as a function of $\tan\beta$. Other mSUGRA parameters are fixed at the values chosen for the nominal point.

variation of m($\widetilde{\chi}_1^{\pm}$) and $\sigma(\widetilde{\chi}_1^{\pm}\widetilde{\chi}_2^0)$ with A_0. As before, the mSUGRA parameters aside from the one on the abcissa are held constant at the values of the nominal point.

2.4.2 Decay of $\widetilde{\chi}_1^{\pm}\widetilde{\chi}_2^0$

The $\widetilde{\chi}_1^{\pm}$ and $\widetilde{\chi}_2^0$ decays can proceed via two processes to give the final trilepton state. For simplicity, the two decay modes will be referred to as 3−body decays and 2−body decays. The 3−body decays are straightforward; the $\widetilde{\chi}_1^{\pm}$ and $\widetilde{\chi}_2^0$ decay via virtual W, Z or virtual sleptons[4], and give the final trilepton state in the following way :

$\widetilde{\chi}_1^{\pm} \to l^{\pm}\nu\widetilde{\chi}_1^0$, and

[4]Or sneutrino in case of $\widetilde{\chi}_1^{\pm}$.

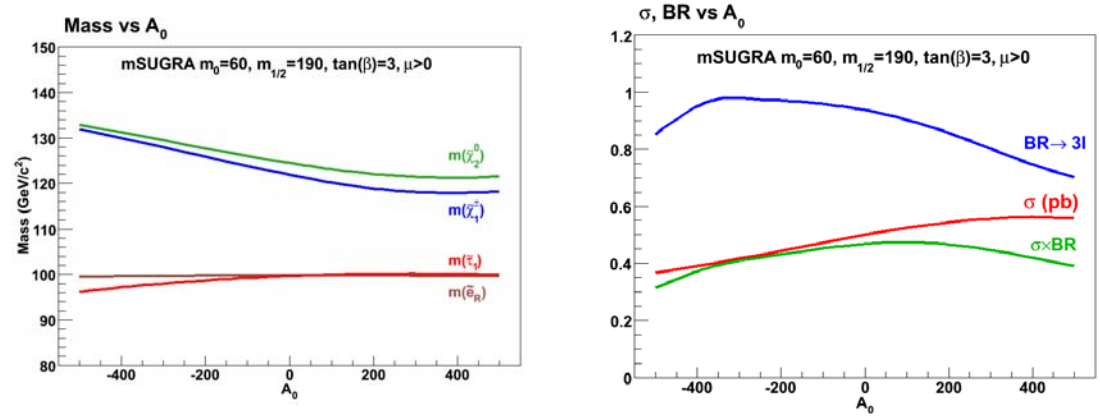

Figure 2.9: Figure shows m($\widetilde{\chi}_1^{\pm}$) (left) and $\sigma(p\bar{p} \rightarrow \widetilde{\chi}_1^{\pm}\widetilde{\chi}_2^0)$ as a function of A_0. Other mSUGRA parameters are fixed at the values chosen for the nominal point.

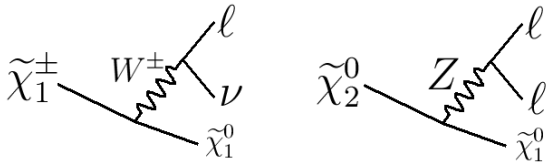

Figure 2.10: Figure shows the 3−body decay modes of the $\widetilde{\chi}_1^{\pm}$ and $\widetilde{\chi}_2^0$.

$\widetilde{\chi}_2^0 \rightarrow l^{\pm}l^{\mp}\widetilde{\chi}_1^0$.

Clearly, the decay via virtual sleptons (sneutrinos) happens only when the slepton (sneutrino) is heavier than the $\widetilde{\chi}_1^{\pm}$ and $\widetilde{\chi}_2^0$. These decays are illustrated in Fig. 2.10.

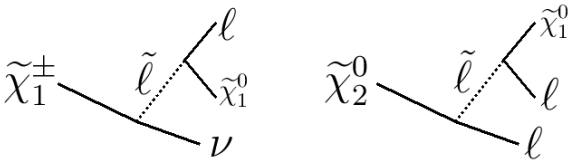

Figure 2.11: Figure shows the 2−body decay modes of the $\widetilde{\chi}_1^{\pm}$ and $\widetilde{\chi}_2^0$.

If however the $\tilde{l}^{\pm}$ is lighter than the $\widetilde{\chi}_1^{\pm}$ or $\widetilde{\chi}_2^0$, then the decays can be 2−body decays and proceed via intermediate slepton states as follows :

$\widetilde{\chi}_1^{\pm} \rightarrow \tilde{l}^{\pm}\nu$, and

$\widetilde{\chi}_2^0 \rightarrow \tilde{l}^{\pm}l^{\mp}$ where in each case the slepton decays to a lepton and the LSP, $\tilde{l}^{\pm} \rightarrow l^{\pm}\widetilde{\chi}_1^0$.

Alternatively, the $\widetilde{\chi}_2^0$ can decay as above, and the $\widetilde{\chi}_1^\pm$ can decay via a real $\tilde{\nu}$ as follows[5]: $\widetilde{\chi}_1^\pm \to \tilde{\nu} l^\pm$, followed by $\tilde{\nu} \to \nu \widetilde{\chi}_1^0$. The 2−body decays are shown in Fig. 2.11.

The final state in both cases is the same, $\widetilde{\chi}_1^\pm \widetilde{\chi}_2^0 \to l^\pm l^\mp l'^\pm \nu \widetilde{\chi}_1^0 \widetilde{\chi}_1^0$, or experimentally $\widetilde{\chi}_1^\pm \widetilde{\chi}_2^0 \to l^\pm l^\mp l'^\pm + \not{E}_{\mathrm{T}}$. The branching ratio of $\widetilde{\chi}_1^\pm \widetilde{\chi}_2^0$ into three leptons is shown in Fig. 2.12 in the m_0-$m_{1/2}$ plane. The other mSUGRA parameters are held at the values of the nominal point. The features of this plot will be explored later in Section 7.3.1 where their impact will be much more evident. Here, it will suffice to look at Region A, where m($\tilde{\nu}$)>m($\tilde{l}^\pm$)>m($\widetilde{\chi}_1^\pm$). The decays of $\widetilde{\chi}_1^\pm$ and $\widetilde{\chi}_2^0$ are via virtual W, Z or virtual sleptons. As m_0 increases[6], the amplitude of decays via virtual sleptons decreases, and the decays via virtual W, Z dominate. At high m_0, the branching ratio for $\widetilde{\chi}_1^\pm \widetilde{\chi}_2^0$ decay to three leptons is similar to the WZ branching ratio; i.e. much smaller than in the 2−body case. This explains the behavior of BR($\widetilde{\chi}_1^\pm \widetilde{\chi}_2^0 \to 3l$) in Fig. 2.7.

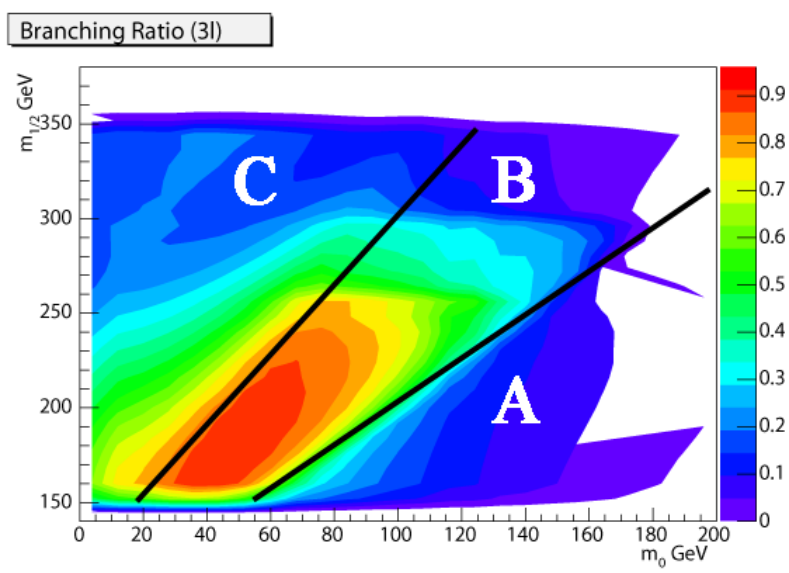

Figure 2.12: The figure shows the branching ratio to trileptons, BR($\widetilde{\chi}_1^\pm \widetilde{\chi}_2^0 \to 3l$) in the m_0-$m_{1/2}$ plane ($l = e, \mu, \tau$). The other mSUGRA parameters are kept constant at $\tan\beta = 3$, $A_0 = 0$, $\mu > 0$. The bin size is 10 GeV/c^2 × 10 GeV/c^2, although in certain places a finer grid is used. Region A: m($\tilde{\nu}$)>m($\tilde{l}^\pm$)>m($\widetilde{\chi}_1^\pm$); Region B: m($\tilde{\nu}$)>m($\widetilde{\chi}_1^\pm$)>m($\tilde{l}^\pm$); Region C: m($\widetilde{\chi}_1^\pm$)>m($\tilde{\nu}$)>m($\tilde{l}^\pm$);

[5]If the $\widetilde{\chi}_2^0$ decays via a $\tilde{\nu}$, the final state does not have 3 leptons.

[6]i.e. increasing slepton mass

In Figure 2.13 the generator level p_{T} distributions for the three leptons are shown, ordered in p_{T} for the nominal signal point. It is evident that leptons with low p_{T} need to be efficiently identified in order to maximize the sensitivity of the analysis. A detailed description of the behavior of the trilepton signature in the mSUGRA parameter space is given in Ref. [13].

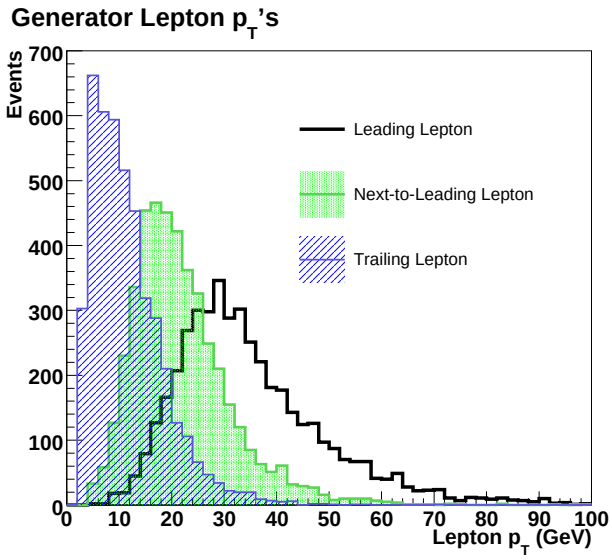

Figure 2.13: p_{T} distributions for generator level leptons for nominal signal point. Three lepton events are selected and the leptons are ordered in p_{T} . Lepton here refers to electrons, muons and tau-leptons.

2.4.3 Standard Model Backgrounds

Given the trilepton signature, $3l + \not{E}_{\mathrm{T}}$, the relevant standard model backgrounds can be determined. In the SM, the signature of WZ production, when they decay leptonically, is the same as that for signal. This is not suprising, since the $\widetilde{\chi}_1^{\pm}\widetilde{\chi}_2^0$ are the superpartners of the SM gauge bosons. It is also possible to obtain the same signature in the leptonic decay of $t\bar{t}$. The decay $t\bar{t} \rightarrow W^{\pm}bW^{\mp}\bar{b} \rightarrow l^{\pm}\nu l^{\mp}\nu b\bar{b}$, when followed by a semileptonic decay of a B-meson will give $3l + \not{E}_{\mathrm{T}}$. However, the possibility of a third lepton here is much smaller, and the dilepton final state of $t\bar{t}$ decay will be predominant[7].

[7]If both W's decay leptonically

The leptonic decay of ZZ will also lead to more than three leptons. Note that here (as well as for WZ) and henceforth Z will include the off-shell contribution unless specified otherwise[8]. However, there is no intrinsic $\not{E}_{\mathrm{T}}$ in the ZZ final state. On the other hand, if one of the Z's decays to the invisible state, i.e. $\nu\nu$, then the final state has significant $\not{E}_{\mathrm{T}}$, but is missing one lepton. This missing lepton, in principle, can be obtained from a photon conversion, where the photon comes from initial state radiation or final state radiation[9]. We shall see in Section 4.4 that there is an additional source of background; hadrons in the event can 'fake' a lepton if they pass all the selection criteria for leptons. Table 2.6 shows the different SM backgrounds and the ratio of the background cross section the to the cross section for the nominal signal point. The table also shows the leptonic final states associated with the background, and what else will be needed for the SM process to become a background. For example, WW production cross section is of the same order as signal. The leptonic decay leads to two leptons + $\not{E}_{\mathrm{T}}$ in the final state. To become a background for this search, the WW process needs an extra lepton.

Process	σ(bkgd)/σ(sig)	What it has	What it needs
$WZ \to lll\nu$		$3l + \not{E}_{\mathrm{T}}$	-
$ZZ \to llll$	$\sim$1	$\geq 3l$	$\not{E}_{\mathrm{T}}$
$WW \to ll\nu\nu$		$2l + \not{E}_{\mathrm{T}}$	one l
$t\bar{t} \to WbWb$	$\sim$10	$2l + \not{E}_{\mathrm{T}}$	one l
Drell-Yan$\to ll$	$\sim$1000	$2l$	one l + $\not{E}_{\mathrm{T}}$
$Z\gamma \to ll\gamma$	$\sim$30	$\geq 3l$	$\not{E}_{\mathrm{T}}$
$W \to l\nu$	$\sim$5000	one l + $\not{E}_{\mathrm{T}}$	two l

Table 2.6: The standard model backgrounds to the trilepton signature.

The inclusion of $W \to l\nu$ in the table might seems suprising, but with hindsight, this process will result in background for certain analysis channels which will be described later. The point to note here is that although the W production needs two leptons to become a

[8]Usually by making an invariant mass selection specifically for the Z

[9]bremsstrahlung from one of the other leptons

background, the ratio of cross sections is relatively high. This means, that even in cases where the 'fake' probability is low, this background might not be negligible. A notable absence of background is from the production and semileptonic decay of $b\bar{b}/c\bar{c}$, i.e. so called heavy flavor background. The heavy flavor background has been extensively studied. Again, with hindsight, with the lepton E_{T} thresholds, and other analysis selections, heavy flavor background is negligibly small [14].

2.5 Prior Constraints

The phenomenology of supersymmetry is rich in signatures, and also the possible models and scenarios. This is a very good sign for experimental reasons. These searches can then be used to constrain, and eventually rule out specific models. Constraints are usually obtained from indirect results or from direct searches. An example of an indirect result would be the use of cosmological studies of dark matter to constrain the LSP properties with certain assumptions [15]. Here we focus on the direct searches on $\widetilde{\chi}_1^{\pm}$. The direct searches are usually applicable without too many assumptions.

The direct searches of $\widetilde{\chi}_1^{\pm}$ performed at the LEP experiments present the most robust constraints [16]. These results are summarized in an excellent diagram in Ref. [1], reproduced in Fig. 2.14 and are described in Ref. [17]. The higgsino-like scenario is not applicable here. In the higgsino-like scenario, $\mathrm{m}(\widetilde{\chi}_1^{\pm})\simeq\mathrm{m}(\widetilde{\chi}_2^{0})\simeq\mathrm{m}(\widetilde{\chi}_1^{0})$, where the $\widetilde{\chi}_1^{\pm}$ decay will have a significantly different phase space. The mass limits in the gaugino-like scenario, which has similar mass relations as mSUGRA, are shown on the left side.

The results from the LEP collider are obtained from a combination of the four LEP experiments, Aleph, Delphi, Opal and L3. The result on the $\widetilde{\chi}_1^{\pm}$ mass is shown in Fig. 2.15. The results rule out $\mathrm{m}(\widetilde{\chi}_1^{\pm})< 103.5$ GeV/c^2. It is assumed that $\mathrm{m}(\tilde{\nu})> 300$ GeV/c^2, and the chargino decay is $\widetilde{\chi}_1^{\pm} \rightarrow \widetilde{\chi}_1^{0}W^*$. This condition translates in to an mSUGRA region where m_0 is large. While the $\mathrm{m}(\tilde{\nu})$ condition is not always necessarily fulfilled, the limit on $\mathrm{m}(\widetilde{\chi}_1^{\pm})$ remains robust to within a GeV/c^2. However, since the LEP experiments include channels

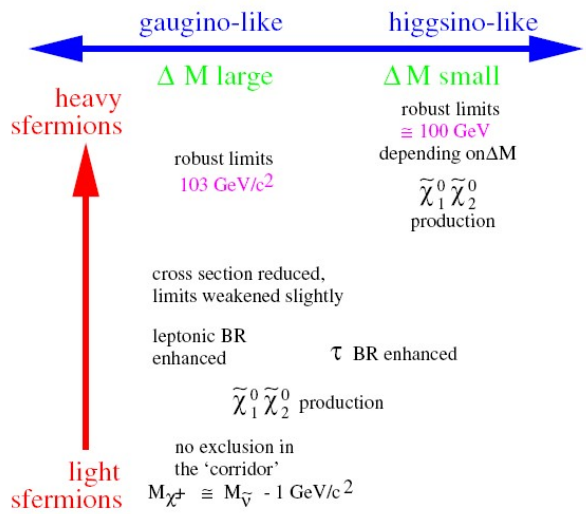

Figure 2.14: Figure shows the summary of the $\widetilde{\chi}_1^{\pm}$ mass limits, in various scenarios [1]. The gaugino-like scenario is applicable here. ΔM =m($\widetilde{\chi}_1^{\pm}$)−m($\widetilde{\chi}_1^0$).

with jets in the final state[10] the effect of the $\widetilde{\chi}_1^{\pm}$ decay condition on the applicability of these limits is harder to judge.

Limits are also placed on m($\widetilde{l}^{\pm}$); 99, 95, and 86 GeV/c^2 for $\widetilde{e}$, $\widetilde{\mu}$, and $\widetilde{\tau}$ respectively. These limits give indirect contraints on $\widetilde{\chi}_1^{\pm}$ mass, and shall be ignored here. The limits for mSUGRA in the m_0-$m_{1/2}$ plane from several supersymmetric searches are shown in Fig. 2.16. Prior results from the CDF collaboration [18] do not place constraints within the context of mSUGRA beyond those imposed by LEP experiments. They place limits on m($\widetilde{\chi}_1^{\pm}$) using a 'mSUGRA-like' scenario. The DØ collaboration also places limits in a similar scenario [19]. For this scenario, along with the mass relations on the gauginos, mass universality of the sleptons is also imposed. In addition, no mixing between the sleptons is allowed. The DØ published result has been superseded by preliminary results [20] which extend the published limits on m($\widetilde{\chi}_1^{\pm}$) in the same scenario. The published results from CDF are m($\widetilde{\chi}_1^{\pm}$)>130 GeV/c^2, the preliminary results from DØ are m($\widetilde{\chi}_1^{\pm}$)>145 GeV/c^2. For the analysis described in this dissertation, we do not assume m($\widetilde{l}^{\pm}$)>m($\widetilde{\chi}_1^{\pm}$); this limits the applicability of the DØ results.

[10] i.e the W^* need not decay leptonically

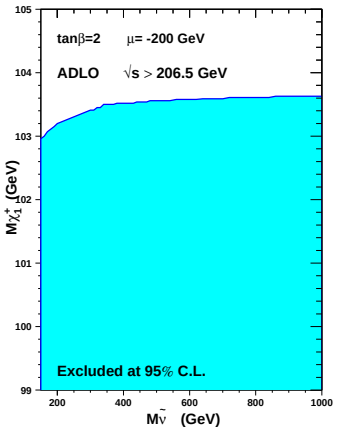

Figure 2.15: Limits on m($\widetilde{\chi}_1^{\pm}$) from LEP experiments

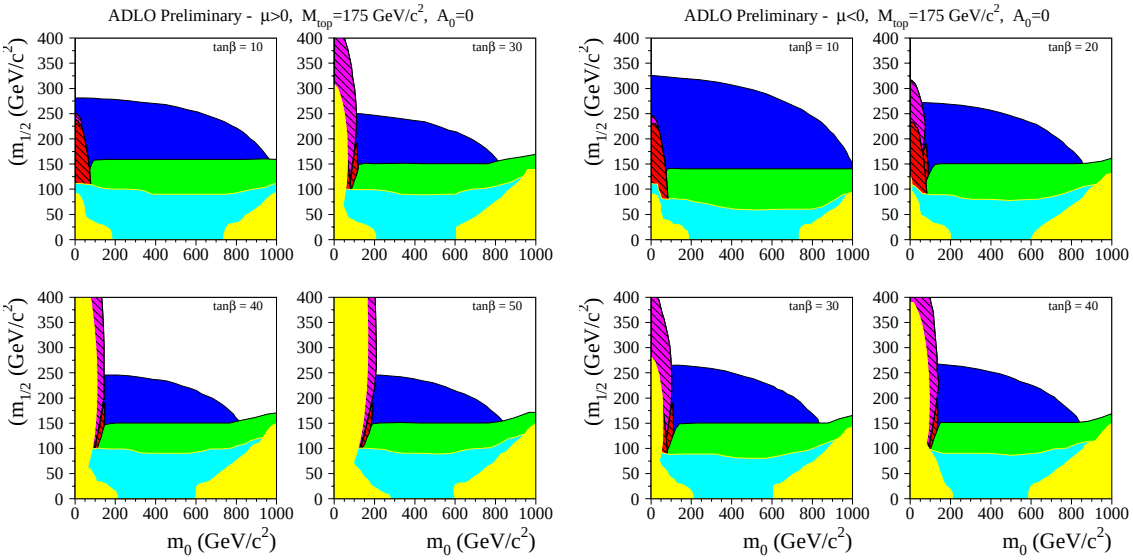

Figure 2.16: LEP2 Limit on mSUGRA for positive and negative μ, and for different $\tan\beta$. $A_0 = 0$ for all plots. ADLO refers to the four LEP experiments. The legend is as follows : Yellow - no mSUGRA solution, no EWSB or tachyonic particles, Cyan - Regions inconsistent with EWK measurements at LEP1, Green - Excluded by chargino searches, Red - Excluded by selectron or stau standard searches, Blue - Excluded by search for hZ, Brown - Excluded by the neutralino stau cascade searches, and Pink - Excluded by the search for stable charged particles applied to staus.

Chapter 3

The Tevatron and the CDF Detector

The Tevatron accelerator was the world's highest energy accelerator for the better part of this decade. It is located at the Fermi National Accelerator Laboratory (Fermilab), situated about 35 miles west of Chicago, Illinois on a 6800-acre site. The Tevatron was built in the late 1960's, and has been a part of many important discoveries. The bottom-quark (1977) and the top-quark (1995) were discovered at the experiments at Fermilab. The work presented here was carried out at the CDF experiment at Fermilab. CDF, which stands for Collider Detector at Fermilab, is an international collaboration of around 600 physicists. The CDF II detector is a 5000-ton multipurpose detector designed with the goal of discovering signs of new physics, and measuring the properties of known standard model particles accurately. In this chapter, we shall discuss the Tevatron accelerator and the CDF II detector.

3.1 The Accelerator Complex

The Tevatron is a sophisticated accelerator complex consisting of five different accelerators. A schematic view of the accelerator complex is shown in Fig. 3.1. The final goal of the complex is to collide two beams, one of protons (p) and one of antiprotons ($\bar{p}$) each with energy of 980 GeV. The center of mass energy is thus 1960 GeV, and collisions happen at two interaction points around the main Tevatron accelerator.

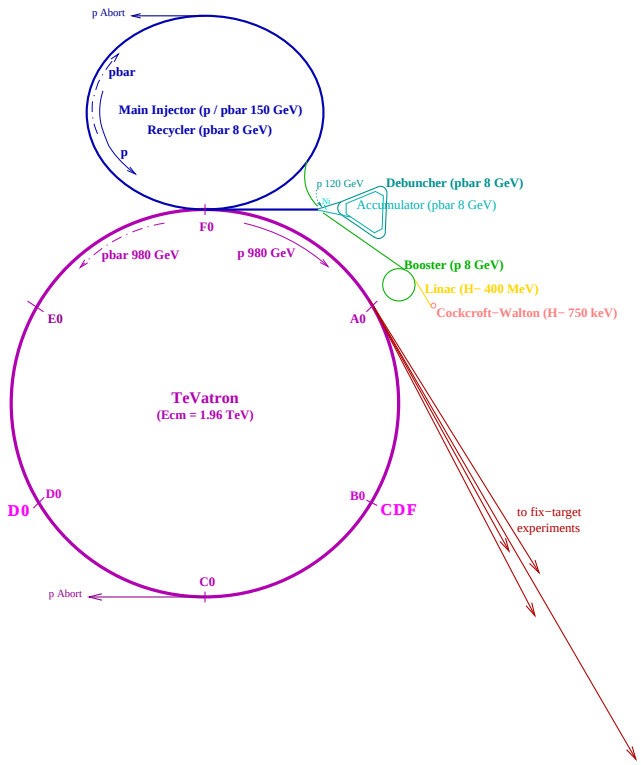

Figure 3.1: Figure shows the schematic diagram of the Fermilab accelerator complex.

3.1.1 Obtaining Protons

The process starts with a hydrogen bottle, and the Cockroft-Walton chamber. A large electric discharge into H_2 gas produces H^- ions with 25 KeV energy. The Cockroft-Walton preaccelerator boosts the energy to 750 KeV, and the H^- ions are taken to the Linac via a magnetic transfer line. The Linac, a linear accelerator, takes the beam to 400 MeV and injects the beam in to the Booster.

The Booster is a rapid cycling synchrotron, 150m in diameter. The H^- beam obtained from the Linac is overlaid with the previously circulating beam of protons. The beam is passed through a carbon foil, where the H^- ions are stripped of the electrons to obtain a proton beam. The Booster has a revolution period of 2.22 ms. The collected protons in the Booster are accelerated using the conventional method of varying RF fields in accelerating cavities to an energy of 8 GeV and injected in to the Main Injector. The protons in the Booster are divided into 84 bunches separated by 18.9 ns; a maximum of 5×10^{12} protons

can be contained in one batch of protons from the Booster.

3.1.2 Main Injector

The Main Injector (MI) is a synchrotron with exactly seven times the circumference of the Booster. It is thus able to hold six Booster batches plus a spare slot for switching purposes. The MI has been designed with the following goals in mind : a) accept 8 GeV protons (antiprotons) from the Booster (or the Accumulator, Recycler); b) accelerate the protons to 120 GeV and send them to the $\bar{p}$ production target, the fixed target experiments and the NuMI[1] beamline for neutrino production; c) accelerate the protons and antiprotons to 150 GeV for injection in to the Tevatron.

One cycle of the MI consists of accelerating the six bunches (6×10^{10} protons) to flat-top, i.e 150 GeV, coalescing the bunches in to one bunch and injecting it in to the Tevatron.

The main task of the MI is to produce antiprotons. A beam of 120 GeV from the MI is collided with a nickel target. The resulting debris of particles is collimated through a Lithium lens. A pulsed dipole magnet is used to select negative particles of 8 GeV energy; one $\bar{p}$ is obtained per approximately 100,000 protons. The antiprotons are then sent the Accumulator. The antiprotons need to be confined in a small phase space volume. Thermodynamically this means cooling the beam, which is done partially in the MI and further in the Accumulator. The beam is cooled using betatron and momentum stochastic cooling techniques. In addition, there is also the Recycler ring, constructed with permanent magnets, which is used to recover unused $\bar{p}$'s from the Tevatron. The construction of the Recycler was finished in 1999 for Run 2 of the Tevatron.

[1]The NuMI Beamline is a facility which uses protons from the MI to produce an intense beam of neutrinos for the MINOS experiment

3.1.3 Tevatron

The Tevatron was the first accelerator to use superconducting magnets throughout, and has been declared a heritage site by ASME[2]. The Tevatron has a radius of exactly 1 km. In its normal operating mode for Run 2, there are 36 bunches each of protons and antiprotons. The bunches form three trains of 12 bunches each. The bunches are separated by 396 ns. The trains are separated by 2621 ns, which is known as the *abort-gap*. The abort-gap is essential to allow the beam aborting system to charge the kicker magnet which diverts the beam out of the Tevatron. This protects the sensitive detectors of CDF and DØ from damage due to any beam spray.

The protons are injected first, followed by the antiprotons during the proton beam's abort gap. Just before the antiproton injection, a set of electrostatic separators create a double-helix type of orbit. The protons use one helical orbit, the antiprotons the other. Once all proton and antiproton bunches are in the Tevatron, they are accelerated to flat-top, 980 GeV. In two places around the beam, at the CDF and DØ detectors, the beams are made to collide. The beams are focused using quadropole magnets to reduce the beam size and to maximize the chance of a collision. The number of collisions per unit time is proportional to the instantaneous luminosity $\mathcal{L}$, approximately given by

$$\mathcal{L} = \frac{f N_B N_p N_{\bar{p}}}{2\pi(\sigma_p^2 + \sigma_{\bar{p}}^2)} \tag{3.1}$$

where f =bunch revolution frequency, N_B is the number of bunches, $N_p, N_{\bar{p}}$ are the number of protons and antiprotons in each bunch, and $\sigma_p^2(\sigma_{\bar{p}}^2)$ is the transverse proton (antiproton) beam size at the interaction point. Thus reducing the beam size gives a higher instantaneous luminosity and a higher rate of collisions. At CDF, the transverse section of the beam is circular with a gaussian dispersion of 30 μm.

[2]American Society of Mechanical Engineers

3.2 CDF Detector

The CDF II detector[3] [21, 22] is a general purpose detector with the traditional onion-ring design. It is cylindrically symmetric about the beam axis, and has a solenoidal magnetic field of 1.4 T parallel to the beam axis. Moving radially outwards, the innermost detector next to the beam line is the silicon vertex detector (SVX), followed by the central tracker (COT), the calorimeter, and the muon systems at the very outside. The detector geometry is shown in Fig. 3.2.

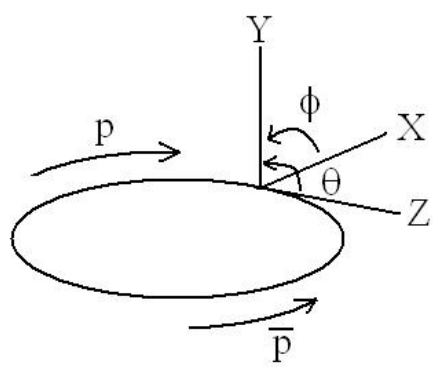

Figure 3.2: Figure shows the geometry of the CDF II detector.

The cartesian co-ordinate system is centred at the geometric center of the the detector, with the Z-axis pointing along the proton direction, and X-axis pointing radially outward from the center of the Tevatron towards CDF. The polar co-ordinates are the azimuthal angle ϕ, measured counterclockwise from the plane of the ring, and θ, measured with respect to the positive Z-axis as shown in the figure. However, θ is not invariant under relativistic boost. Hence, pseudorapidity η is used, which is defined as $\eta = -\ln\tan(\theta/2)$. The coordinate system of (r, η, ϕ) is used henceforth to define various quantities and different regions of the detector. In this section, we shall discuss the subsystems of the CDF detector relevant to this analysis. Figure 3.3 shows an elevation view of the CDF detector.

[3]or CDF for short

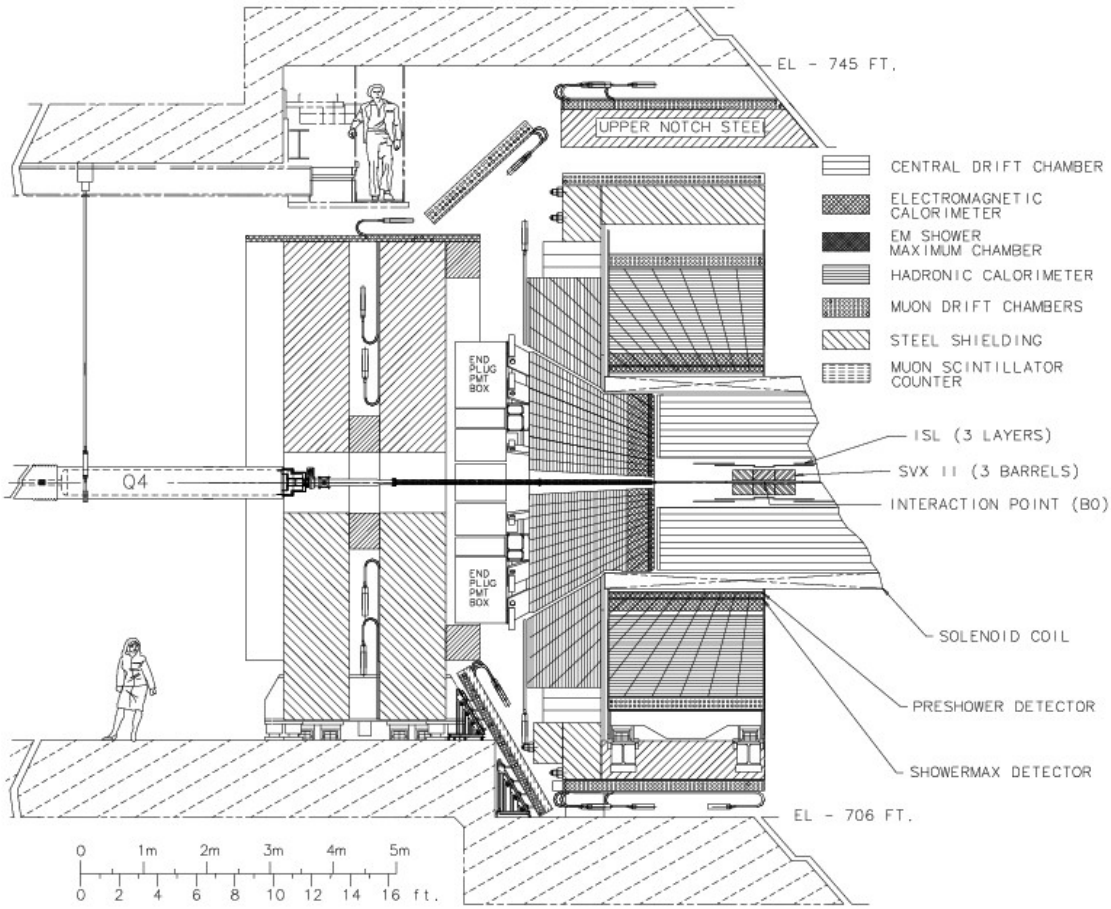

Figure 3.3: Figure shows the elevation view of the CDF II detector. The various subsystems are labelled and are described in the text.

3.2.1 COT : Central Outer Tracker

The COT [23] consists of an open-cell wire drift chamber used for spatial tracking of charged particles and measuring their momentum. The COT is 3.1 m long and extends from radius of 40 to 137 cm within $|z| < 155$ cm. It covers the pseudorapidity range $|\eta| < 1.1$, which is defined as the central region of the CDF detector. It sits inside the solenoid, and thus charged particles follow a helical path inside the COT. The particle trajectories are described by these parameters :

- z_0 - z coordinate of the tracks closest approach to the Z-axis.
- d_0 - the impact parameter, the distance from the point of closest approach to the

Z-axis.

- ϕ_0 - ϕ direction of p_{T} of the particle at the point of closest approach to the Z-axis
- $\cot\theta$ - the pitch of the helix; i.e. ratio of the helix step to its diameter.
- C - the helix curvature.

The particle transverse and longitudinal momentum is then determined as $p_{\mathrm{T}} = cB/2|C|$, and $p_z = p_{\mathrm{T}} \cot(\theta)$.

The COT has 8 superlayers, each consisting of 12 planes of sense wires alternated with layers of potential wires. Four superlayers are axial (wires along axial direction), and the other four are stereo (wires tilted ± 3 deg to the axial direction). The COT chamber is filled with a mixture of Argon and Ethane in ratio of 1:1, giving a drift velocity of 100 μs/ns. Charged particles travel through the gas mixture and leave a trail of ionization electrons. The electrons drift towards sense wires; to account for their motion in the combined electrical and magnetic fields, the drift chambers are aligned 35 deg (the Lorentz angle). The momentum resolution of the COT is $\delta p_{\mathrm{T}}/p_{\mathrm{T}} \simeq 0.3\%\ p_{\mathrm{T}}/(\mathrm{GeV}/c)$.

A point to note is that the COT determines the geometry of the CDF detector. The origin of the CDF coordinate system is at the COT center.

3.2.2 Calorimeter

The CDF calorimeters [24] are placed outside the solenoid and are designed to measure the energy of charged and neutral particles coming out of the tracking chamber. The calorimeter is split into towers projecting outwards from the center of the detector. The towers are composed of two subsystems, and electromagnetic part on the inside, and a hadronic part on the outside. As the names suggest, the electromagnetic calorimeter is meant to degrade most of the energy of electrons and photons, with the hadronic calorimeter intended for showering of hadrons. We shall discuss the central electromagnetic calorimeter (CEM) and the central hadronic calorimeter (CHA) here.

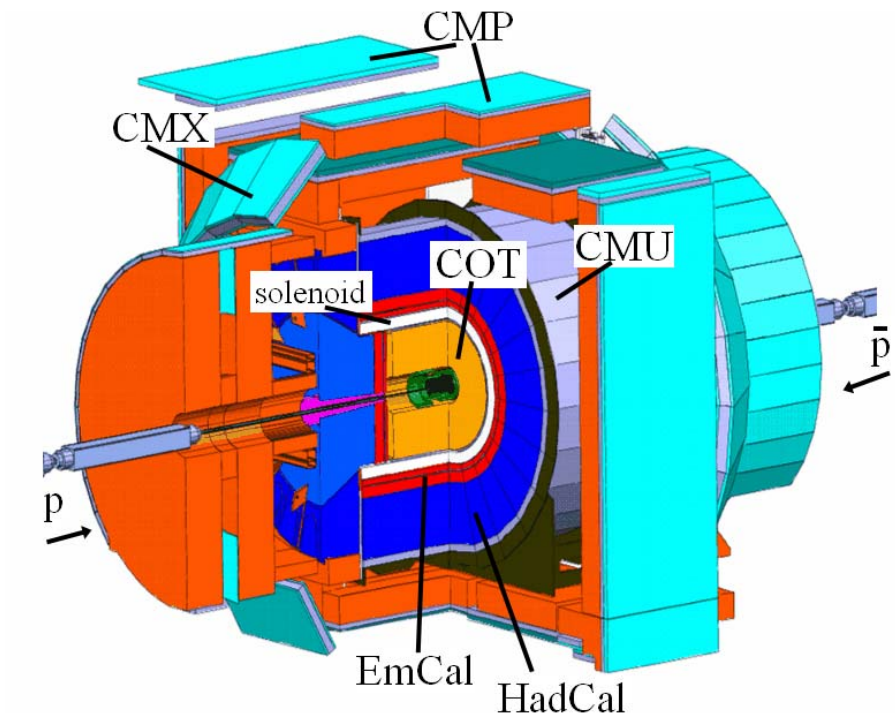

Figure 3.4: Figure shows the cut-away view of the CDF II detector. The various subsystems are labelled and are described in the text.

The electromagnetic calorimeter (EMcal or CEM) is a sampling calorimeter with the passive element being lead, alternated with sheets of scintillator. As an electron traverses the CEM, it bremsstrahlungs , and the bremsstrahlung photon produces e^+e^- pairs, photons also produce e^+e^- pairs. Each particle in the pair produces more photons, and more pairs. This showering process continues till the particle loses energy and is unable to produce e^+e^- pairs any more. The radiation length X_0 is defined as the mean length over which a high energy electron will lose all but $1/e$ of its energy by bremsstrahlung. The CEM is $19X_0$ deep.

The CEM consists of two halves, each consisting of 24 wedges in ϕ, each wedge subtending an angle of 15 degrees. Each wedge has ten towers in steps of $\Delta\eta = 0.11$. The

Central Electromagnetic Strip chamber (CES) is placed $5.9X_0$ deep in the CEM to improve the spatial resolution of the calorimeter. The CES consists of wires in the $r\phi$ direction and cathodes in the z direction, and provides a measurement of the charge deposition corresponding the maximum electromagnetic shower development. The CES resolution is about 1 cm in z and 1 mm in $r\phi$, and it provides a means of distinguishing electrons from photons by accurately matching the shower to a track.

The CHA has the same geometry as the CEM and consists of iron as the passive medium. The CHA is intended to absorb the energy from most hadrons, with only minimum ionizing particles such as muons, or weakly interacting particles such as the neutrino escaping beyond the CHA. Similar to X_0, we define the interaction length λ_0 to characterize the energy loss by nucelar interactions. λ_0 is the nuclear inelastic length for interactions of the particle with nuclei of the detector material. The CHA is $4.7\lambda_0$ deep.

3.2.3 Muon systems

At the very outside of the CDF detector are the muon systems [25]. Muons are minimum-ionizing particles; i.e. they are not expected to shower in any of the inner detectors, and any charged particle signal at the outside of the calorimeters is expected to be predominantly from muons. The central muon subsystems are CMU : central muon detectos, CMP : central muons upgrade, and CMX : central muon extension. Figure 3.5 shows the muon coverage.

The CMU chambers consist of a four-layered stacked array of drift chambers with rectangular cells. It covers the region $|\eta| < 0.6$ and detects muons with $p_{\mathrm{T}} > 1.4$ GeV/c. The CMP chambers are located outside the CMU chambers behind additional shielding. The CMP chambers use the solenoid's return yoke as absorbing steel. The CMP has the same η range as the CMU, but due to the additional shielding, it can detect muons with $p_{\mathrm{T}} > 2.2$ GeV/c. The CMX chambers operate from $0.6 < \eta < 1.0$ and extend the central muon coverage to about the same as the central tracker or calorimeter.

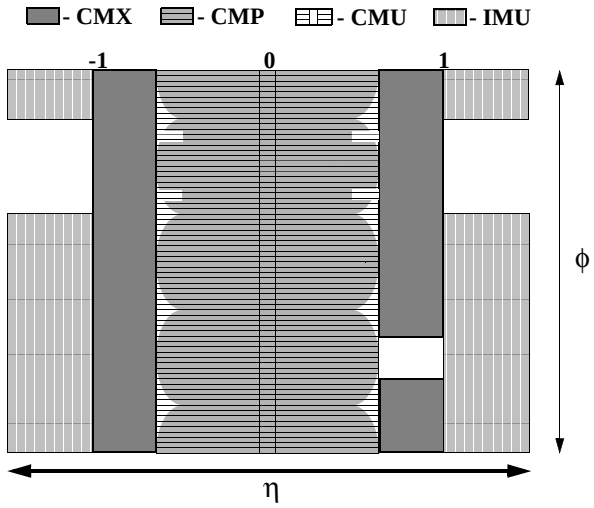

Figure 3.5: Figure shows the muon coverage of the CDF II detector. The various subsystems are described in the text. IMU stands for Intermediate Muon detector. The holes in the CMX and IMU are for mechanical reasons such as readout cables etc.

3.2.4 Luminosity Measurement

Luminosity which is a measure of quantity of data, is measured using the Cherenkov Luminosity Counters (CLC's) [26]. A CLC module contains 48 cm long gas Cherenkov counters arranged around the beam pipe in three concentric rings and projecting to the nominal interaction point. Two such modules are installed in the high-η region between 3.75 and 4.75, and they measure the online luminosity in real-time. The CLC's, as the name suggests, use Cherenkov radiation from particles coming from the $p\bar{p}$ collisions and measures the average number of interactions per bunch crossing μ. The luminosity is then given by $\mathcal{L} = \mu \cdot f_{bc}/\sigma_{p\bar{p}}$, where f_{bc} is the rate of bunch crossings at the Tevatron and $\sigma_{p\bar{p}}$ is the total $p\bar{p}$ cross-section at $\sqrt{s} = 1.96$ TeV. As a matter of fact, the luminosity measured by the CLC's has to be corrected for the change is $p\bar{p}$ cross-section from $\sqrt{s} = 1.8$ TeV in Run I, to $\sqrt{s} = 1.96$ TeV in Run II. The corrected luminosity is 1.019×CLC luminosity.

The total uncertainty on the luminosity measurement is 6% , which is dominated by uncertainty in the $p\bar{p}$ cross-section (4%) and the CLC acceptance (4.2%).

3.3 Trigger and Data Acquisition System

One bunch crossing at the Tevatron happens every 396 ns. Expecting one collision per bunch crossing, this is defined as an event[4]. This event rate taken at the instantaneous luminosity of the Tevatron translates in to a rate of about 2 MHz, i.e. 2 million events per second.

Ideally, one would like to store every event. However, most events are uninteresting; they do not have a hard collision. Moreover, the time taken to read out the entire detector is about 2 ms, so the rate of 2 MHz cannot be handled. The average event size is of the order of 150 kb, and thus the total throughput is almost impossible to handle with present technology. To address these problems, a method of selecting the interesting events is necessary. This is accomplished by using a trigger system, which makes a fast decision as to whether an event is to be stored. The CDF trigger system is a three-level trigger with minimum deadtime. A schematic of the trigger and data acquisition system is shown in Fig. 3.6.

3.3.1 Level 1

Level 1 is a synchronous hardware trigger. At Level 1, three simultaneous streams of information are used to construct crude physics objects called primitives. The available streams are from the calorimeter, the COT, and the muon systems. These can be put together to construct primitive physics objects such as electrons or muons. In addition a crude estimate of $\not\!\!E_{\mathrm{T}}$ is also available (based on the sum of all calorimeter towers above 1 GeV). The primitives, and combinations of them are then used to fix the trigger requirements.

Level 1 has a latency time (or decision time) of 5.5 μs. Due to this, each subdetector system has a buffer of 42 events during which Level 1 can make its decision. An important piece of information available at Level 1 is from the eXtremely Fast Tracker (XFT).

[4] A $p\bar{p}$ collision

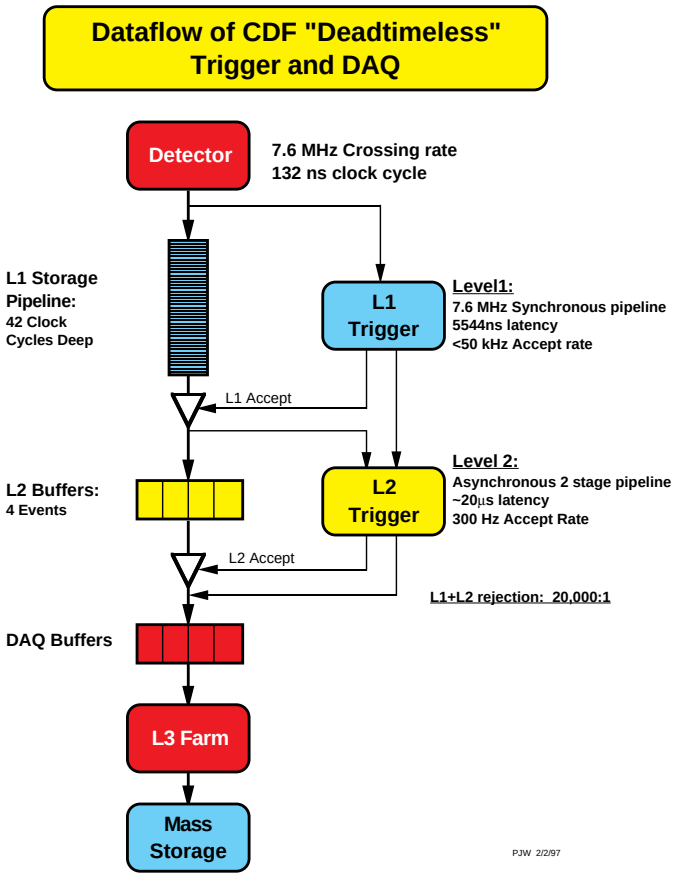

Figure 3.6: Figure shows a block diagram of the deadtime-less CDF data acquisition and trigger systems.

The XFT identifies track primitives in $r - \phi$ using 4 axial superlayers in a two step process. During the first step, the COT axial hits are classified as prompt (drift time < 44 ns) or delayed ($44 <$ drift time < 132 ns). The hits are then compared against a set of predefined patterns of prompt and delayed hits to obtain a valid track. For a match, a 'pixel' is set; 4 pixels seeming to come from the same track are used to crudely determine the track parameters. In the second step, these parameters are used by the XTRP (extrapolator) to extrapolate the track to the detector subsystems such as the calorimeter or muon systems. This information can be used to form advanced primitives at Level 1. The information from XFT is also kept for use at Level 2.

3.3.2 Level 2

Level 2 is an asynchronous trigger. It has a programmable processor that performs some event reconstruction. The primitives available at Level 2 are thus slightly better than those at Level 1; upon a Level 1 accept, the detector front-ends send more information to Level 2 allowing finer granularity and more realistic objects. The Level 2 calorimeter information is supplemented with Level 1 trigger tower information to find energy tower clusters by applying seed and tower thresholds. Level 2 also has information from the CES enabling it to produce electron candidates.

Level 2 has a buffer of 4 events and a latency time of 20 μs. The output rate is reduced to 300 Hz.

3.3.3 Level 3

Only if the event passes Level 2 is the complete detector read out. The Level 3 trigger [27] has two parts, an event builder (EVB) and a computer farm. The EVB collects the events from Level 2, and the event fragments from the entire detector. The fragments are then put together in a coherent way and an event record is constructed. The EVB sends this information to the computer farm of about 300 CPU's.

The computer farm forms a detailed reconstruction of each event. The available information for the Level 3 trigger is almost close to the fully reconstructed events. Level 3 is able to take advantage of the complete detector information and improved resolution. The output rate of Level 3 is around 120 Hz. The Level 3 triggered events are monitored in real-time and the events are sent to the data handling system to be written to long term storage.

3.3.4 Analysis Triggers

The combination of Level 1/Level 2/Level 3 describes a unique trigger path. Each trigger path can form its own dataset, or several logically equivalent triggers can be combined to

form a single dataset. For example, the dielectron, dimuon and $e\mu$ triggers are all part of a dilepton dataset for SUSY analyses. For the analysis presented here, the trigger paths used are described in Section 4.1[5]. An example of the trigger requirements is shown here.

The dielectron trigger path[6] is part of the "SUSY Dilepton" dataset. The requirements at Level 1, Level 2 and Level 3 are as follows :

- Level 1 : Two central towers in the calorimeter with $E_{\mathrm{T}} > 4$ GeV with the fraction of hadronic energy deposit to electromagnetic < 0.125, and two tracks from the XFT with $p_{\mathrm{T}} > 4$ GeV/c.
- Level 2 : The Level 1 requirements are repeated here, with the better Level 2 reconstruction of the event. In addition, two CES towers with $E_{\mathrm{T}} > 3$ GeV are also required.
- Level 3 : At Level 3, the two electron candidates are required to pass these identification criteria : CES $\chi^2 < 20$, Lshr< 0.2, Had/Em< 0.125, $|\Delta Z| < 8$ cm, in addition to the E_{T} and p_{T} requirements of 4 GeV and 4 GeV/c. The identification criteria are explained in Section 3.5.

Similarly, some other trigger paths are a) Dimuon trigger path, b) Single electron with $p_{\mathrm{T}} > 18$ GeV/c etc.

3.4 Event Reconstruction

The raw data saved to tape is further processed in to physics objects. The process of creating vertices, tracks, electron candidates, muon candidates etc. is known as reconstruction. The event reconstruction process is carried out with dedicated software versions. For this analysis the majority of data was processed in the CDF software version 6.1, with a small

[5]Also see Appendix A

[6]Trigger efficiency, see Appendix C

part of data reconstructed with v5.3. In this section, we shall discuss the reconstruction of the objects relevant to this analysis.

3.4.1 Tracks

The reconstruction of tracks is of primary importance in the event. The tracks determine the event vertex, and are an important part of the identification of electrons and muons.

The track reconstruction algorithm for the tracks used here starts from the COT hits. It converts the TDC output in to hit position, and then searches for three consecutive wires to fit to a straight line. The algorithm constructs track segments with four or more hits in each superlayer of the COT. The segments are the foundation of the segment-linking process and form seeds for histogram-linking.

Segment-linking assembles the tracks in to $r\phi$ tracks. Based on the axial segments and the beam position, the algorithm matched hits within 1 cm on circular trajectories. A histogram is filled with the radius of each hit; if one bin has more than 10 hits, then a track is reconstructed. A CDF track has more than 20 hits. After tracks are reconstructed in $r\phi$, the algorithm starts from outer stereo layer and matches stereo segments to tracks. The track is continually refit to obtain the z and angular information. The track parameters are also modified according to calibrations for the magnetic field, and for effects such as material in the COT.

3.4.2 Vertex

A vertex is defined by the intersection of multiple tracks. This analysis requires the presence of a good quality vertex; with quality quantified by the number of COT tracks used in the reconstruction. A dedicated algorithm generates a list of vertex candidates. The vertex candidate with the highest sum-p_{T} of tracks is taken as the primary vertex of the event.

The distribution of the event vertex is shown in Fig. 3.7 for dilepton-triggered data. The vertex z has a spread of about 30 cm around the detector center. For fiduciality reasons,

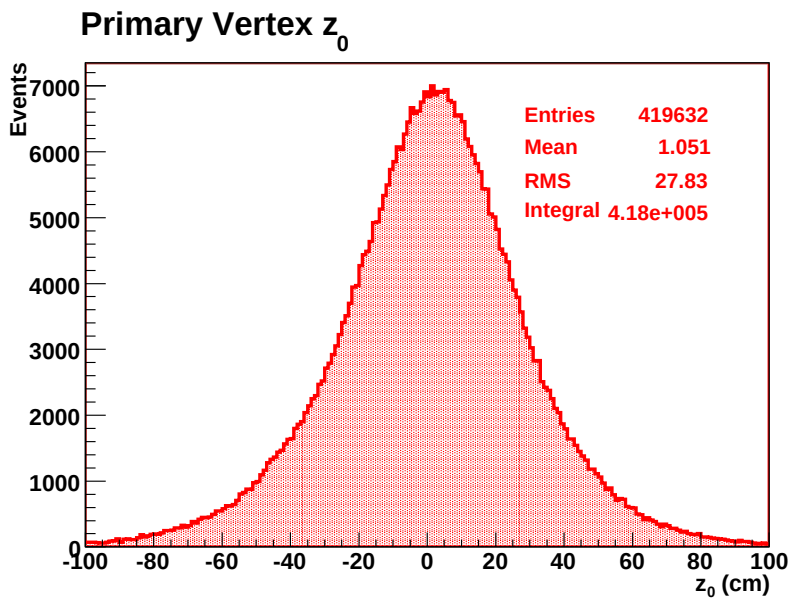

Figure 3.7: Figure shows z_0 distribution of the primary event vertex in the dilepton triggered data. Events with $z_0 > 60$ cm are discarded.

events with the primary vertex $|z_0| > 60$ cm are discarded. The efficiency of this requirement varies slightly with the data-taking period; it has an average value of 96.2±0.2 % [28].

3.4.3 Electrons

Incident electrons will induce showers across multiple towers in the calorimeter. The electron reconstruction algorithm is based on track reconstruction and the matching of the track to a cluster in the CEM. The electromagnetic clustering algorithm calibrates the towers in the calorimeter and E_{T} -orders them. A tower with energy > 200 MeV is taken as a seed tower, and neighbouring towers with energy > 100 MeV are combined with it to create a cluster. The profile of the energy shower is compared with test beam data, and the use of the CES information is made to accurately match the cluster to the track from the COT.

3.4.4 Muons

The reconstructed muons fall in to two categories : 'stubless' and 'stubbed'. Stubless muons are simply isolated tracks with associated energy deposits in the calorimeter consistent with

those of a minimum-ionizing particle.

Stubbed muons are reconstructed using the stub-finder algorithm. The hits in the muon detectors (which are drift chambers) are linked by seeding with alternate layers and finding matching hits with remaining layers. The resulting track segments are called muon stubs. The stub-finder works in each of the muon subsystems giving CMU, CMP and CMX stubs. The stub-linking algorithm tries to match a COT track to the stub by minimizing a fit χ^2. A track can be matched to more than one stub, but a stub is matched to at most one COT track. For each stub-track pair, calorimeter information is retrieved and associated with the muon candidate.

3.4.5 Jets

Quarks and gluons undergo fragmentation and create partons via a cascade of gluon emissions and decays. The partons then form colorless hadrons in a process known as hadronization. The unstable hadrons subsequently decay into stable particles which reach the detector and shower in the calorimeter. This cluster of energy in the calorimeter is known as a jet.

The jets are reconstructed with a fixed-cone algorithm, with a cone size of $\Delta R = \sqrt{\Delta\eta^2 + \Delta\phi^2} = 0.4$, where $\Delta\eta = \eta_{\text{centroid}} - \eta_i$, (with a similar definition for $\Delta\phi$) for the ith calorimeter tower. The algorithm selects seed towers with energy > 300 MeV, and associates with them hadronic calorimeter towers with energy > 100 MeV inside the cone. The jet center is recalculated at each step as a E_{T} -weighted centroid. If two jets overlap by more than 75%, then the jets are merged into one.

Each jet has a massless four-momentum associated with it. The magnitude is given by the tower energies, and the 3-momentum points from the center of the detector to the center of the jet. The jet direction is corrected later for the position of the event vertex with respect to the detector center. The jet energy is further corrected [29] (the direction remains unchanged) for the following effects :

- η-dependence : This corrects for the non-uniform η response of the calorimeter. It

accounts for the cracks in the calorimeter at $\eta = 1.0, 1.1$, and 1.5. The transverse spread of the calorimeter shower outside the cone of the jet is also corrected, as is the η dependence of the gluon radiation.

- E_{T} dependence : The calorimeter response to E_{T} is non-linear. The jet energy is corrected for this effect.

- Other : Corrections are also made for pile-up events leading to extra energy associated with jets, instability of the calorimeter energy scale etc.

In this analysis, jets are selected if they satisfy the following criteria : raw jet $E_{\mathrm{T}} >$ 8 GeV, corrected jet $E_{\mathrm{T}} > 15$ GeV, EM fraction < 0.9 [7], and jet $\eta < 2.5$.

3.4.6 Missing Energy

The missing energy is based on calorimeter and is measured in the transverse direction ($\not\!\!E_{\mathrm{T}}$). It is given by the negative sum of all calorimeter towers with energy > 100 MeV, and $|\eta| < 3.6$. $\not\!\!E_{\mathrm{T}}$ is calculated as :

$$\not\!\!E_{\mathrm{T}_x} = -\sum_{i=1}^{N_{\mathrm{towers}}} E_x^i; \quad \not\!\!E_{\mathrm{T}_y} = -\sum_{i=1}^{N_{\mathrm{towers}}} E_y^i \tag{3.2}$$

$$\not\!\!E_{\mathrm{T}} = \sqrt{\not\!\!E_{\mathrm{T}_x}{}^2 + \not\!\!E_{\mathrm{T}_y}{}^2} \tag{3.3}$$

The $\not\!\!E_{\mathrm{T}}$ is a property of the event, and usually cannot be associated with a single particle such as a neutrino. Further corrections to $\not\!\!E_{\mathrm{T}}$ are discussed in Section 3.7.

3.5 Lepton Identification

The selection of leptons in this analysis is driven by the need to maximize acceptance while keeping the backgrounds down. Electrons and muons are selected as described below. In addition to using electrons and muons, sensitivity to the decay of τ-leptons is also desirable.

[7] The fraction of total jet energy deposited in the electromagnetic calorimeter. For hadrons, most of the energy should be deposited in the hadronic calorimeter.

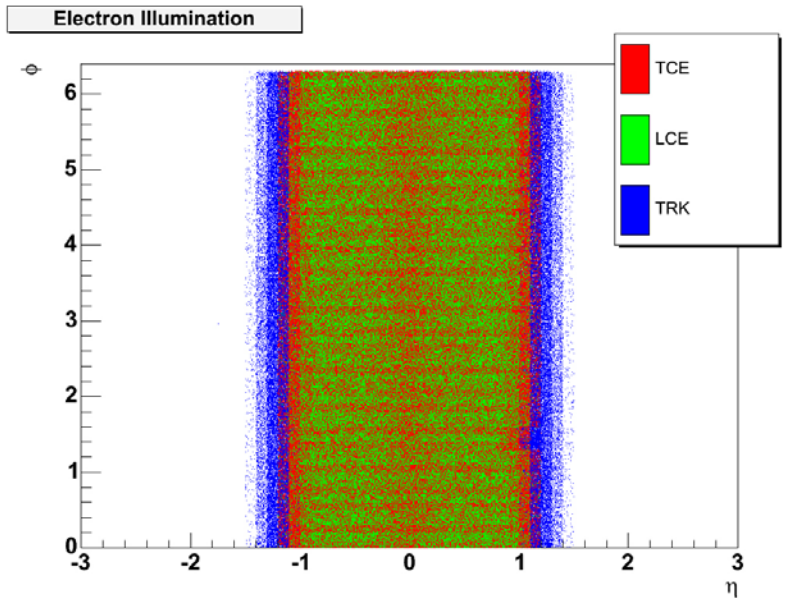

Figure 3.8: Figure shows the illumination for selected electrons in this analysis. In addition, the isolated track illumination is also shown.

It is interesting to note that the single-prong decays of the tau cover 85% of its decays, of which 50% are non-leptonic. In a single-prong decay, the τ decays to a single charged particle (with accompanying neutrinos). An isolated track category of leptons is added to select the hadronic single-prong decays of the τ. The leptonic decays of the τ's are obviously included in the electron and muon selections below.

3.5.1 Electrons

Electrons are selected in two categories, 'tight' and 'loose'. The 'tight' electrons, henceforth called TCE, are selected by imposing all the requirements in Table 3.1. Let us now examine each of the electron selection criteria

- CEM fiducial : The track associated with the electron points towards the fiducial regions of the calorimeter, thus away from any cracks and the central chimney. This ensures good measurement of the electron's energy deposit. The track is also required to originate from the event vertex.

- Had/Em : The ratio of energy deposited by the electron in the hadronic part of the

calorimeter to the electromagnetic part. An electron is expected to shower in the EM calorimeter and thus only a small fraction of its energy is expected to make it to the HAD calorimeter. The ratio is adjusted to take into account that electrons with higher E_{T} will leak more energy into the hadronic calorimeter.

- E/p : The ratio of the electron's energy to its momentum. For electrons, this ratio is expected to be close to one. For hadronic tracks with associated π^0's or photons, the energy deposited in the calorimeter will be higher than the associated track momentum, and thus this selection will remove such hadronic tracks.

- Lshr : The shower shape of the electron in the calorimeter is compared with to the same from the test beam data. The comparison is quantified as the variable Lshr

$$\mathrm{Lshr} = 0.14 \times \sum_i \frac{E_i - E_i^{exp}}{\sqrt{0.14^2 \times E_{\mathrm{cluster}} \times (\Delta E_i^{exp})^2}} \tag{3.4}$$

where E_i is the energy deposited in the ith tower, E_i^{exp} is the expected energy deposited in the tower based on test beam data, ΔE_i^{exp} is the uncertainty, and E_{cluster} is the energy of the electromagnetic cluster and the sum run overs the adjacent towers to the seed tower.

- Charge$\times\Delta X$, $|\Delta Z|$: The matching of the extrapolated track to the CES cluster is done in the two coordinates x and z.

- CES χ^2_{strip} : The CES shower shape is compared to templates and the comparison is quantified by this χ^2.

- The number of axial [NAxialSeg(5)] and stereo [NStereoSeg(5)] segments with at least 5 COT hits each determine the quality of the track associated with the electron.

- Isolation : The electrons in this analysis are expected to be away from any other particles. The isolation requirement is the ratio of extraneous energy around the electron to its energy and is calorimeter based; it is the ratio of the energy in towers

in a η-ϕ cone of 0.4 around the electron to the energy of the electron. It is corrected for expected leakage of the electron energy into the neighbouring towers.

The 'loose' electrons, henceforth called LCE, are selected by imposing only the right part of the requirements in Table 3.1. The electrons are also required to originate from the event vertex by requiring the z coordinates to be within 5 cm. Figure 3.9 shows the distributions for some of the identification variables for TCE's after every other selection is made[8]. The TCE's are triggerable and have smaller backgrounds. The LCE's, while being more efficiently selected, have higher backgrounds. See Section 4.4.2 for the fake rates for TCE and LCE. Figure 3.8 shows the electron illumination for TCE's and LCE's.

A potential source of contamination to the electrons thus selected is those coming from photon conversions. The conversions are removed using a dedicated algorithm, which checks the electron's track with every other track in the event to determine if the pair is consistent as having come from a photon. Figure 3.10 shows the selection criteria for tagging conversions, the separation S_{xy} and $\Delta\cot\theta$ plotted for electron candidates.

3.5.2 Muons

Muons are selected in three categories. The first two categories, CMUP and CMX are defined by the specific locations of the muons in our detector, see Fig. 3.12. The CMUP selection consists of ensuring that the muon candidate is fiducial to two muon detector subsystems, the CMU and the CMP. The third muon category, CMIO muons, are "stubless" muons, meaning there is no signal in any of the muon chambers which corresponds to this muon candidate. The requirements on the selection of all three categories of muons are shown in Table 3.2.

The CMUP and CMX muons can be thought of as the muon counterparts to the TCE, while CMIO is the muon counterpart to the LCE[9]. Thus a tight muon refers to the CMUP,

[8]For example, the Had/Em is shown after every identification criteria except Had/Em is applied

[9]The CMIO muon also differs from the CMUP,CMX muons in the sense that since it is stubless, it suffers

Tight Electron Identification
CEM fiducial, Track $\lvert z_0 \rvert < 60$ cm
Track $\lvert z_0 \rvert$ - Event Vertex $\lvert z_0 \rvert < 5$ cm
$E_T \geq 5$ GeV, $P_T \geq 4$ GeV
Had/Em $< 0.055 + 0.00045 \times$ Em/GeV
E/$p < 2$ if Track $p_T < 50$ GeV
Lshr < 0.2
-3 cm $<$ charge $\times \Delta X < 1.5$ cm
$\lvert \Delta Z \rvert < 3$ cm
CES $\chi^2_{\text{strip}} < 10$
NAxialSeg(5) ≥ 3, NStereoSeg(5) ≥ 2
if $\mathrm{E_T} > 20$, fractional isolation < 0.1
if $\mathrm{E_T} < 20$, isolation energy < 2 GeV

Loose Electron Identification
CEM fiducial, Track $\lvert z_0 \rvert < 60$ cm
Track $\lvert z_0 \rvert$ - Event Vertex $\lvert z_0 \rvert < 5$ cm
$E_T \geq 5$ GeV, $P_T \geq 4$ GeV
Had/Em $< 0.055 + 0.00045 \times$ EmE/GeV
NAxialSeg(5) ≥ 3, NStereoSeg(5) ≥ 2
CES $\chi^2_{\text{strip}} < 20$
fractional isolation < 0.1

Table 3.1: Electron Identification cuts, left for TCE, right for LCE.

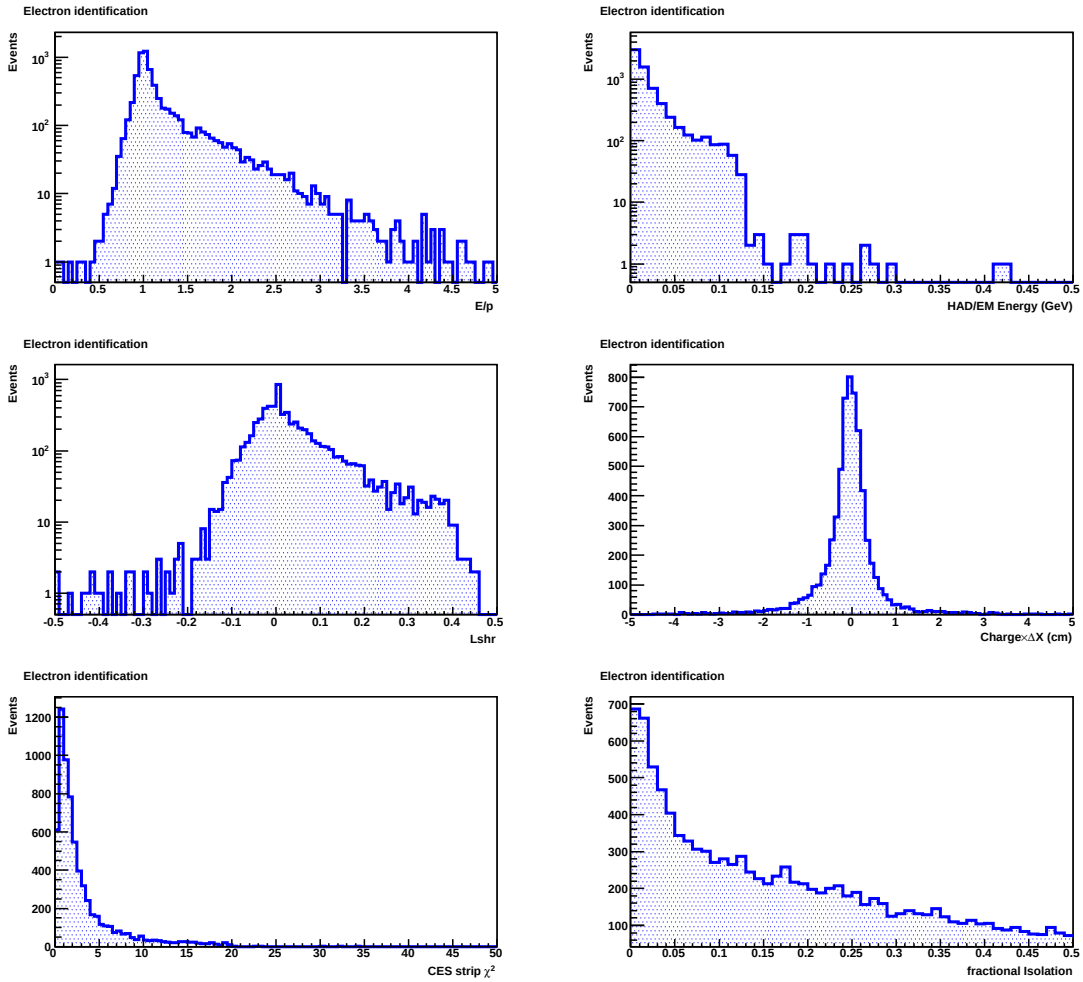

Figure 3.9: Figure shows some of the electron identification variables: E/p, HadE/EmE, Lshr, Charge$\times\Delta X$, CES χ^2, and fractional isolation.

CMX type muons and loose muon refers to the CMIO. The muon selection criteria (see Fig. 3.11) details are :

- ΔX and Track χ^2: These determine how well the candidate muon track extrapolated to the muon chambers matches the muon stub in the respective muon detector. The χ^2 accounts for the errors in the x and ϕ direction.

- Corrected d_0 : The impact parameter of the muon track is used to ensure that the muon originates from the event vertex. The 'correction' is with respect to the actual

from much larger backgrounds and fake rates (Section 4.4.2).

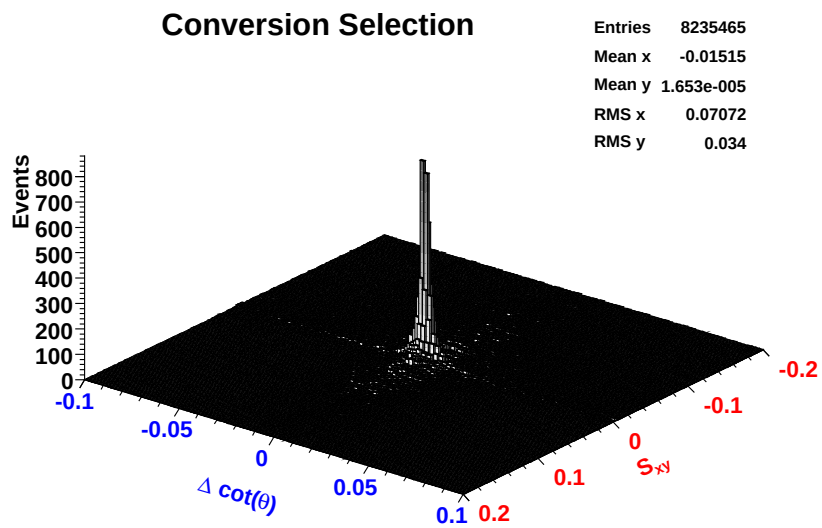

Figure 3.10: Figure shows the conversion tagging selections plotted for all electron candidates, conversions are tagged if $|\Delta\cot\theta| < 0.02$, and $|S_{xy}| < 0.2$. The peak comes from real photon conversions.

beam position.

- NAxialSeg(5) and NStereoSeg(5) are the same variables as for electrons.

- EmEnergy, HadEnergy : The muon, being a minimum ionizing particle, is expected to deposit energy consistent with that in the calorimeter. In addition, to ensure that tracks going in to cracks are not selected, a minimum energy requirement is also imposed. The EmEnergy sliding cut is EmEnergy$< 2.+\max(0., 0.0115*[p-100.])$ GeV, the HadEnergy sliding cut is HadEnergy$< 6. + max(0., 0.028 * [p - 100.])$ GeV, where p is the momentum of the associated track.

- Isolation : The muons, like the electrons, are also expected to be isolated from other particles in the event. The isolation is calculated as the ratio of sum of track momenta around the muon in an η-ϕ cone of 0.4 to the p_{T} of the muon.

An additional point to note is that some electrons (especially LCE) might pass the CMIO selection. Figure 3.13 shows the HadEnergy distribution for muons selected as CMIO's. The

ID Cut	CMUP,CMX	CMIO
$\|\eta\|$	≤ 1.0	≤ 1.0
BCp_{T} (GeV/c)	≥ 5	≥ 10
$Track\|z_0\|$ (cm)	≤ 60	≤ 60
Track $\|z_0\|$ - Event Vertex $\|z_0\|$ (cm)	< 5	< 5
Fiduciality	CMU&CMP or CMX	Not CMUP,CMX
ΔX CMU, CMP, CMX (cm)	$\leq 7, 5, 6$	-
Track χ^2 (Data)	≤ 2.3	≤ 2.3
Corrected d_0 (cm) with(without) Si Hits	$\leq 0.02(0.2)$	$\leq 0.02(0.2)$
NAxialSeg(5)/NStereoSeg(5)	$\geq 3/2$	$\geq 3/3$
Hadronic Energy (GeV)	$\leq$ 6+sliding	$\leq$ 6+sliding
EM Energy (GeV)	$\leq$ 2 +sliding	$\leq$ 2 +sliding
EM+Had Energy (GeV)	≥ 0.1	≥ 0.1
fractional isolation	≤ 0.1	≤ 0.1

Table 3.2: Muon Identification Cuts. BC stands for beam constrained; the muon quantities are recalculated after constraining the muon to originate from the beam spot.

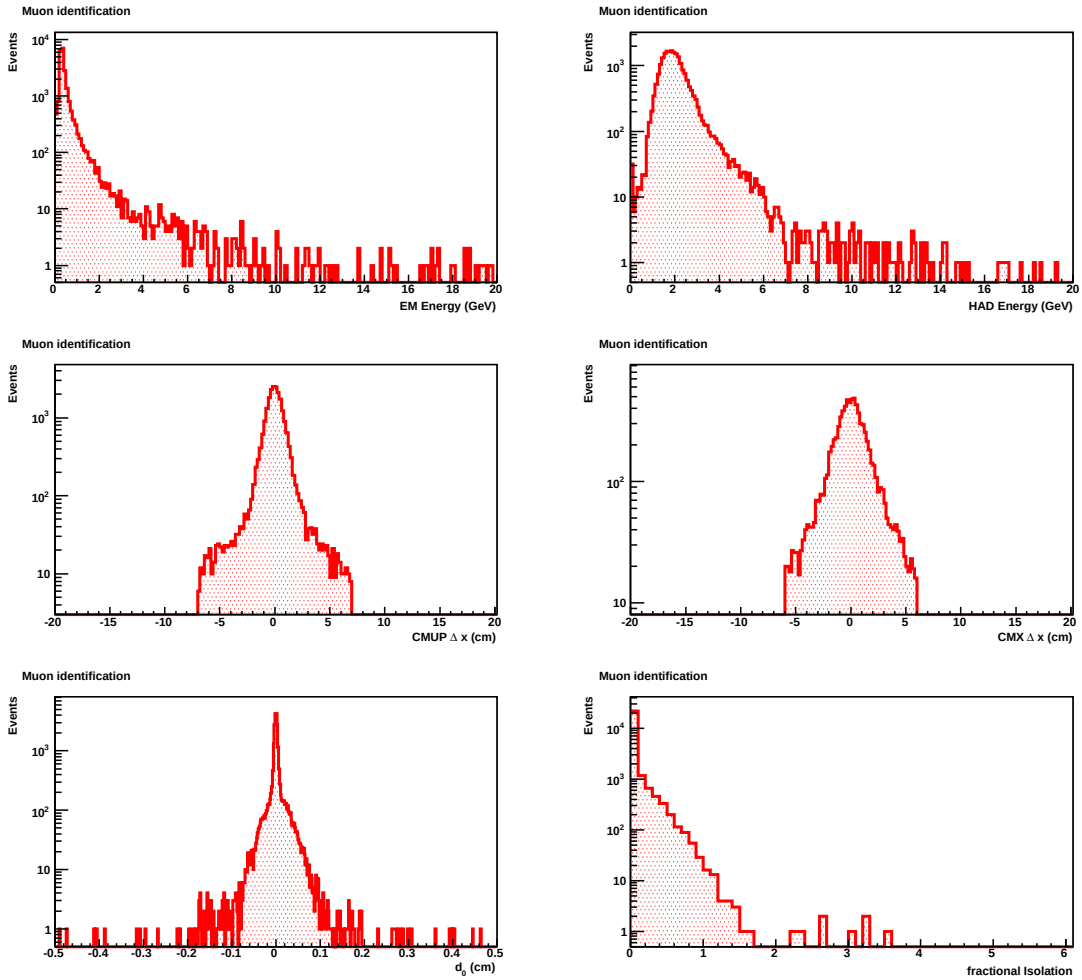

Figure 3.11: Figure shows some of the muon identification variables: EMEnergy, HadEnergy, stub matching ΔX, impact parameter, and fractional isolation.

red and green curves peaking at ∼2 GeV are from real muons in the dimuon Drell-Yan and signal MC samples. The blue curve peaking at ∼0 GeV is from the electrons in dielectron Drell-Yan MC being selected as CMIO muons. The electrons which go in to cracks are most likely to be reconstructed as CMIO muons, but the total energy (EM+Had) requirement will reduce some of these.

3.5.3 Isolated Tracks

Isolated tracks passing requirements listed in Table 3.3 are selected as indicators of hadronic single-prong τ decays. In terms of increasing signal acceptance, the tracks give a significant

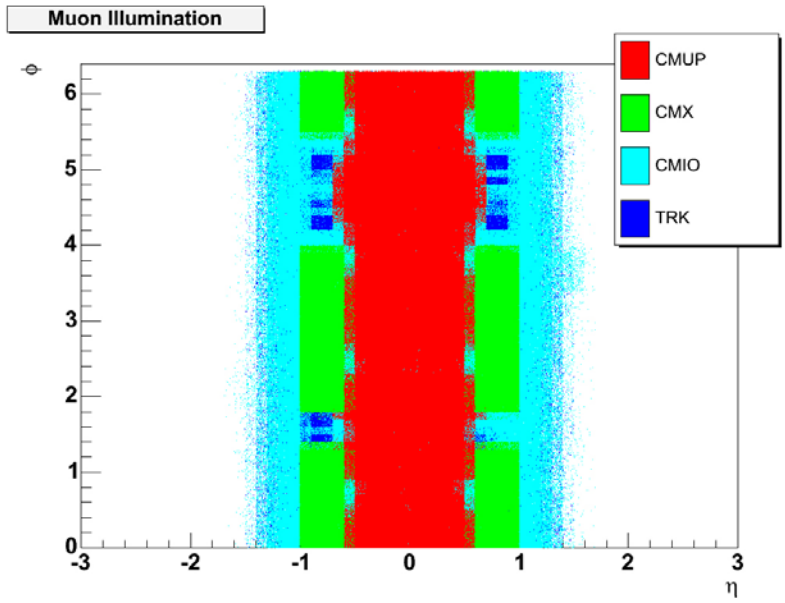

Figure 3.12: Figure shows the illumination for selected muons in this analysis. In addition, the isolated track illumination is also shown.

contribution. Of course, the acceptance of background also increases, but this can be dealt with by imposing selections to reduce background for events with a track. The track isolation is determined in the same way as muons with an additional modification; for the track selection the fractional track isolation is required to be 0. This requirement ensures that there be no tracks with $p_{\mathrm{T}} > 0.4$ GeV around the track in a η-ϕ cone of 0.4. The illumination of the track selection can be seen from Figs. 3.8 and 3.12.

$p_{\mathrm{T}} > 5$ GeV
$\lvert z_0 \rvert < 60$ cm
Track $\lvert z_0 \rvert$ - Event Vertex $\lvert z_0 \rvert < 5$ cm
Number of COT stereo segments with at least 5 hits ≥ 3
Number of COT axial segments with at least 5 hits ≥ 3
fractional track isolation $= 0$

Table 3.3: Isolated track requirements.

One possible extension of the lepton categories is to include higher η leptons, in regions

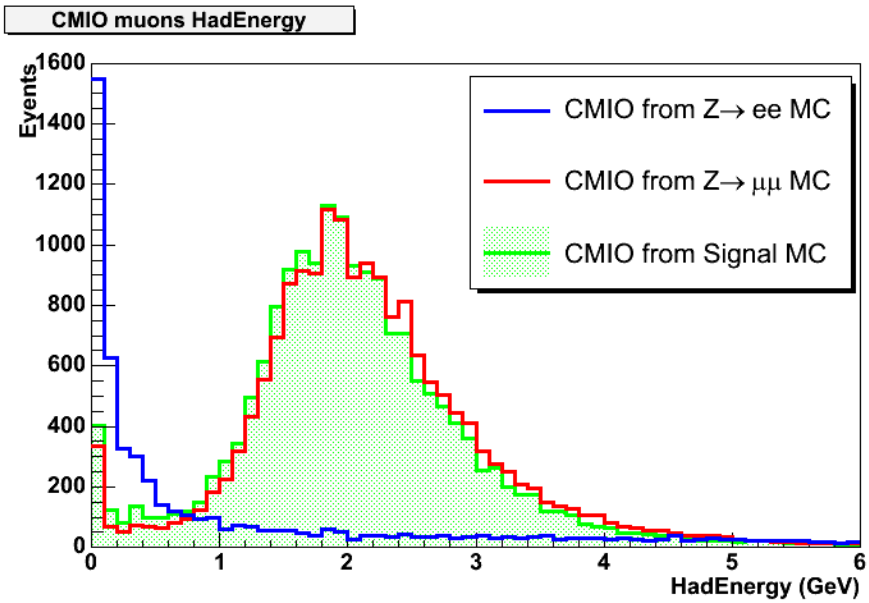

Figure 3.13: The HadE distribution for CMIO muons. The red and green curves are from real muons in $\mu\mu$ Drell-Yan, and signal. The blue curve is the electrons in ee Drell-Yan which pass the CMIO selection.

with $|\eta| > 1$. However, the forward leptons are harder to identify and suffer from higher backgrounds. As an example, the η distribution for generator signal leptons and WZ leptons is shown in Fig. 3.14, normalized for equal area. The background WZ sample is fatter in η than signal.

3.6 Identification scalefactors

The identification efficiencies for leptons are different in data and MC. This means that this difference must be accounted for when using MC samples to make a prediction of data events. The scalefactors, which are the ratio of data efficiency ϵ_{data} to the MC efficiency ϵ_{MC}, are calculated using independent samples. These scalefactors are then used as event weights as described in Section 4.4.1. The amount difference in efficiencies represents a lack of complete understanding of the detector in the simulation. In most cases, the scalefactor is within a few percent of unity. An example of the measurement of the electron scalefactors is shown in Appendix B. The complete list of scalefactors used in this analysis is given in

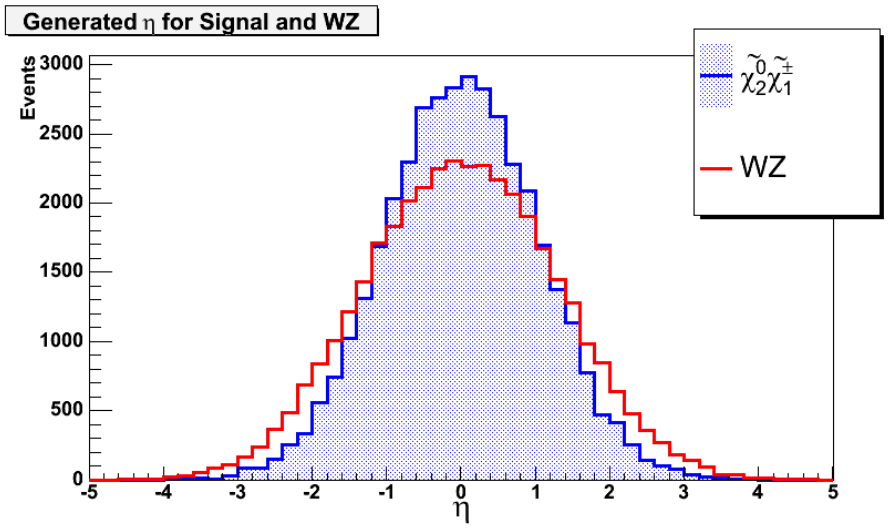

Figure 3.14: Figure shows the lepton η for signal leptons and those from WZ background process.

Table 3.4. Detailed measurements for these scalefactors can be found in Refs. [30, 31, 32, 33, 34, 35, 36, 37, 38]. In addition there is also a mismatch between the efficiency of finding conversions in data and MC. An E_{T} dependent scalefactor as described in Ref. [39] is also used.

3.7 Missing Energy Correction

We expect to get significant missing energy in the trilepton decay of the $\tilde{\chi}_1^\pm$ and $\tilde{\chi}_2^0$ due to the neutrino and the two LSP's. Among the standard model backgrounds, the ones with missing energy are WZ, W+jets, and $t\bar{t}$. However mismeasurement can also lead to missing energy above the analysis threshold.

The $\not{E}_{\mathrm{T}}$ is calculated based on raw tower energies. If jets exist in the event, then their energies will be corrected after raw $\not{E}_{\mathrm{T}}$ has been calculated. The raw $\not{E}_{\mathrm{T}}$ has to be corrected to account for the new jet energies. Muons are minimum-ionizing particles, and do not deposit energy corresponding to their momentum in the calorimeter. The $\not{E}_{\mathrm{T}}$ has to be corrected for the presence of muons in the event.

Figure 3.15 shows the $\not{E}_{\mathrm{T}}$ distribution at the various stages of corrections. The $\not{E}_{\mathrm{T}}$ is

Lepton	E_{T} (p_{T}) range	Scalefactor
TCE	$\geq$ 20 GeV	0.98(0.006)
TCE	8 to 20 GeV	0.96(0.02)
TCE	5 to 8 GeV	0.88(0.16)
LCE	$\geq$ 20 GeV	0.96(0.03)
LCE	8 to 20 GeV	0.97(0.03)
CMUP	$\geq$ 20 GeV/c	0.94(0.006)
CMUP	5 to 20 GeV/c	0.87(0.04)
CMX	$\geq$ 20 GeV/c	0.99(0.01)
CMX	5 to 20 GeV/c	0.88(0.04)
CMIO	$\geq$ 20 GeV/c	1.0(0.01)
CMIO	10 - 20 GeV/c	1.0(0.06)
Trk	$\geq$ 5 GeV/c	1.0(0.002)

Table 3.4: Lepton identification scale factors used in this analysis.

plotted for data which has been collected on a single-muon trigger. From the figure, we can see that the final $\not\!\!E_{\mathrm{T}}$ distribution, labelled as "muons", i.e after correcting for muons, shows contributions from the Drell-Yan process at the low end, as well from W decay at around 40 GeV. Before the corrections are applied, it is not possible to see these features and the raw $\not\!\!E_{\mathrm{T}}$ is quite different from the corrected one.

The correction for muons is as follows

$$\not\!\!E_{T_x}^{corr} = \not\!\!E_{T_x} - (p_{\mathrm{T}}^{\mu} - (\mathrm{EmE}^{\mu} + \mathrm{HadE}^{\mu})/\cosh(\eta)) \times \cos(\phi); \tag{3.5}$$

$$\not\!\!E_{T_y}^{corr} = \not\!\!E_{T_y} - (p_{\mathrm{T}}^{\mu} - (\mathrm{EmE}^{\mu} + \mathrm{HadE}^{\mu})/\cosh(\eta)) \times \sin(\phi); \tag{3.6}$$

$\not\!\!E_{\mathrm{T}}$ is then calculated : $\not\!\!E_{\mathrm{T}} = \sqrt{\not\!\!E_{T_x}^2 + \not\!\!E_{T_y}^2}$, and the direction of $\not\!\!E_{\mathrm{T}}$ is also reevaluated.

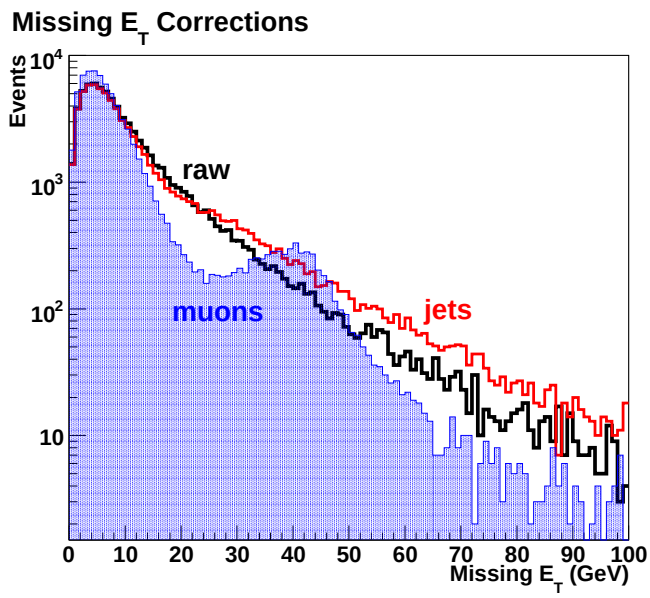

Figure 3.15: Figure shows the $\not\!\!E_{\mathrm{T}}$ in muon triggered data at various stages. Raw (black, open histogram) is the uncorrected $\not\!\!E_{\mathrm{T}}$. Jets (red, open) has $\not\!\!E_{\mathrm{T}}$ corrected for any jets in the event. Muons (blue, hatched) has the final $\not\!\!E_{\mathrm{T}}$ distribution corrected for muons. The distributions have been normalized to have the same area.

The correction for jets is as follows

$$\not\!\!E_{T_x}^{corr} = \not\!\!E_{T_x} - p_{\mathrm{T}}^{\mathrm{jet}} \times \cos(\phi) \times (\text{jet correction factor} - 1.) \tag{3.7}$$

$$\not\!\!E_{T_y}^{corr} = \not\!\!E_{T_y} - p_{\mathrm{T}}^{\mathrm{jet}} \times \sin(\phi) \times (\text{jet correction factor} - 1.) \tag{3.8}$$

where jet correction factor is as described in Section 3.4.5. $\not\!\!E_{\mathrm{T}}$ is then calculated as above and the direction is reevaluated.

Chapter 4

Analysis

The search was conducted as a straightforward counting experiment. This is driven mostly by the number of signal events expected, which is small, and by the fact that there are no resonance peaks that will be evidently found in data.

The counting experiment is carried out in a blind fashion; all selections are fixed *prior* to checking data. The method can be summarized briefly as follows :

- Decide the triggers and datasets to be used for the analysis based on the signature.
- Define preliminary selections and clean-up cuts.

To a certain extent this will also decide which SM backgrounds will be significant.

- Define a set of 'control' regions. The control regions are defined based on selections which will ensure that the signal selected for a control region is negligible. The control regions are to be used to test the background predictions.
- Finalize the selections, which are optimized for discovery of the signal.
- Compute the final expected background from SM and the expected number of signal events.
- Estimate systematic uncertainties.
- Examine the data.

In this chapter we shall examine the first couple of these steps, along with the methods of estimating backgrounds. In the next chapter we shall look at the control regions, in

Chapter 6 we shall discuss the final selections, the systematic uncertainties and the final background and signal predictions.

4.1 Triggers

The trilepton signature has three leptons in the final state, with the p_{T} distribution as shown in Fig. 2.13. Leptons here refers to electrons, muons, or τ-leptons. The e, μ, and the isolated track selection account for 85% of the τ decays as seen in Section 3.5. The choice of triggers follows from the selection of leptons (lepton = e, μ, track).

The presence of three leptons in the final state leads to a choice of dilepton triggers first. As is obvious from the name, two leptons are required for the dilepton triggers. The different dilepton triggers used here are :

- Dielectron trigger DIELECTRON_CEM4 : Requires two central[1] electrons with $E_{\mathrm{T}} >$ 4 GeV, and $p_{\mathrm{T}} > 4$ GeV/c. The detailed requirements are listed in Appendix A.
- Dimuon trigger :
  - DIMUON_CMUCMU4 : Requires two muons with CMU stubs, with $p_{\mathrm{T}} >$ 4 GeV/c.
  - DIMUON_CMUPCMUP4 : Requires two muons with CMU and CMP stubs, with $p_{\mathrm{T}} > 4$ GeV/c.
  - DIMUON_CMU4_CMX4 : Requires two muons, one with CMU stub and one with CMX stub with $p_{\mathrm{T}} > 4$ GeV/c.
  - DIMUON_CMUP4_CMX4 : Requires two muons, one with CMU and CMP stub and one with CMX stub with $p_{\mathrm{T}} > 4$ GeV/c.

For the most part, imposing the dilepton trigger requirements means effectively selecting two tight leptons. Thus only the third lepton can be loose. To overcome this restriction, in

[1] $|\eta| < 1.1$

addition to the dilepton triggers, the single-lepton triggers are also used :

- High p_{T} electron ELECTRON_CENTRAL_18 : Requires a single central electrons with E_{T} >18 GeV, and $p_{\mathrm{T}} > 9$ GeV/c.
- High p_{T} muon :
  - MUON_CMUP18 : Requires a single CMUP muon with $p_{\mathrm{T}} > 18$ GeV/c.
  - MUON_CMX18 : Requires a single CMX muon with $p_{\mathrm{T}} > 18$ GeV/c.

  In addition to these two paths, there are several other muon paths which are variations on these two and are meant for high luminosity running.

The SUSY dilepton trigger paths have different thresholds for the last 191 pb^{-1} of data. The thresholds change from 4, 4 GeV for both leptons, to 8, 4 GeV. However the trigger is fully efficient for the lepton p_{T} thresholds used here(Table 4.1) and there is no effect of the change in thresholds on the trigger efficiency.

The High p_{T} muon triggers require special consideration. The trigger paths for this dataset have changed considerably over the data taking period. The trigger efficiencies are first measured individually and are then corrected for effects such as dynamic prescaling. However, since not all triggers were implemented all the time, accounting must be done for the presence of various paths at different periods in the data. Using the unchanged high-p_{T} electron triggers as a benchmark, the trigger efficiencies of various muon paths are corrected for the fraction of time they were present in the data taking period. For example, if path A was present in the data for only 500 pb^{-1}, then the efficiency of path A (ϵ_A) is

$$\epsilon_A^{corr} = \epsilon_A \times \frac{500}{2000}$$

where 2000 pb^{-1} is the total amount of data we are analyzing. In such a way the corrected efficiencies for the various paths of the High p_{T} muon dataset are obtained.

The trigger efficiencies are listed in Appendix C. These trigger efficiencies are for specific paths. They are applied to MC events as event weights. If $P(A)$ is the probability of A,

the event trigger efficiency is defined as

$$\epsilon_{\text{total}} = 1 - P(\text{Event does not fire any possible trigger}) \tag{4.1}$$

The second term on the right hand side is then just the product of inefficiencies of all the applicable trigger paths. For example, let the dielectron trigger have efficiency ϵ_{ee}, and the single-electron have efficiency ϵ_e. A MC dielectron event (with electrons e, e') which would have fired both triggers then has a total trigger weight

$$1 - (1 - \epsilon_{ee'}) \times (1 - \epsilon_e) \times (1 - \epsilon_{e'}) \tag{4.2}$$

4.2 Preliminary Event Selection

The datasets to be used for the analysis are determined by the trigger paths already discussed. In addition, a "good run" requirement is imposed. The data are collected in "runs", which are short periods of data-taking with exactly the same detector conditions. Only those runs are selected for which the detector components relevant to this analysis were in a stable and working state[2] [40].

Event selection first ensures that one of the chosen trigger paths has fired. This is followed by requiring that there is at least one vertex of good quality in the event, and the highest p_{T} vertex within each event is chosen to be the event vertex. The z_0 of the vertex is required to be within 60 cm of the origin of the CDF detector geometry.

The leptons for the analysis are then selected in the following order : First tight electrons are selected. If an electron candidate does not pass tight requirements, but passes the loose selection, then it is selected as a loose electron. Electron candidates consistent with conversions are removed as described previously. Then tight muons (CMUP,CMX) are selected. In a similar way to electrons, loose muons pass the loose selection, but not the

[2]For example, since the analysis requires electrons and muons, the central calorimeter and muon systems had to be working smoothly for all runs. Since the silicon detector is not a part of the analysis, no requirement was made on the working of the silicon detector.

tight selection. Lastly, isolated tracks are selected, exclusively from the electrons and muons selected above.

In addition to the primary analysis objects (tight/loose electrons, muons and isolated tracks), jets are selected as described in Section 3.4.5. The $\not\!\!E_{\mathrm{T}}$ in the event is then corrected for presence of jets and the selected muons in the event. In cases where the final event selection has an isolated track (Table 4.1), the $\not\!\!E_{\mathrm{T}}$ is also corrected for the isolated track. In some cases, the source of $\not\!\!E_{\mathrm{T}}$ can be jet energy mismeasurement, and the $\not\!\!E_{\mathrm{T}}$-correction for jets will not account for this. To remove events with such fake $\not\!\!E_{\mathrm{T}}$, any events where the $\not\!\!E_{\mathrm{T}}$ and any jet ($E_{\mathrm{T}} > 10$GeV) are azimuthally separated by less than 0.35 radians are rejected. Figure 4.1 shows this angle in dijet events with $\not\!\!E_{\mathrm{T}} > 15$ GeV. Here, the intrinsic $\not\!\!E_{\mathrm{T}}$ is expected to be negligible and any $\not\!\!E_{\mathrm{T}}$ is from mismeasurement. In addition the azimuthal separation between leading lepton and $\not\!\!E_{\mathrm{T}}$ and that between next-to-leading lepton and $\not\!\!E_{\mathrm{T}}$ is required be more than 0.17 rad to remove events where the mismeasured $\not\!\!E_{\mathrm{T}}$ comes from lepton energy mismeasurement. Figure 4.2 shows the distributions of azimuthal separation between leptons and $\not\!\!E_{\mathrm{T}}$ for signal and for Drell Yan events (DY has no intrinsic $\not\!\!E_{\mathrm{T}}$). As seen from the figure, these selections don't result in any significant signal acceptance loss.

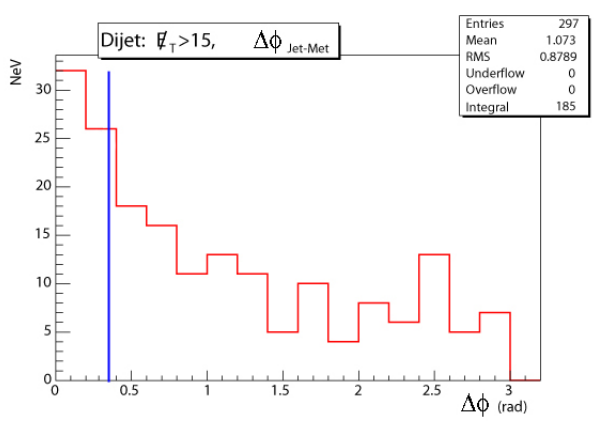

Figure 4.1: Figure shows the azimuthal angle between jets and $\not\!\!E_{\mathrm{T}}$ for dijet events (triggered on a single $E_{\mathrm{T}} > 20$ GeV jet) when $\not\!\!E_{\mathrm{T}} > 15$ GeV. The angle is required to be greater than 0.35 rad.

To remove contributions from the J/ψ and Υ resonances, the invariant mass of the lepton

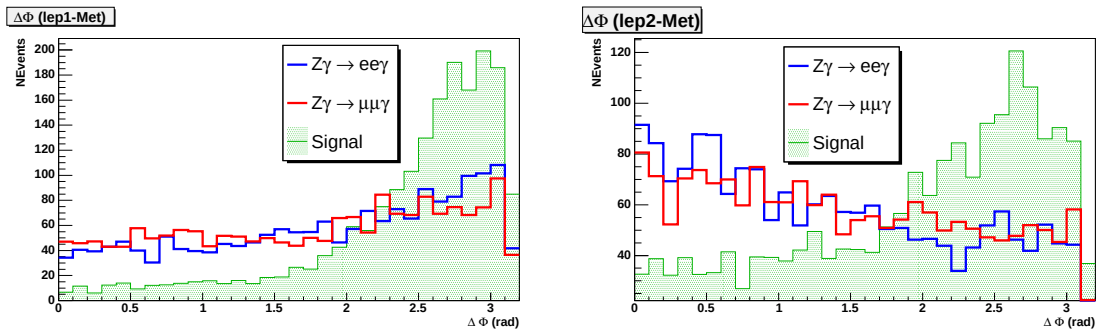

Figure 4.2: Signal and DY distributions for azimuthal angle between leading lepton and $\not\!\!E_{\mathrm{T}}$ on left and next-to-leading lepton and $\not\!\!E_{\mathrm{T}}$ on right. The distributions are normalized to area. We require that this separation be more than 0.17 rad.

pair in dilepton events is required to be above 20 GeV/c^2 [3]. Trilepton events have two opposite-charge pairs (lepton-track pairs included), and thus two opposite-charge masses. The higher of the two masses is required to be at least 20 GeV/c^2, and the lower mass is required to be at least 13 GeV/c^2. Since the third lepton has fairly low p_{T} , it is required to be tightly isolated. This is done by requiring the fractional isolation to be less than 0.1, and the track-isolation[4] to be less than 0.1. Thus for events with three leptons (e's, μ's) the softest lepton is track-isolated, for events with two leptons and a track, the softest lepton or track is track-isolated. Finally, aside from the three primary objects (Table 4.1), no other analysis level object above 10 GeV is allowed in the event.

4.3 Analysis Channels

Once the analysis objects and the preliminary selections are done, the exclusive analysis channels are defined. The events are categorized based on the quality of the lepton objects. The first channel is purest; it requires three tight leptons. If three tight leptons are not found, then one lepton is allowed to be loose. Else, one tight and two loose leptons are selected. If none of these are satisfied, then two dilepton+track channels are selected, first with two tight leptons, then with one tight and one loose lepton. The channels are thus

[3] In addition, the Drell-Yan MC samples are generated with this requirement.

[4] Fractional isolation is ratio of energy in calorimeter around the lepton to the energy of the lepton; track isolation is the ratio of sum of track momenta around track to the momentum of the track.

exclusive from the outset, and are ordered roughly in terms of expected purity of signal. Table 4.1 gives the details of the channels. Table 4.2 gives the channels for dilepton events. The dilepton channels will be used for the control regions as described in the next chapter.

Channel	**Selection**	E_{T} $l^{1,2,3}$ **GeV**
$l_t l_t l_t$	3 tight leptons or 2 tight leptons + 1 loose electron	15, 5, 5
$l_t l_t l_l$	2 tight leptons + 1 CMIO	15,5,10
$l_t l_l l_l$	1 tight leptons + 2 loose leptons	20, 8, 5(10 if CMIO)
$l_t l_t T$	2 tight leptons + 1 isolated track	15, 5, 5
$l_t l_l T$	1 tight + 1 loose lepton + 1 isolated track	20, 8(10 if CMIO), 5

Table 4.1: The exclusive analysis channels.

Channel	**Selection**	E_{T} $l^{1,2,3}$ **GeV**
$l_t l_t$	2 tight leptons	15, 5
$l_t l_l$	1 tight lepton + 1 loose lepton	20, 8(10 if CMIO)

Table 4.2: The exclusive channels for dilepton control regions.

For the rest of this chapter, we shall discuss the methods of estimating backgrounds.

4.4 Background Estimation

The exhaustive list of backgrounds for this analysis based on the preliminary event selection described above is as follows :

- $WZ \rightarrow l^{\pm} l^{\mp} l'^{\pm} \nu$. The WZ background from the leptonic decay of both W and Z bosons has the same signature as signal, viz. three leptons + $\not{E}_{\mathrm{T}}$.
- $ZZ \rightarrow l^{\pm} l^{\mp} l'^{\pm} l'^{\mp}$. The ZZ leptonic decay leads to more than three leptons.
- $WW \rightarrow l^{\pm} \nu l'^{\mp} \nu$
- Drell-Yan : $Z/\gamma* \rightarrow ee, \mu\mu, \tau\tau$
- top-quark pair production : $t\bar{t} \rightarrow W^{\pm} b W^{\mp} \bar{b}$ with the subsequent leptonic decay of the W bosons, and possible semi-leptonic decay of the b-quarks.

The backgrounds can now be classified according to the number of leptons in the final state. Thus WZ and ZZ have three (or more) leptons in the final state and are classified as backgrounds with three real leptons. The dilepton SM sources, such Drell-Yan or WW become a background when there is an additional lepton in the event. This additional or 'fake' lepton can come from three possible sources :

- γ conversion : It is possible that all the $\gamma \to ee$ conversions are not tagged and any residual conversion in the event leads to a third lepton.
- $h^{\pm} \to$ fake : A charged hadron, such as a pion, (or a jet) fakes the signal of an electron or a muon and is thus an additional third lepton.
- U.E.$\to$isolated track : For the channels with an isolated track (Table 4.1), it is possible to obtain an isolated track from the underlying event (U.E.). This will then make a dilepton event from SM processes a background in the dilepton+track channels.

These backgrounds with a fake lepton are classified as dilepton+fake backgrounds. Aside from these two, associated W+jets production can also lead to background when one jet fakes a lepton and an additional isolated track comes from U.E. or a jet. This is mainly a background for the dilepton+track channels.

The $t\bar{t}$ background can have three real leptons in the final state, although the dominant contribution is in the dilepton+fake category.

4.4.1 Three real leptons

The backgrounds with three real leptons are estimated from Monte Carlo (MC) simulated samples. The details of the MC samples are given in Table 4.3. Events are selected in exactly the same way as data. However, there are corrections that need to be done in the MC samples. The efficiencies of identifying leptons is different in data and MC (see Section 3.6). To correct for this, each MC event is weighted by the combined efficiency of

all leptons in the event. The event weight is thus different from one[5].

The event weight is then also corrected for trigger efficiency in data, since MC event selection involves no triggering. The trigger efficiency correction is calculated by considering all the possible ways the event could have satisfied any of the triggers and then combining the efficiencies of the fired triggers.

Once each event has a correct event weight assigned to it, the event weights are summed giving a total event weight which is then normalized to the total data luminosity to obtain a prediction.

4.4.2 Dilepton+Fake Lepton

The dilepton+fake backgrounds are estimated in three ways depending on the source of the fake lepton; jets faking leptons, residual conversions, or underlying event giving isolated tracks (U.E.→isolated tracks).

Jets faking Leptons

The rate at which jets fake leptons is measured in jet-triggered data samples in the following way. Events with more than one jet are selected. The denominator is the number of well-identified jets (or fakeable objects) in the sample. Electrons (tight and loose) are selected and matched to the fakeable objects. This forms the numerator. The electron fake rate (tight and loose) is thus defined as the number of electrons (tight and loose) obtained given a number of fakeable objects. For muons, the fakeable objects are well-identified tracks instead of jets. In each case, the leading jet (or track) is excluded to avoid trigger bias. Figure 4.3 shows the fake rates for electrons and muons. Based on the variation between the various jet samples, there is a 50% systematic uncertainty on the fake rate measurement. It is worth noting that this fake rate includes cases where the intitial state radiation (ISR) photon converts and gives an extra electron.

[5]To be more explicit, 100 MC events, say each with weight 1.05, will be counted as 105 events.

The dilepton+fake contribution from this source is then estimated by selecting events with two well identified leptons and one fakeable object. The fake rate corresponding the fakeable object is then applied to this event as a weight, and the fakeable object is then treated as a real lepton. The event is taken through all the selections and the sum of weights is computed in the same way as Section 4.4.1. The sum of event weights of all such events is the total fake contribution. The contribution from events with one real lepton and two fake leptons is very small, and such 'double-fake' background is ignored. The lepton+track+fake contribution is estimated in the same way by selecting events with a lepton+track first, and then applying the same procedure as above.

Figure 4.4 shows the transverse mass distribution for the identified lepton with $\not{E}_{\mathrm{T}}$ for the $l_t l_t T$ channel for the background where one lepton + track is accompanied by a fake lepton. For reference, the same distributions in Drell-Yan and signal MC are also shown. The contributions from Drell-Yan and W+jets are identifiable in the data $l_t + T$+fake distribution, thus showing that W+jets is an important contribution to the dilepton+track background aside the U.E→isolated track background to be described shortly.

Residual Conversions

The jet fake rate method described above includes contributions from ISR. However, the case where one of the two leptons radiates a photon (bremsstrahlung) which converts is not covered by the fake rate. To account for the backgrounds arising from untagged conversions of bremsstrahlung photons or final state radiation photons, the corresponding MC samples are used. For example, to account for the Drell-Yan ($Z\gamma$) background, a $Z\gamma$ MC sample is used. Events are required to have a bremsstrahlung photon, and then the event is analyzed in the same way as described in Section 4.4.1.

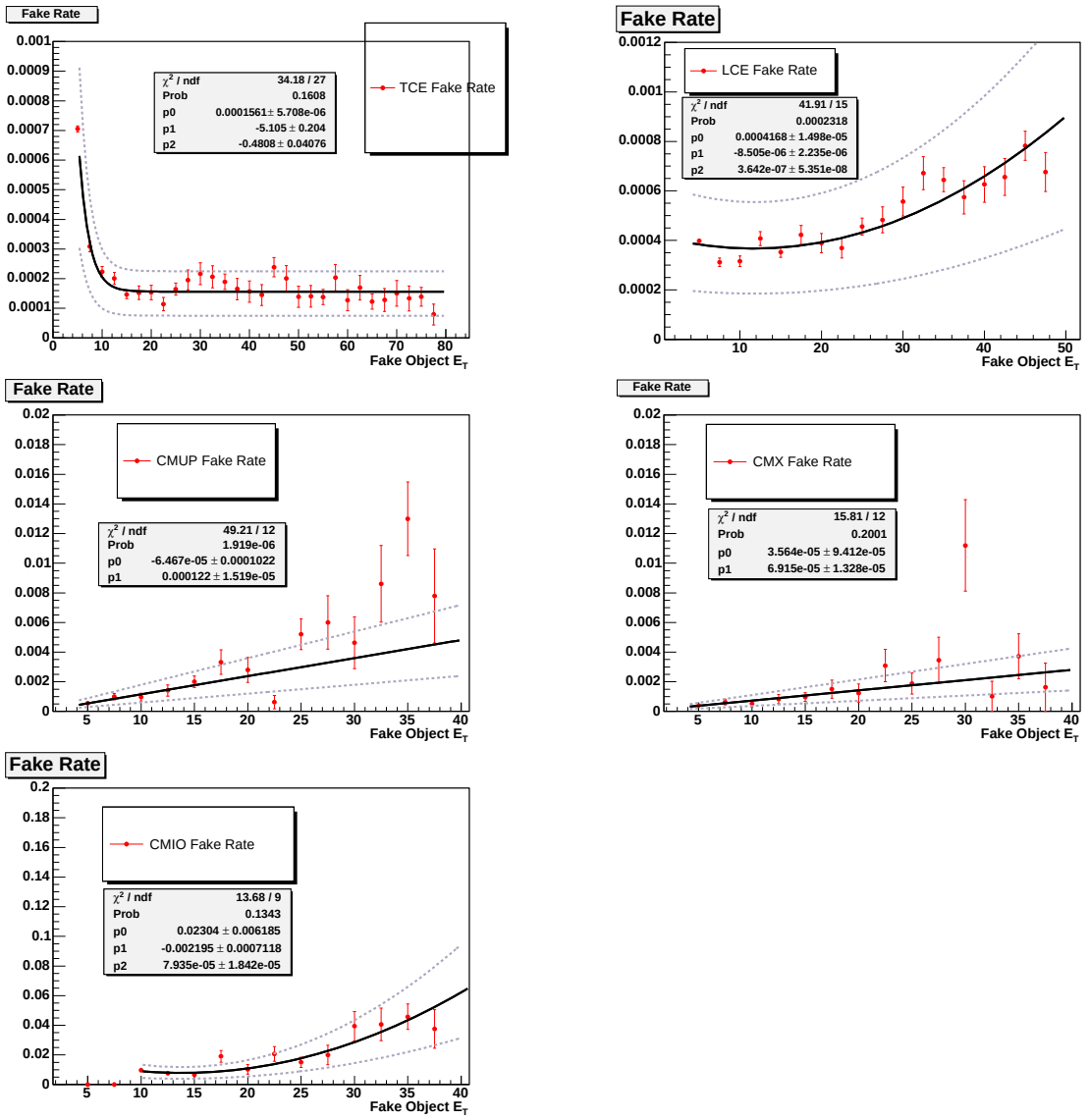

Figure 4.3: Figure shows the fake rates for top left: tight electron, top right: loose electron, middle left: CMUP muons, middle right:CMX muons, bottom: CMIO muons. Fits to the points are shown along with the 50% systematic that we take.

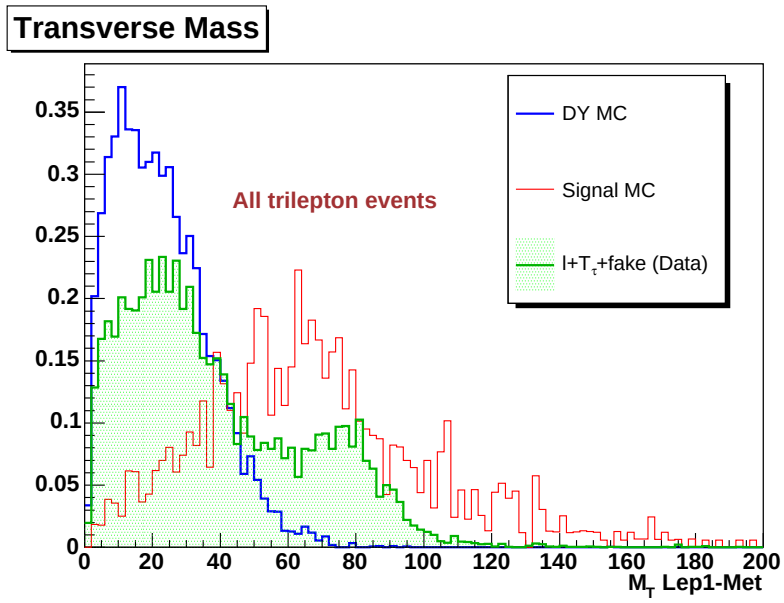

Figure 4.4: Figure shows the transverse mass distribution of leading lepton and $\not\!\!E_{\rm T}$ for all $l_t l_t T$ events with the 'fake' lepton background in green ($l_t + T$+fake). For reference, the DY and signal MC is also shown. More details are in the text.

U.E.→isolated track

The backgrounds with two real leptons and an isolated track from the underlying event are estimated using the isolated track rate (ITR) method developed for this analysis. The ITR is measured in the Z data sample as a function of the number of tracks in the event. The measurement procedure is:

- Select $Z \to ee$ and $Z \to \mu\mu$ events with two tight leptons or one tight + one loose lepton. The invariant mass of the lepton pair must satisfy $|M_{ll} - 91.2| < 15$ GeV.
- Require $\not\!\!E_{\rm T} < 10$ GeV to remove WZ and $t\bar{t}$ contributions. All other SM contributions are negligible.
- Count the number of events with at least one extra isolated track as a function of number of good tracks (NAxialSeg(5)>2, NStereoSeg(5)> 2, $p_{\rm T} > 4$ GeV, $|z_0| <$ 60 cm, and within 5 cm of event vertex) excluding the two tracks which form the Z.
- As a systematic check, the ITR is also measured as a function of the sum of $E_{\rm T}$'s of

all jets in the event.

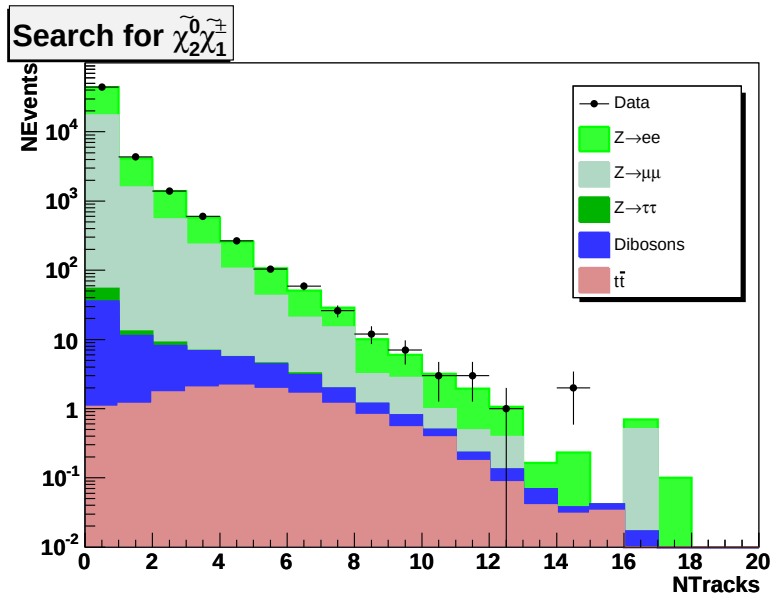

Figure 4.5: Track multiplicity in the $l_t l_t$ channel for Z events. Z selection is discussed elsewhere in the text.

Figure 4.5 shows the track multiplicity distributions for the Z events. Figure 4.6 shows the Isolated Track Rate (ITR) for the Z data. The track rate is fit with a straight line for events with more than two tracks.

To estimate the number of dilepton+track events in our sample, the ITR measured with data Z events is applied to MC as follows:

- The MC events must have two leptons as described before (both tight, or one tight+one loose).
- If there is no third isolated track in the event or the isolated track is not matched to a lepton at generator level, the ITR is applied to the MC event as a weight.

The measured ITR from Z data is applicable to DY, WW, WZ, and ZZ events. The event acceptance is :

$$A_{event} = \frac{(N_{3lep}^{cut} * \epsilon_{3lep}^{cut} + N_{3lep}^{cut}/N_{3lep}^{base} * N_{dilep} * \epsilon_{dilep})}{N_{gen}}, \tag{4.3}$$

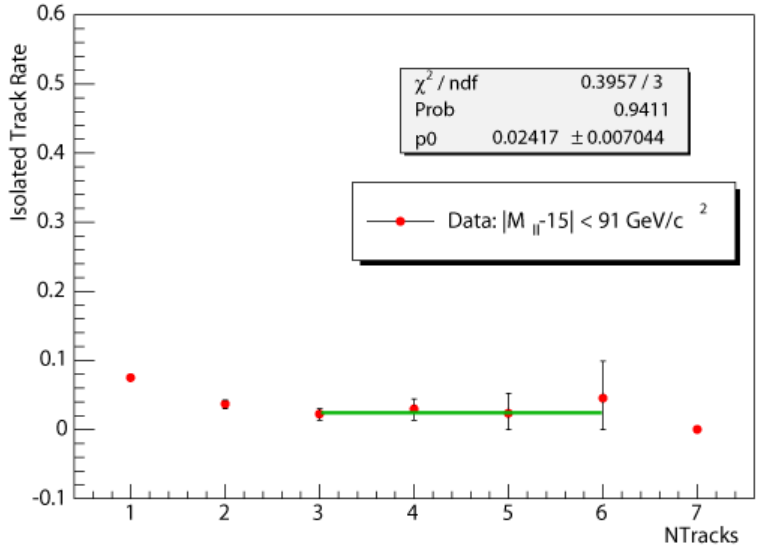

Figure 4.6: Isolated track rate in Z events. The fit is ITR(NTrk)=p_0 for NTrk>2. For NTrk=1, the track rate is $= 0.075 \pm 0.005$. For NTrk=2, the track rate is $= 0.037 \pm 0.006$.

where ϵ is the average event weight, "*base*" stands for dilepton+track selection, and "*cut*" stands for additional selections on top of the "*base*" selection. Therefore $N_{3lep}^{cut}/N_{3lep}^{base}$ stands for the efficiency for a particular optimized cut for an event with 2 leptons and a track. The corresponding ϵ_{3lep}^{cut} is the average event weight for events passing the "*cut*". The average event weight includes lepton identification scale factors and trigger efficiency as in Section 4.4.1. "N_{gen}" is the number of generated MC events. "N_{dilep}" stands for dilepton only events. ϵ_{dilep} includes the ITR weight in addition to lepton identification scale factor and trigger efficiency. The error on A_{event} is then propagated with the errors of individual ϵ and the binomial errors of N_{3lep}^{cut}/N_{gen}, $N_{3lep}^{cut}/N_{3lep}^{base}$, and N_{dilep}/N_{gen}.

4.4.3 Monte Carlo Samples

The Monte Carlo samples used for this analysis are listed in Table 4.3 along with the relevant details.

For signal events, the SUSY mass spectrum is obtained from ISAJET 7.51 [11] followed by

Sample	σ (pb)	Sample Lum.(fb^{-1})
Nominal Signal Point	0.5	218
DY, Z$\rightarrow ee$	355*1.4	20
DY, Z$\rightarrow \mu\mu$	355*1.4	20
DY, Z$\rightarrow \tau\tau$	355*1.4	19
Z$\gamma \rightarrow ee\gamma$	10.33*1.36	409
Z$\gamma \rightarrow \mu\mu\gamma$	10.33*1.36	405
Z$\gamma \rightarrow \tau\tau\gamma$	10.33*1.36	408
WW	1.27	404
WZ	0.208	560
ZZ	2.116	493
$t\bar{t}$	6.9	593

Table 4.3: Cross section for the signal points is calculated using PROSPINO [12]. The diboson backgrounds WW, ZZ, and WZ include off-shell bosons.

hard scattering in PYTHIA 6.216 [41]. For the WZ background, MADEVENT [42] is used[6]. All other background samples are generated using PYTHIA. In each MC sample, hadronization is done using PYTHIA followed by a detailed detector simulation using GEANT3 [43]. The CTEQ5L [44] parton distribution functions (PDF) are used for all generators.

[6]Unlike PYTHIA, MADEVENT generates the off-shell Z boson.

Chapter 5

Control Regions

An important step in a counting experiment is testing the validity of the background estimates. This is usually carried out by means of control regions. Control region are defined such that there is minimal or negligible contamination from signal; in other words, a control region is dominated by background. Multiple control regions can be devised to test different background contributions or specific background estimation methods. Here, the control regions are defined for two basic selections : dilepton events (lepton=e,μ), and trilepton events (including dilepton+track). The control regions are categorized by two variables, the invariant mass of lepton-lepton (or lepton-track) pairs, and the $\not\!\!E_{\mathrm{T}}$ in the event.

The control regions are defined for two sets; dilepton events, and trilepton events. The dilepton control regions have high statistics and are used to test luminosity measurement, lepton identification scalefactors, trigger efficiencies and the combination of different datasets. The trilepton control regions have worse statistics than dilepton ones, but are used to test the background estimation methods, the fake rate measurements and so on.

5.1 Dilepton Control Region

The dilepton control regions are defined in terms of the dilepton pair invariant mass, and the $\not\!\!E_{\mathrm{T}}$ in the event. Figure 5.1 shows the schematic for the dilepton control regions. Events are classified into two regions based on invariant mass :

1) invariant mass in the Z window ($|M_{ll} - 91| < 15$ GeV/c^2, i.e $76 < \frac{M_l l}{\mathrm{GeV}/c^2} < 106$, denoted by "$Z$" and

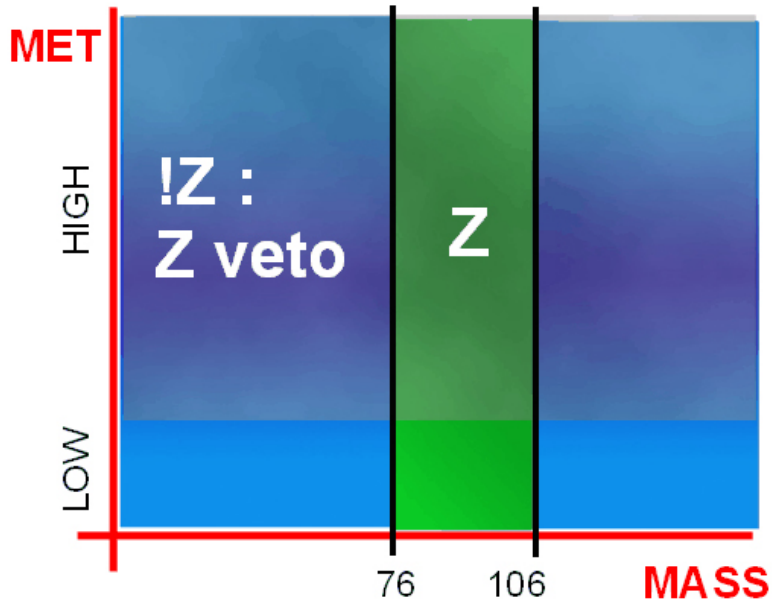

Figure 5.1: Figure illustrates the dilepton control regions. See text for details.

2) invariant mass outside the Z window, denoted by "!Z", or "Z-veto".

Events are also classified into two $\not\!\!E_{\mathrm{T}}$ regions :

1) low-$\not\!\!E_{\mathrm{T}}$ ($\not\!\!E_{\mathrm{T}} < 10$ GeV), and

2) high-$\not\!\!E_{\mathrm{T}}$ ($\not\!\!E_{\mathrm{T}} > 15$ GeV).

Combinations of these selections give the different control regions. For example "!Zlo" stands for events with dilepton mass outside Z window and with $\not\!\!E_{\mathrm{T}} < 10$ GeV, while "Zhi" stands for events in the Z mass window with $\not\!\!E_{\mathrm{T}} > 15$ GeV.

The contribution from signal is small in each of these control regions. For example, the maximum signal contribution would be in the "!Zhi" control region; it is ~ 10 events while SM background prediction is 1758$\pm$80 events.

In addition to these classifications, the dilepton events are further split into the dilepton channels described in Table 4.2; viz. two tight leptons, or one tight + one loose lepton. The events can be further split into dielectron events, dimuon events or $e\mu$ events. In case of $e\mu$ events, the statistics precludes splitting into different control regions. Instead, the combined contributions are presented. To estimate the backgrounds from cases where there

is one real lepton and one fake lepton, the number of same-charge events is subtracted from the number of opposite-charge events, since the fake lepton contribution is expected to be same for either charge. Thus the *dilepton* numbers presented are opposite charge − same charge.

Table 5.1 shows the results of the exhaustive dilepton control region studies for the $l_t l_t$ channel, Table 5.2 shows the results for the $l_t l_l$ channel. Figure 5.2 shows the dilepton ($l_t l_t = ee, \mu\mu, e\mu$) invariant mass distribution for events with $\not{E}_{\mathrm{T}} < 10$ GeV. The SM backgrounds are shown as stacked histograms, and the data is shown as black points with statistical errors. The dominant contribution is from Drell-Yan, with some contribution seen from ZZ production (indicated as Diboson, in blue). The data agrees well with the background prediction. Figure 5.3 shows the $\not{E}_{\mathrm{T}}$ distribution for all dilepton($l_t l_t = ee, \mu\mu, e\mu$) events in the Z mass window. At the low end, Drell-Yan once again is the dominant background. At high $\not{E}_{\mathrm{T}}$, there are contributions from WZ, and some from $t\bar{t}$ production. The data (black points) agrees well with the SM predictions, which gives us confidence in the corrections applied to $\not{E}_{\mathrm{T}}$. There is however a slight tail in the data distribution which is interesting, but will not be examined further here.

Figure 5.4 (electrons) and Figure 5.5 (muons) show a few kinematic distributions in the "!Z" control region. Figure 5.6 (electrons) and Figure 5.7 (muons) show the distributions in the "Z" control region.

5.1.1 Summary of dilepton control regions

The dilepton control regions have high statistics. These control regions test the luminosity estimates (number of Z's), and the lepton identification efficiency measurements. In addition, the control regions also test if the combination of various datasets and trigger paths is done correctly. The dilepton control regions show good agreement between SM background predictions and the observations in data. Figure 5.8 shows the agreement in a visual way. For each channel and control region, the difference between observation and expectation is

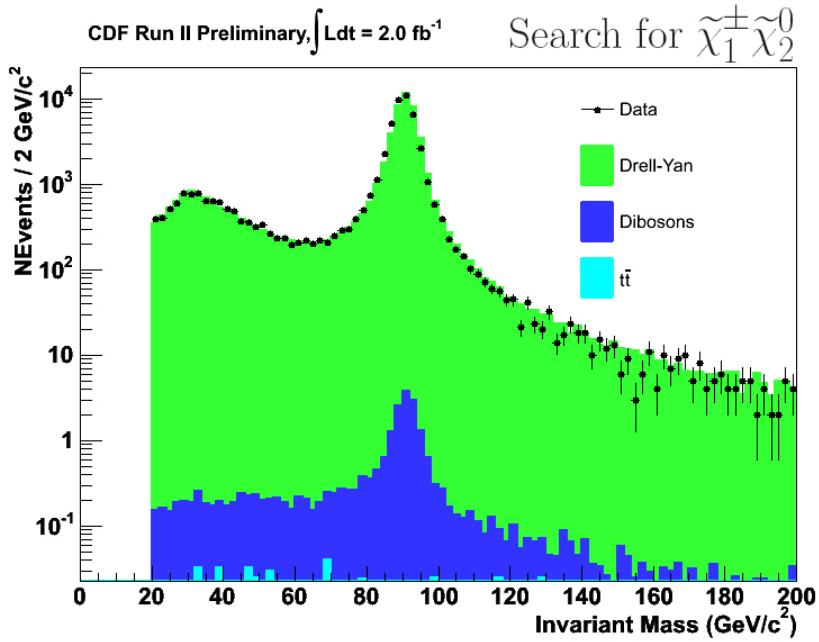

Figure 5.2: Figure shows the dilepton invariant mass distribution for events with $\not\!\!E_T <$ 10 GeV.

Name	$Z(ee)$	$Z(\mu\mu)$	$Z(\tau\tau)$	WW	WZ	ZZ	$t\bar{t}$	Bkgd	Data
tt									
!Z	9847.8	5034.7	1310.2	93.3	1.6	7.1	57.1	16352 ± 716	15966
!Zlo	7705.6	4240.6	477.7	4.7	0.1	2.3	1.0	12432 ± 569	12352
!Zhi	858.4	205.5	550.3	83.5	1.4	3.6	55.0	1758 ± 80	1612
Z	31178.2	19870.4	21.9	22.4	6.3	35.8	15.0	51150 ± 2034	51042
Zlo	25577.6	16665.6	11.1	1.6	0.2	13.4	0.2	42270 ± 1682	42093
Zhi	1261.1	741.5	6.4	19.0	5.8	15.9	14.4	2064 ± 92	2143
lo	33349.6	20903.9	488.7	6.3	0.3	15.7	1.2	54766 ± 2212	54445
Z(ee)	31178.3	0.0	6.7	6.5	4.0	21.9	4.7	31222 ± 1710	31074
Z($\mu\mu$)	0.0	19867.7	3.9	4.6	2.3	13.9	3.0	19895 ± 1102	19942
!Z(ee)	9847.9	0.0	497.8	29.9	1.1	4.3	18.3	10399 ± 617	10033
!Z($\mu\mu$)	0.0	5015.4	243.2	18.2	0.4	2.3	10.9	5290 ± 352	5198
eμ	-0.2	21.9	580.4	56.5	0.1	0.5	35.1	694 ± 47	761

Table 5.1: Table shows the control region numbers for all dilepton control regions for the $l_t l_t$ channel. Errors include MC statistics, and partial systematics such as lepton identification, trigger efficiencies and a Drell-Yan cross-section uncertainty of 5% .

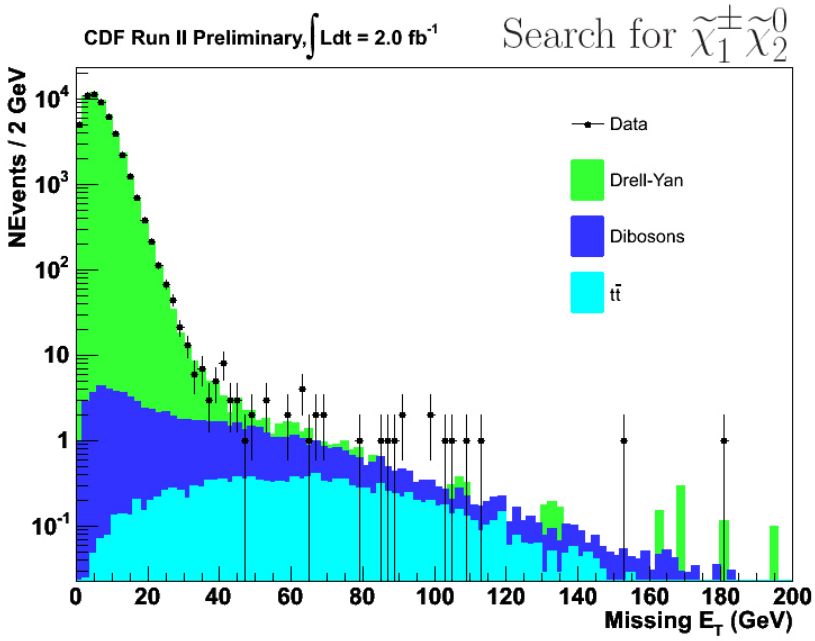

Figure 5.3: Figure shows the $\not\!\!E_{\mathrm{T}}$ distribution for events with dilepton mass in the Z window.

Name	$Z(ee)$	$Z(\mu\mu)$	$Z(\tau\tau)$	WW	WZ	ZZ	$t\bar{t}$	Bkgd	Data
tl									
!Z	1979.7	4360.1	740.7	69.5	0.4	3.8	44.1	7198 ± 300	7069
!Zlo	1281.8	3516.7	318.8	3.5	0.0	1.3	0.8	5123 ± 234	5147
!Zhi	383.1	258.1	259.7	62.2	0.4	1.9	42.4	1008 ± 46	976
Z	11245.7	30953.7	24.0	19.6	4.7	27.1	13.1	42288 ± 1868	41833
Zlo	9061.3	25901.2	13.7	1.5	0.2	10.2	0.3	34988 ± 1557	35055
Zhi	538.4	1177.5	6.6	16.7	4.3	12.0	12.5	1768 ± 85	1616
lo	10342.5	29417.5	332.5	5.0	0.2	11.4	1.0	40110 ± 1776	40202
Z(ee)	10572.3	0.0	5.5	2.8	1.3	7.0	1.9	10591 ± 664	10235
Z($\mu\mu$)	0.0	30906.7	6.5	6.5	3.4	19.6	4.2	30947 ± 1728	30958
!Z(ee)	1706.5	0.0	132.0	9.2	0.1	1.1	6.0	1855 ± 114	1890
!Z($\mu\mu$)	0.0	4285.8	223.9	23.1	0.3	2.4	14.2	4550 ± 261	4482
eμ	946.1	121.3	396.9	47.5	0.1	0.8	30.8	1543 ± 72	1337

Table 5.2: Table shows the control region numbers for all dilepton control regions for the $l_t l_l$ channel. Errors include MC statistics, and partial systematics such as lepton identification, trigger efficiencies and a Drell-Yan cross-section uncertainty of 5% .

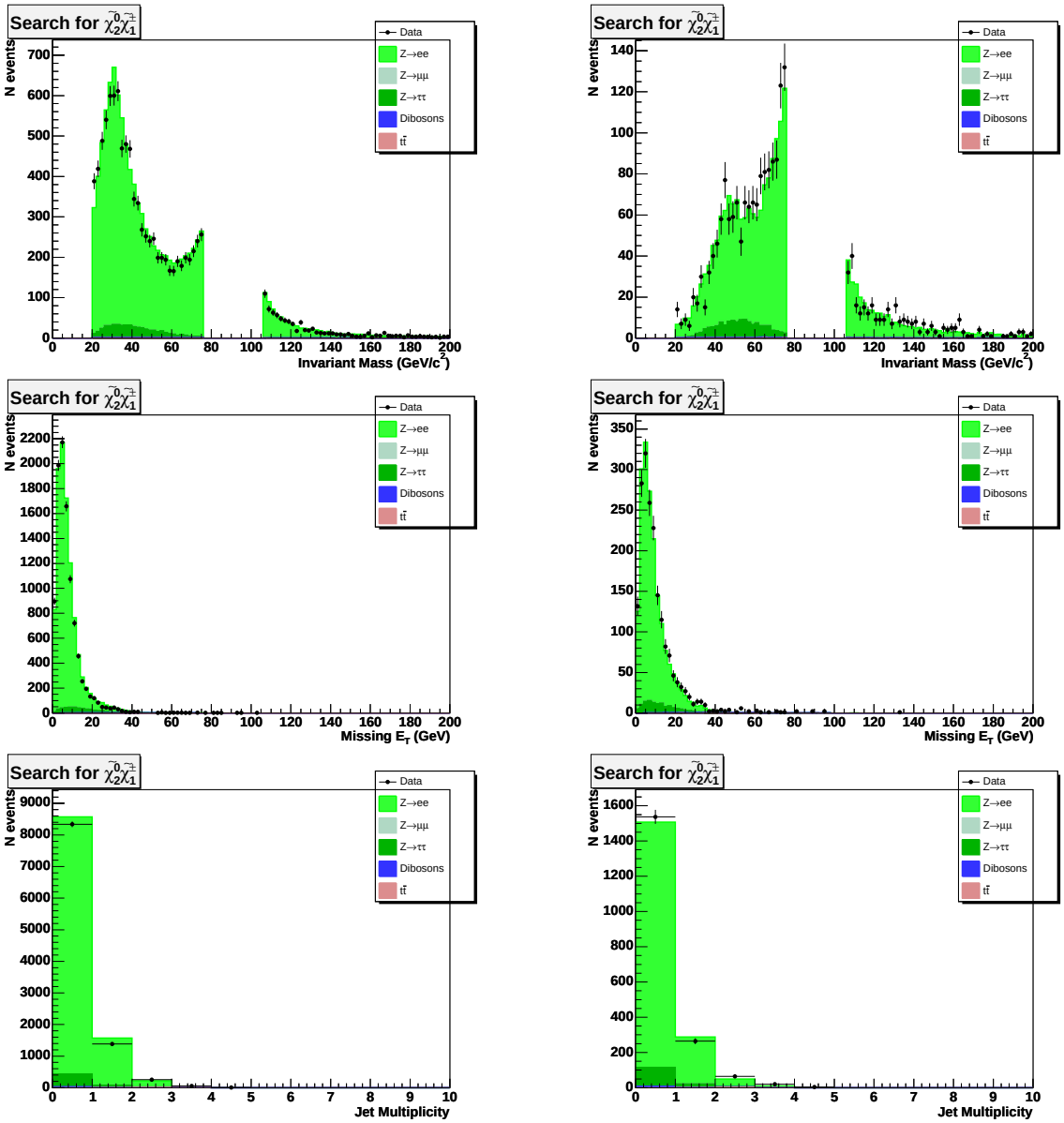

Figure 5.4: M_{os}, $\not{E}_{\mathrm{T}}$, and NJets distributions in control region !Z with 2 tight electrons on left and 1 tight + 1 loose electron on right. Points are data and stacked histograms are background expectation.

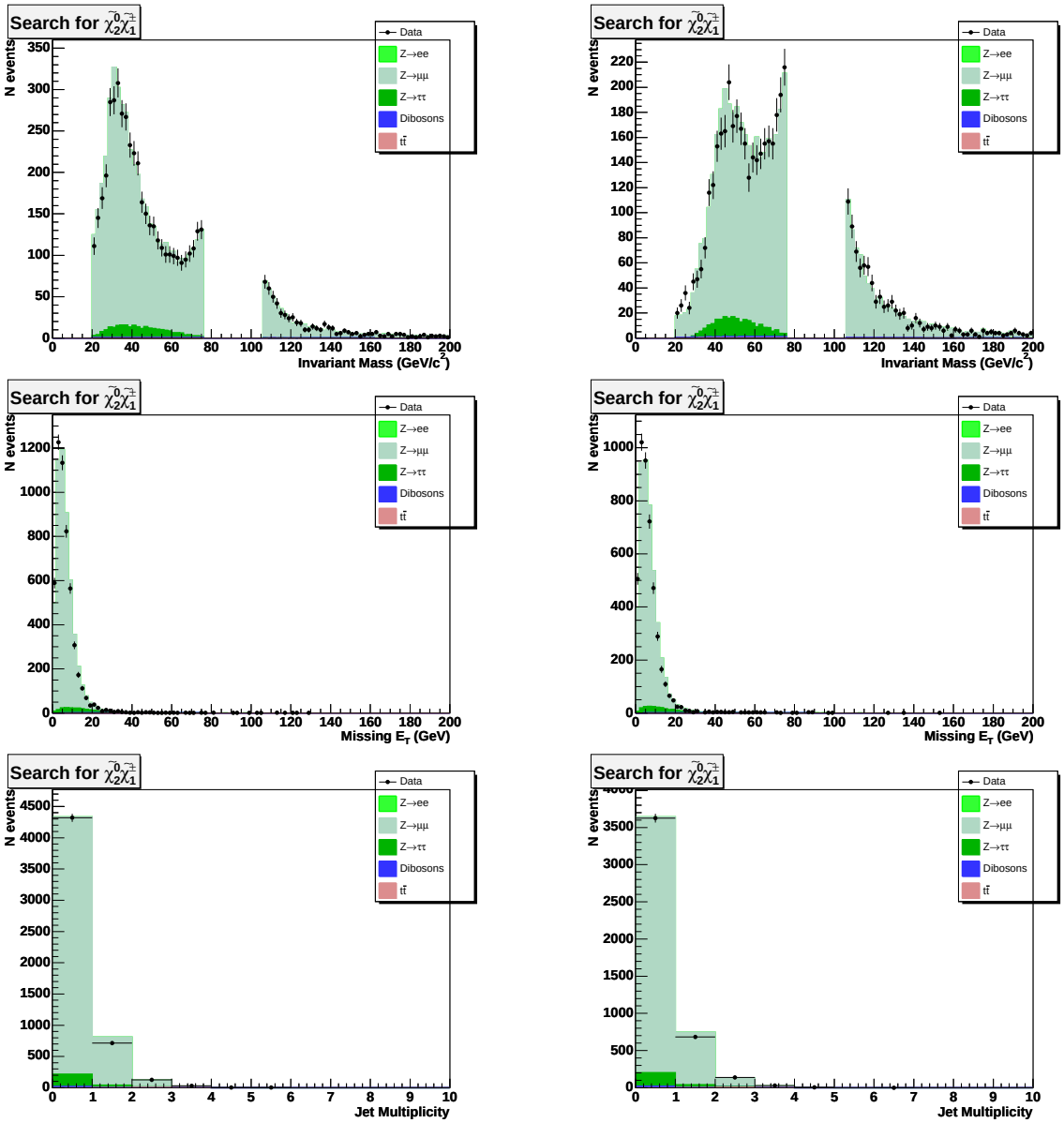

Figure 5.5: M_{os}, $\not\!\!E_{\mathrm{T}}$, and NJets distributions in control region !Z with 2 tight muons on left and 1 tight + 1 loose muon on right. Points are data and stacked histograms are background expectation.

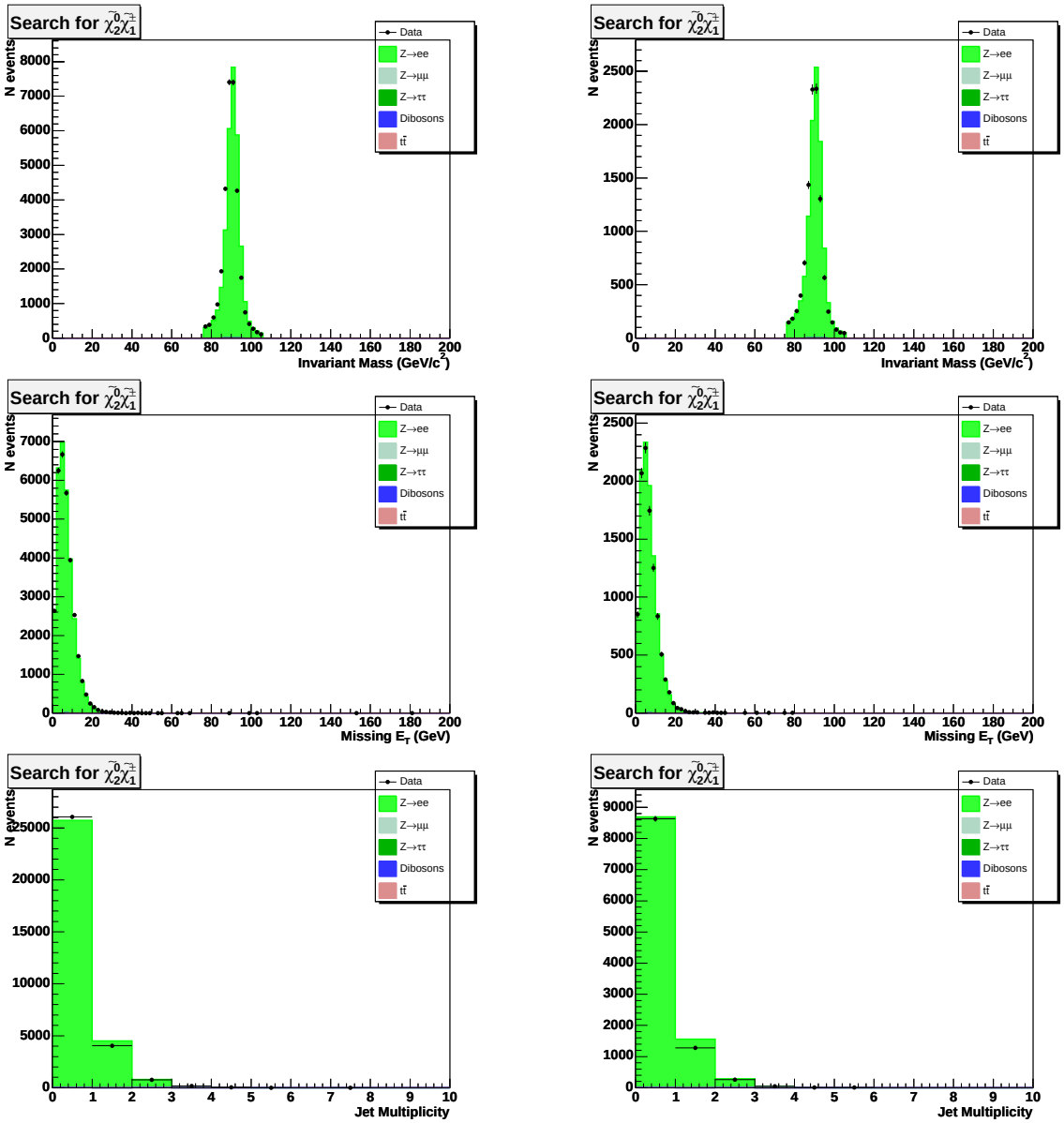

Figure 5.6: M_{os}, $\not{E}_{\mathrm{T}}$, and NJets distributions in control region Z with 2 tight electrons on left and 1 tight + 1 loose electron on right. Points are data and stacked histograms are background expectation.

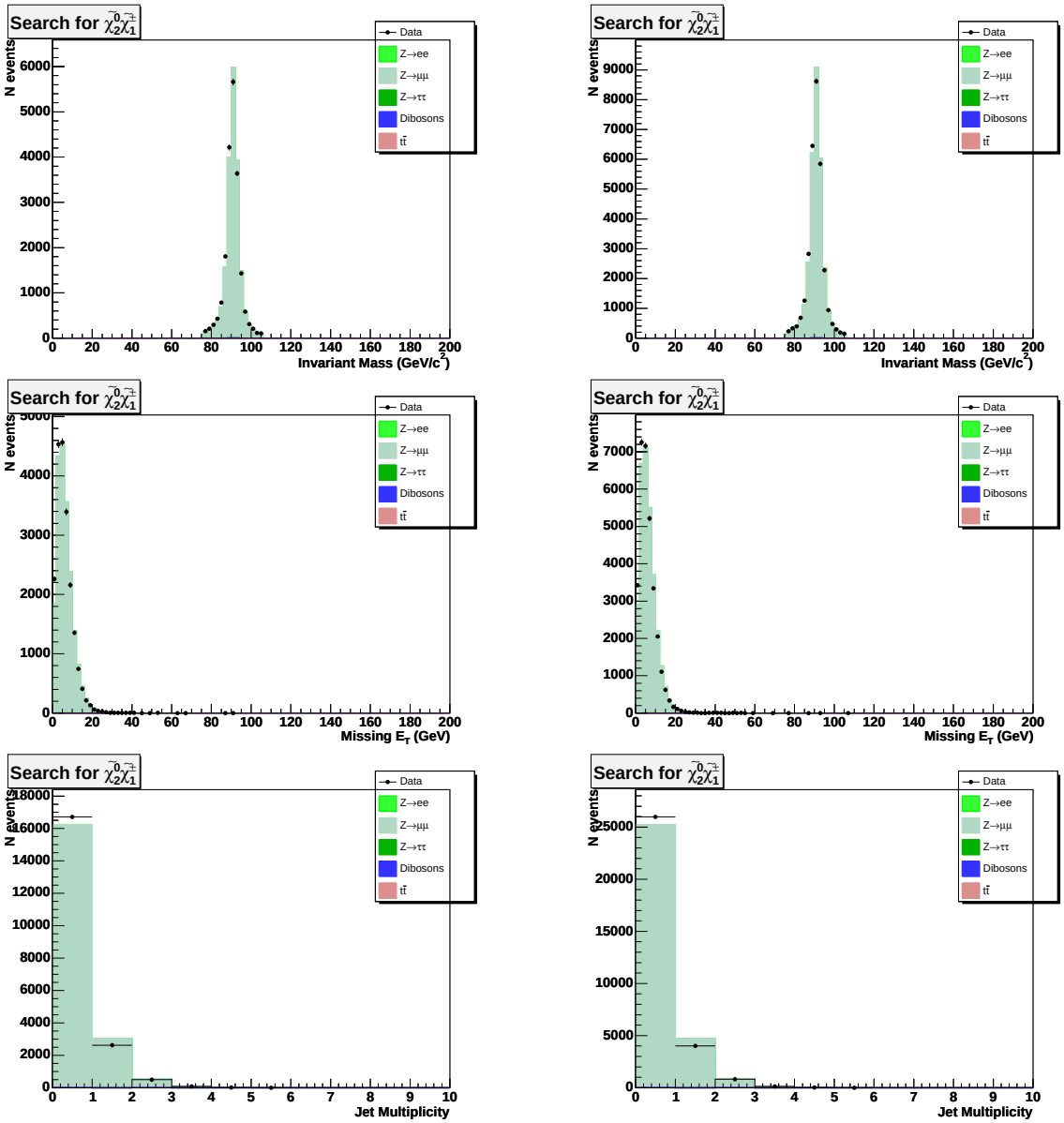

Figure 5.7: M_{os}, $\not{E}_{\mathrm{T}}$, and NJets distributions in control region Z with 2 tight muons on left and 1 tight + 1 loose muon on right. Points are data and stacked histograms are background expectation.

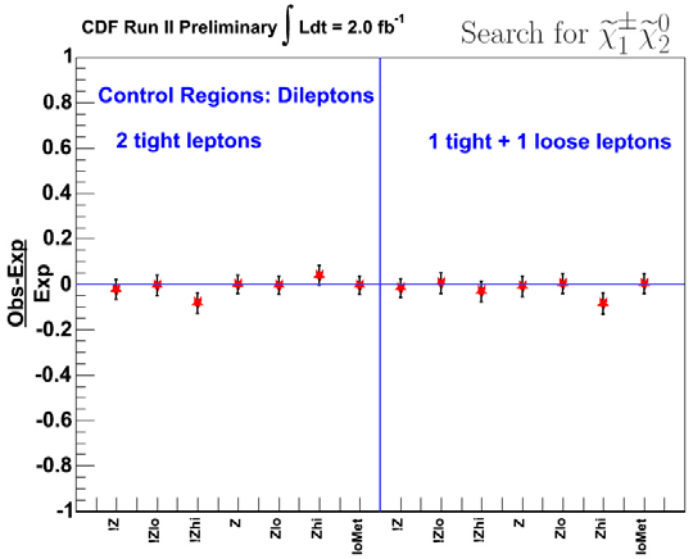

Figure 5.8: Figure shows the agreement in the dilepton control regions for the two channels and various control regions.

shown normalized to the expectation. The errors include those from statistics and partial systematics such as uncertainties in lepton identification efficiency, trigger efficiency and process cross-sections such as σ(Drell-Yan$\rightarrow ll$).

5.2 Trilepton Control Region

Now we move to studying the trilepton control regions. The trilepton control regions are defined in the same way as the dilepton ones. Figure 5.9 shows the schematic for the trilepton control regions. Since there are three leptons (or two leptons+track) in the final state, there are two opposite-charge combinations possible. Of the two opposite-charge lepton-lepton (or lepton-track) invariant masses, the higher is chosen to define the control region.

The region with a Z-veto, and high-$\not\!\!E_{\mathrm{T}}$ now constitutes the signal region. The other regions used as control regions are "Z" (split in to "Zhi", "Zlo") and the "!Zlo" regions. The control regions are split in to the different analysis channels (Table 4.1) to test the background estimation methods used for the different channels.

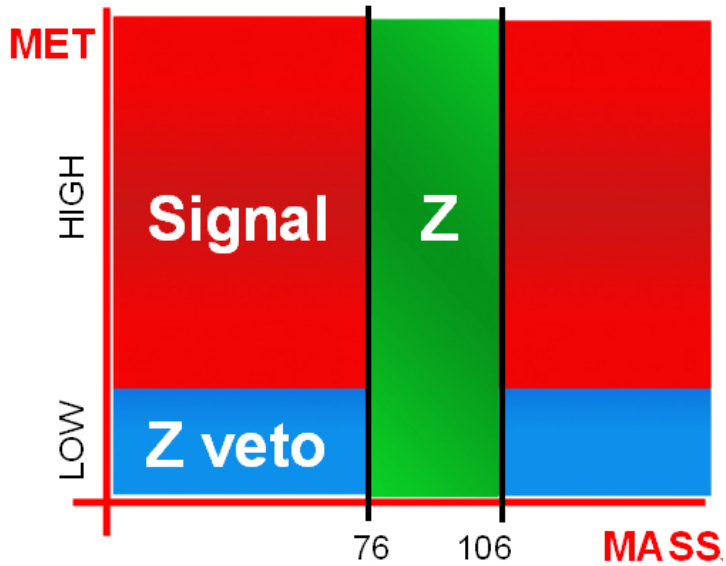

Figure 5.9: Figure illustrates the trilepton control regions. See text for details.

Table 5.3 shows the SM background expectations, and the observation in data for the various trilepton control regions for the channels with three leptons. Table 5.4 shows the control region results for the dilepton+track channels. Figure 5.10 shows a few kinematic distributions for the $l_t l_t l_t$ channel for the low-$\not{E}_{\mathrm{T}}$ control region (events with $\not{E}_{\mathrm{T}} < 10$ GeV). Figure 5.12 and 5.13 show kinematic distributions in the "Zhi" control regions for $l_t l_t T$ and $l_t l_l T$ channels respectively.

5.2.1 Summary of Control Region Studies

Overall, there is good agreement in the trilepton control regions. Even though the trilepton control regions suffer from lack of statistics, they are vital in testing the various background estimation methods, for the different channels. Figure 5.14 shows the agreement in the trilepton control regions. The uncertainties include statistical, as well some systematic contributions.

Figure 5.15 shows the pull distribution for 25 uncorrelated control regions. The distribution is fit with a gaussian and the fit parameters are indicated on the figure. A priori a unit gaussian centred at zero is expected, if the control region agreement is statistically

Name	$Z(ee)$	$Z(\mu\mu)$	$Z(\tau\tau)$	WW	WZ	ZZ	$t\bar{t}$	Fakes	Bkgd	Data
$l_t l_t l_t$										
lo	7.58	2.92	0.00	0.00	0.05	0.57	0.00	6.01	17.1±5.3	17
!Zlo	3.73	1.25	0.00	0.00	0.04	0.17	0.00	1.14	6.3±2.7	9
Z	4.67	2.17	0.00	0.01	1.30	0.82	0.02	7.68	16.7±5.7	9
Zlo	3.86	1.67	0.00	0.00	0.01	0.40	0.00	4.87	10.8±4.2	8
Zhi	0.00	0.09	0.00	0.01	1.23	0.30	0.02	1.06	2.7±1.7	0
$l_t l_t l_l$										
lo	0.74	3.38	0.00	0.00	0.04	0.31	0.00	2.57	7.0±3.0	9
!Zlo	0.64	1.09	0.00	0.00	0.02	0.10	0.00	0.33	2.2±1.5	3
Z	0.10	2.69	0.00	0.00	1.09	0.64	0.01	3.13	7.7±3.2	8
Zlo	0.10	2.29	0.00	0.00	0.02	0.21	0.00	2.24	4.9±2.5	6
Zhi	0.00	0.08	0.00	0.00	1.05	0.34	0.01	0.28	1.8±1.3	2
$l_t l_l l_l$										
lo	0.57	1.81	0.00	0.00	0.03	0.19	0.00	1.68	4.3±2.3	3
!Zlo	0.12	0.96	0.00	0.00	0.00	0.07	0.00	0.29	1.4±1.3	0
Z	0.64	1.09	0.00	0.00	0.70	0.32	0.02	2.63	5.4±2.7	6
Zlo	0.45	0.84	0.00	0.00	0.03	0.12	0.00	1.39	2.8±1.9	3
Zhi	0.19	0.09	0.00	0.00	0.62	0.14	0.02	0.57	1.6±1.3	2

Table 5.3: Table shows the control region numbers for all trilepton control regions for the channels with three leptons.

Name	$Z(ee)$	$Z(\mu\mu)$	$Z(\tau\tau)$	WW	WZ	ZZ	$t\bar{t}$	Fakes	Bkgd	Data
$l_t l_t T$										
lo	168.37	138.84	1.73	0.02	0.02	0.35	0.02	2.39	312±35	290
!Zlo	49.31	35.84	1.61	0.01	0.01	0.10	0.00	1.57	88±13	72
Z	166.42	140.97	0.12	0.13	0.32	0.77	0.29	1.82	311±34	299
Zlo	119.06	103.00	0.12	0.01	0.01	0.25	0.02	0.83	223±26	218
Zhi	14.67	10.40	0.00	0.09	0.30	0.41	0.27	0.67	27±6	34
$l_t l_l T$										
lo	55.02	170.96	0.74	0.01	0.01	0.24	0.05	1.37	228±30	214
!Zlo	6.64	25.38	0.74	0.00	0.00	0.08	0.03	0.90	34±7	31
Z	69.45	202.01	0.15	0.11	0.27	0.56	0.30	1.13	274±35	246
Zlo	48.38	145.58	0.00	0.01	0.00	0.15	0.02	0.47	195±26	183
Zhi	8.59	17.69	0.00	0.10	0.27	0.32	0.28	0.48	28±6	23

Table 5.4: Table shows the control region numbers for all control regions for dilepton+track channels. Fake event contributions for the dilepton+track channels are included in the other predictions (see section 4.4.2).

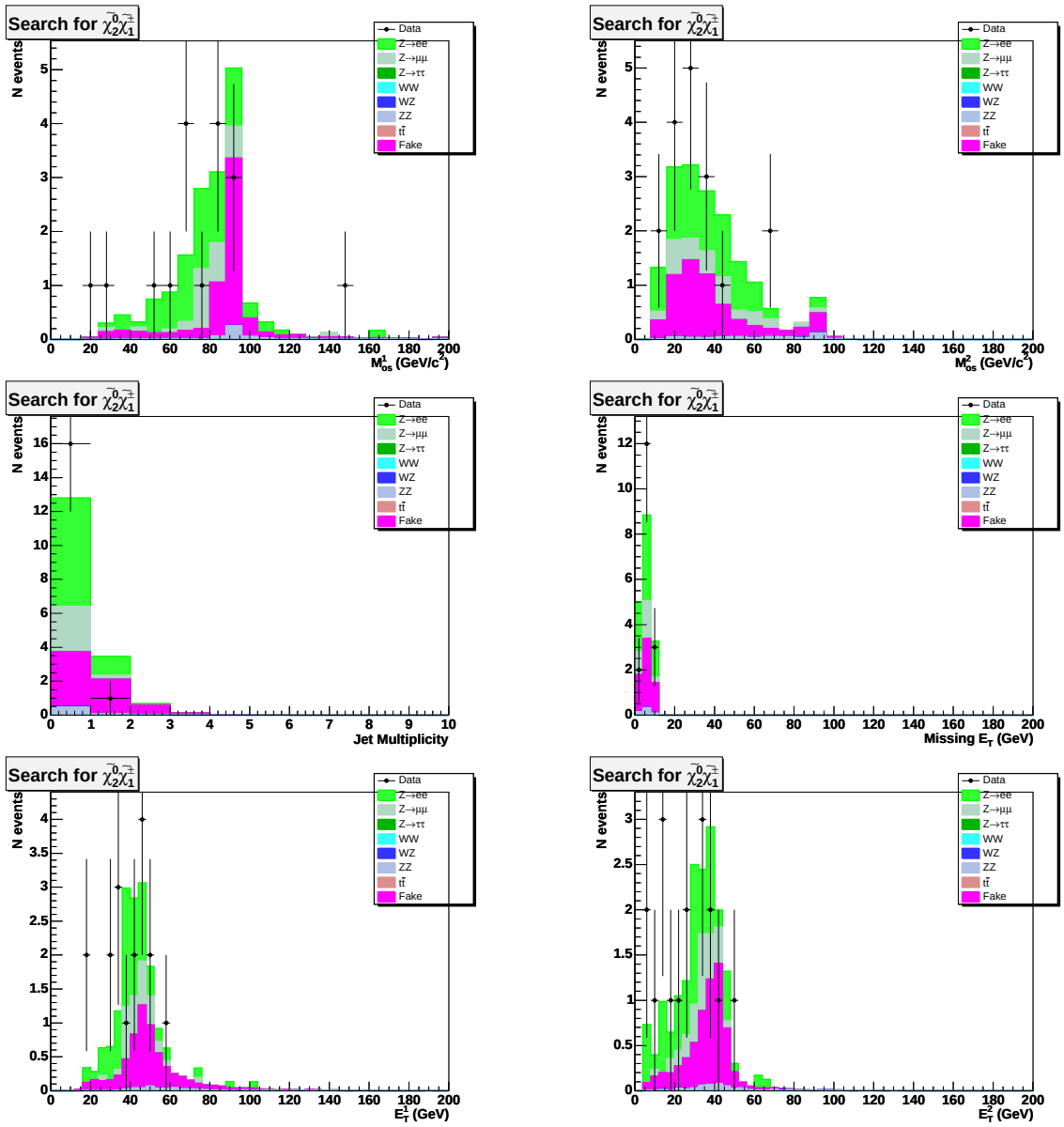

Figure 5.10: M_{os}^1, M_{os}^2, NJets, $\not\!\!E_{\mathrm{T}}$, leading, and next-to-leading lepton E_{T} distributions in control region $\not\!\!E_{\mathrm{T}} < 10$ GeV for the $l_t l_t l_t$ channel. Points are data and stacked histograms are background expectation.

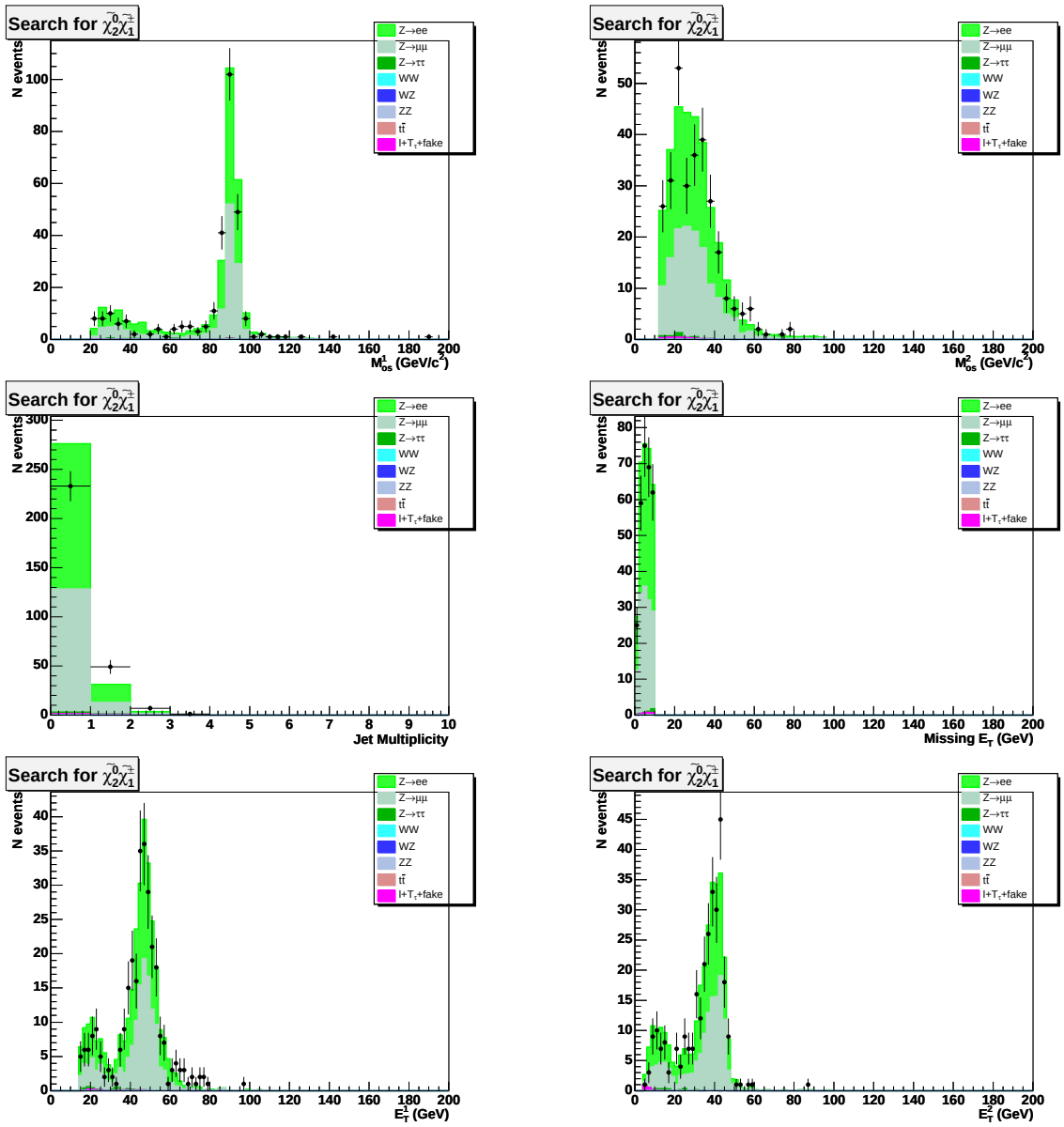

Figure 5.11: M^1_{os}, M^2_{os}, NJets, $\not{E}_{\mathrm{T}}$, leading, and next-to-leading lepton E_{T} distributions in control region $\not{E}_{\mathrm{T}} < 10$ GeV for $l_t l_t T$ channel. Points are data and stacked histograms are background expectation.

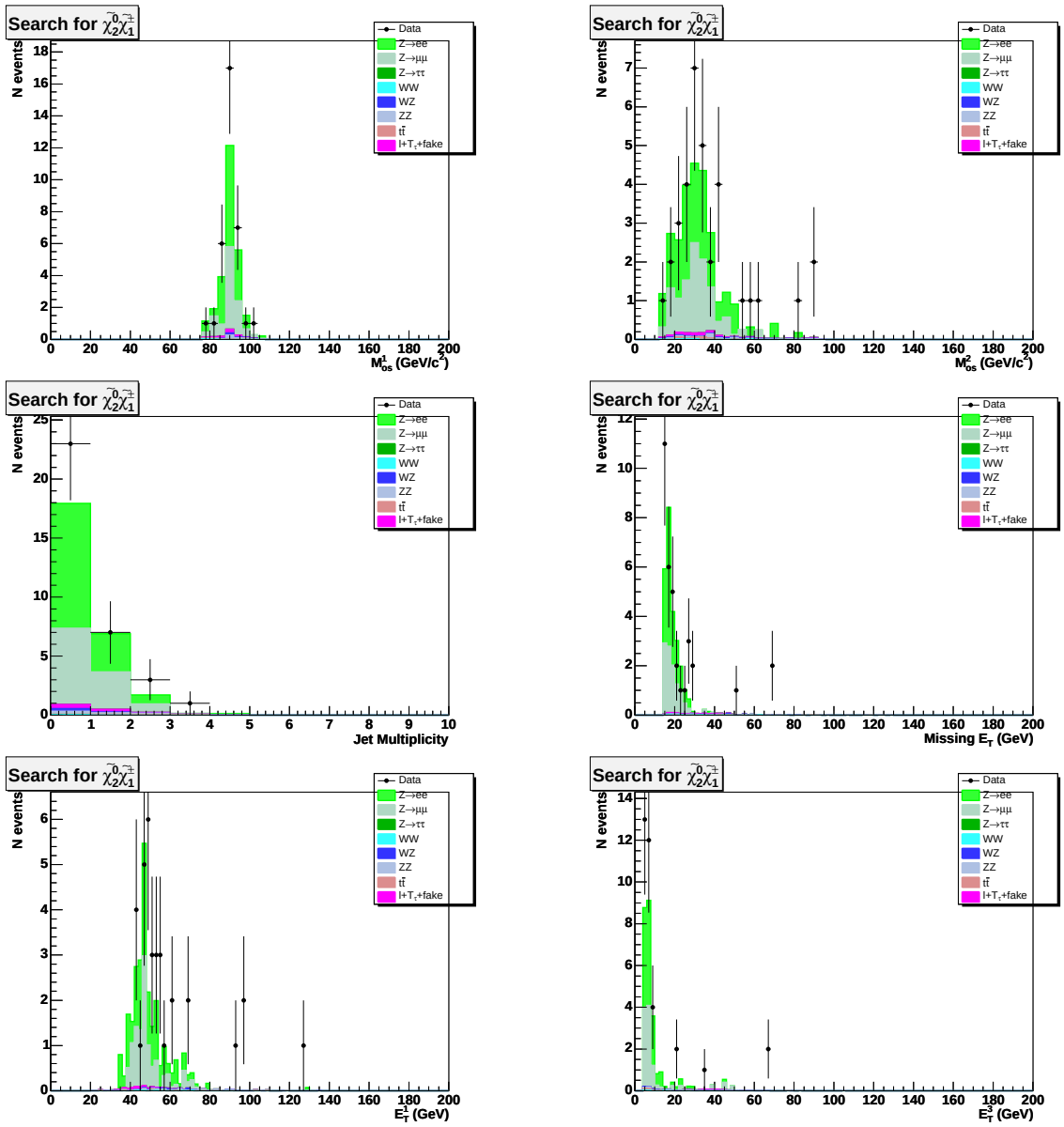

Figure 5.12: M_{os}^1, M_{os}^2, NJets, $\not{E}_{\mathrm{T}}$, leading, and trailing lepton E_{T} distributions in control region Zhi for $l_t l_t T$ channel. Points are data and stacked histograms are background expectation.

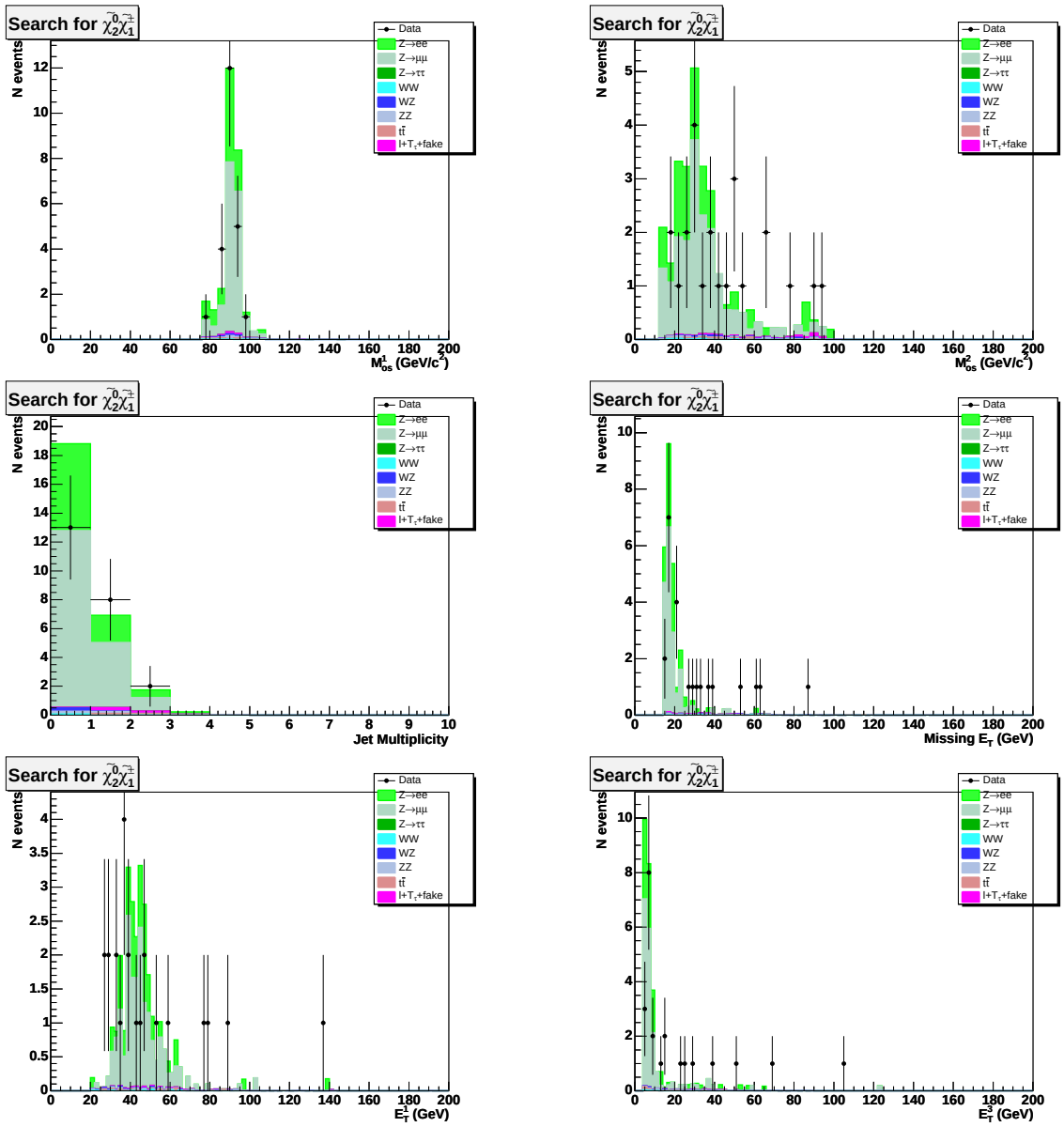

Figure 5.13: M^1_{os}, M^2_{os}, NJets, $\not{E}_{\rm T}$, leading, and trailing lepton $E_{\rm T}$ distributions in control region Zhi for $l_t l_l T$ channel. Points are data and stacked histograms are background expectation.

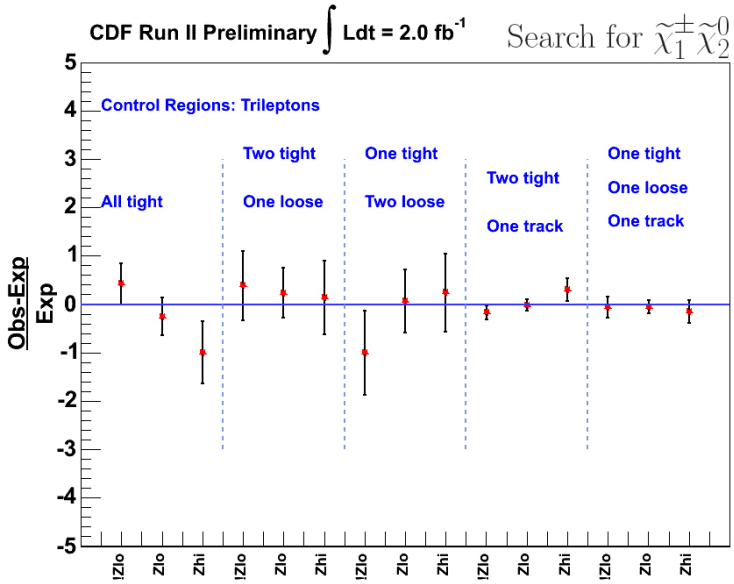

Figure 5.14: Figure shows the agreement in the trilepton control regions for the five analysis channels and various control regions.

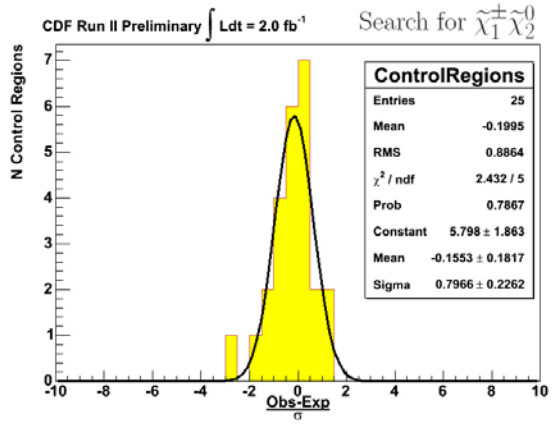

Figure 5.15: Figure shows the pull distribution, i.e difference between observation and expectation in units of one standard deviation, for the 25 uncorrelated control regions (dilepton, trilepton, and dilepton+track).

consistent, and the uncertainties are estimated correctly. From the fit parameters, we see that the mean and standard deviation is indeed consistent with a unit gaussian. This gives confidence in our predictive ability of SM backgrounds.

Chapter 6

Final Event Selection

We have seen in the last chapter that the background predictions have been tested and verified in multiple control regions. In this chapter we shall now discuss the final selections optimized to minimize background without significant loss of signal. In Section 6.3, the final predictions for backgrounds and for the nominal signal point are presented, with a discussion on systematic uncertainties in Section 6.2.

6.1 Final Selections

The final selections are designed to minimize the background predictions, and thus enriching the signal contribution. The optimization is done based on signal/$\sqrt{\text{background}}$ and in an "all-but-one"[1] fashion. However, care is taken against over-optimizing. The parameter space for signal is large and thus the signal characteristics can vary significantly. The selections are designed to maintain sensitivity to signal for as much of parameter space as possible.

Figure 6.1 shows the $\not{E}_{\mathrm{T}}$ distribution for the $l_t l_t l_t$ and $l_t l_t T$ channels after all other selections are made. Figure 6.2 shows the highest opposite-charge invariant mass distribution for the $l_t l_t T$ channel. Figure 6.3 shows the SumE_{T} and NJets distribution for the $l_t l_t l_t$ channel. Figure 6.4 shows the $\Delta\phi_{os}$ distribution, i.e the maximum of the two azimuthal angle distributions of the opposite-charge lepton-lepton (lepton-track) pairs, for the $l_t l_t T$ channel.

[1]Each selection is chosen based on the distribution of that variable after all other selections have been made.

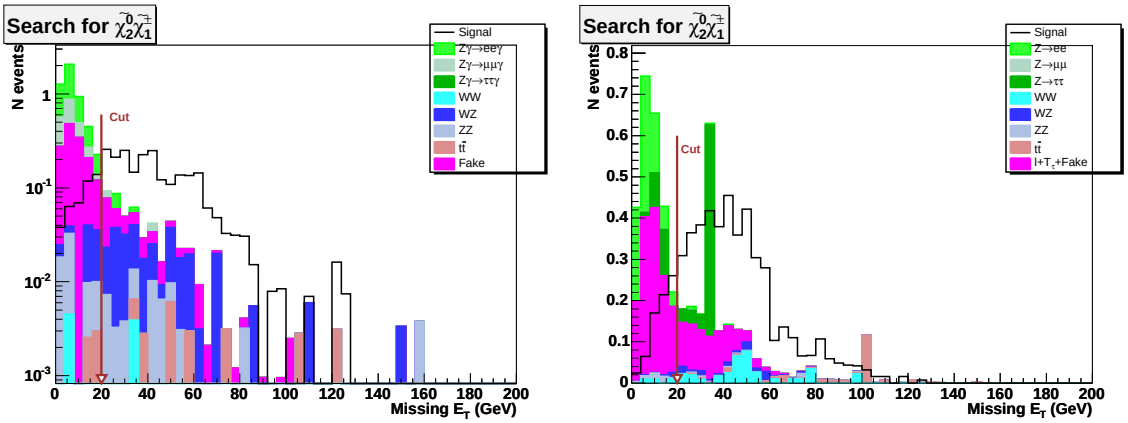

Figure 6.1: Signal and background $\not\!\!E_{\mathrm{T}}$ distributions for $l_t l_t l_t$ channel on left and $l_t l_t T$ on right. Background histograms are stacked. Signal distribution is shown in black open histogram. All samples are normalized to the data luminosity. Events with $\not\!\!E_{\mathrm{T}} > 20$ GeV are selected. All other selections have been applied.

Variable	Trilepton	Dilepton+Track
$\not\!\!E_{\mathrm{T}}$	> 20 GeV	> 20 GeV
$\Delta\phi_{os}$	< 2.9 rad	< 2.8 rad
max OS Mass	Z veto	Z veto
next OS Mass	Z veto	Z veto
SumE_{T}	< 80 GeV	< 80 GeV
Njets	< 2	< 2

Table 6.1: Final selection cuts. Description for each cut can be found in text.

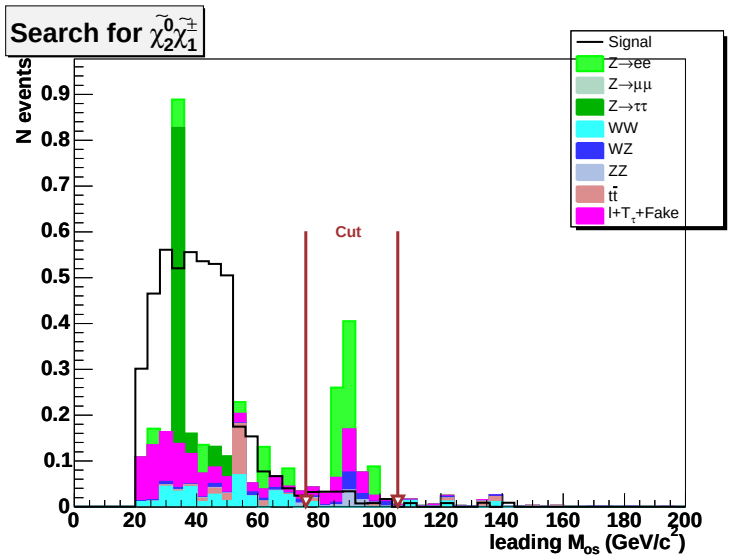

Figure 6.2: Signal and background maximum opposite sign mass distribution for ttT channel. Background histograms are stacked. Signal distribution is shown in black open histogram. All samples are normalized to the data luminosity. Events with mass in the Z-mass window, viz. 76 to 106 GeV/c^2 are rejected. All other selections have been applied.

The final selections are chosen based on specific characteristics of background processes. The selections listed in Table 6.1 are :

- $\not{E}_{\mathrm{T}} \geq 20$ GeV : The $\not{E}_{\mathrm{T}}$ in the event is required to be above 20 GeV. This cut reduces the Drell-Yan and ZZ background, which has intrinsically low $\not{E}_{\mathrm{T}}$.

- $\Delta\phi_{os} \leq 2.9(2.8)$ rad : In addition to $\not{E}_{\mathrm{T}}$, the Drell-Yan background is further reduced by requiring that any opposite charged lepton-lepton (or lepton-track) pairs are not back-to-back by making a cut on the azimuthal separation between the two leptons. The cut is tightened from 2.9 to 2.8 for the dilepton+track channels since the Drell-Yan background is larger for those channels.

- Vetoes on Z mass : To remove potential Z events, the event is vetoed if any of the opposite charged lepton-lepton (or lepton-track) pairs forms a mass in the Z window ($76 \leq \frac{M_{ll}}{\mathrm{GeV}/c^2} \leq 106$).

- Sum$E_{\mathrm{T}} \leq 80$ GeV : The total sum of E_{T} of all jets ($E_{\mathrm{T}}^{corr} \geq 15$ GeV) in the event is required to be less than 80 GeV. This is done to reduce the $t\bar{t}$ and fake lepton

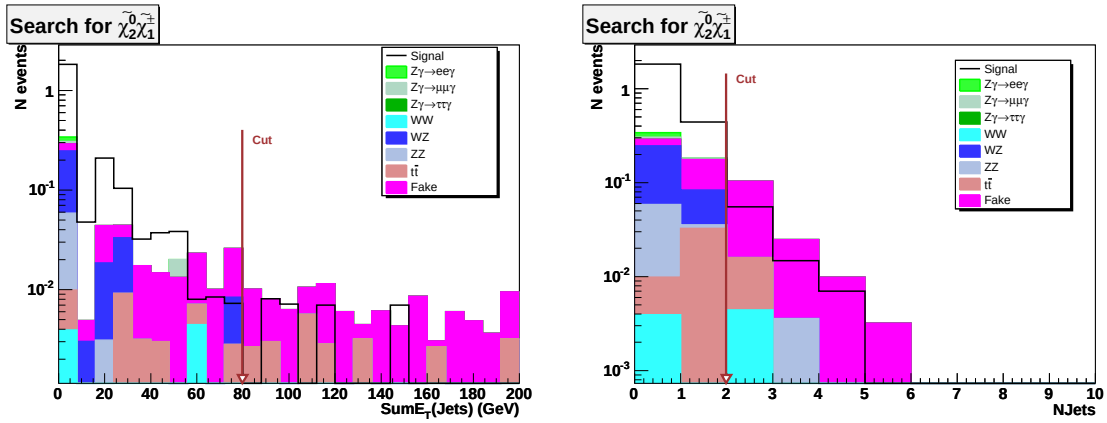

Figure 6.3: Signal and background SumE_T of jets distribution on left and number of Jets on right for $l_t l_t l_t$ channel. Background histograms are stacked. Signal distribution is shown in black open histogram. All samples are normalized to the data luminosity. Events are selected with SumE_T < 80 GeV and Njets < 2. All other selections except SumE_T and Njets are applied.

background. Moreover, the signal topology has no hard jets.

- NJets < 2 : Events are vetoed if there is more than one jet ($E_{\mathrm{T}}^{corr} \geq 15$ GeV). This requirement along with the SumE_{T} requirement will remove any background from $t\bar{t}$ and residual QCD background.

Table 6.2 shows the predictions for various SM backgrounds for the five analysis channels; Figure 6.5 shows the breakdown of the standard model contributions in the trilepton channels (left) and dilepton+track channels (right)

	$Z(ee)$	$Z(\mu\mu)$	$Z(\tau\tau)$	WW	WZ	ZZ	$t\bar{t}$	Fake	Sum of Bkgd
$l_t l_t l_t$	0.03	0.02	0.00	0.00	0.24	0.05	0.02	0.12	0.49
$l_t l_t l_l$	0.00	0.01	0.00	0.00	0.13	0.07	0.01	0.04	0.25
$l_t l_l l_l$	0.00	0.00	0.00	0.00	0.06	0.02	0.03	0.03	0.14
$l_t l_t T$	0.81	0.00	0.82	0.38	0.15	0.08	0.22	0.75	3.22
$l_t l_l T$	0.73	0.30	0.29	0.29	0.05	0.04	0.18	0.41	2.28

Table 6.2: Number of expected signal and background events in 2 fb^{-1}of data. The fake numbers for trilepton channels are for 2 leptons + a fake lepton. For the dilepton+track channels the fake numbers are for 1 lepton + 1 track + fake lepton.

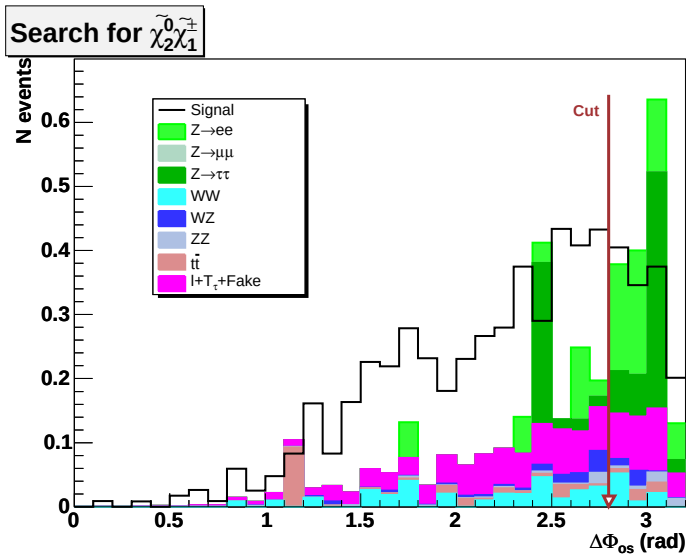

Figure 6.4: Signal and background $\Delta\phi_{os}$ distribution for $l_t l_t T$. The larger of the two opposite-charge pair $\Delta\phi$'s is plotted. Background histograms are stacked. Signal distribution is shown in black open histogram. All samples are normalized to the data luminosity. Events are required to have $\Delta\phi_{12} < 2.8$ rad. For the plot, all cuts listed in Table 6.1 except $\Delta\phi_{os}$ are applied.

	ID	Trig	JES	σ	PDF	ISR/FSR	Conv	ITR(nom)	ITR(alt)	Fake
$l_t l_t l_t$	2.3	0.3	1.5	5.0	1.4	2.3	2.2	-	-	12.2
$l_t l_t l_l$	2.5	0.3	1.7	5.9	1.6	2.5	2.1	-	-	8
$l_t l_l l_l$	2.2	0.3	3.5	5.0	1.3	2.2	1.8	-	-	10.7
$l_t l_t T$	1.8	0.2	3.9	2.3	1.5	1.8	-	5.8	6.0	11.6
$l_t l_l T$	1.8	0.2	5.2	2.4	1.5	1.8	-	8.6	10.5	9.0
Signal	4	0.5	0.5	10	2	4	-	-	-	-

Table 6.3: The systematic errors for the different channels broken down by source in percentage. A universal 6% uncertainty on the luminosity is not included in this table.

6.2 Systematic Uncertainties

The significant systematic uncertainties for this analysis are listed in Table 6.3, in terms of their effect on the final background prediction. A discussion of the sources of systematic uncertainty follows :

- ID : The errors on the lepton identification scalefactors are a source of uncertainty. They are listed in Section 3.5. These errors are estimated during the scalefactor measurements and include the statistical uncertainty on the scalefactor measurement as well.

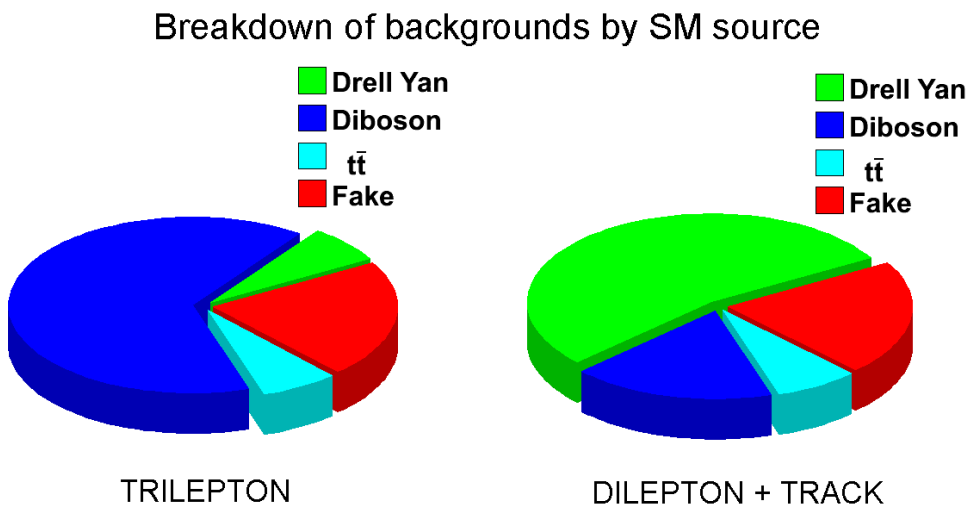

Figure 6.5: The pie charts show the breakdown of the SM background by source in the trilepton channels (left) and the dilepton+track channels (right).

- Trig : The errors on the trigger efficiencies of the various paths are listed in Appendix A and are based on the respective measurements of trigger efficiency.

- JES : For the jet energy scale (JES) uncertainty, the jet energies are fluctuated by one standard deviation up and down and the difference of signal and background acceptance from the nominal acceptance is evaluated. The difference in acceptance is taken as a systematic uncertainty. In some cases, the statistics after all final selections precludes such an estimation. In these cases, the difference from nominal acceptance for a 'signal' like selection[2] is evaluated and taken as a systematic uncertainty.

- Process cross-section (σ) : The error on the cross section of the background process is propogated through to the final background predictions. The errors quoted by the CDF WZ search [45] are used for dibosons, and the top mass measurement [46] is used for the $t\bar{t}$ cross section.

- PDF : For the PDF uncertainties as well, the numbers quoted by the CDF WZ search, and the top-quark mass measurement are used.

[2]viz. two leptons with $\not\!\!E_{\rm T}$ >20 GeV, Sum$E_{\rm T}$ (Jets)<80 GeV, Njets<2, $\Delta\phi_{os} < 2.9$ radians

- ISR/FSR : The effects of turning on the initial state (ISR) and final state (FSR) radiation on the final signal and background acceptance are studied using dedicated MC samples, and the difference from the nominal acceptance is taken as a source of systematic uncertainty.

- Conv. : The systematic error on the conversion scale factor is taken from the measurement of the scalefactor.This is applied to the backgrounds for the trilepton channels, when the third lepton is expected to have come from a photon conversion such as $Z\gamma \rightarrow ee\gamma$.

- ITR(nominal) : This systematic is applied to the dilepton+track channels. It is the error on the isolated track rate measurement as described in section 4.4.2.

- ITR(alternate) : An alternate parametrization is also used for the isolated track rate. The track rate is parametrized as a function of the SumE_{T} of all jets ($E_{\mathrm{T}}{}^{corr} > 10$) in the event. The difference of background estimate from the nominal estimate is taken as the systematic uncertainty.

- Fake : This is the error on the rate of jet faking a lepton measurement (see Section 4.4.2) which is taken to be 50%. This gives a 50% uncertainty on the fake lepton background estimate.

A systematic check for the $\not\!\!E_{\mathrm{T}}$ correction for tracks in each event is also done. For the tracks, no assumption is made about the type of charged particle giving the track. The $\not\!\!E_{\mathrm{T}}$ for the track is corrected if the $E/p \leq 1$ for the track. The energy deposit E associated with the track is used for this. To test if this selection has any systematic effect, this selection is changed to $E/p \leq 0.8$ and the deviation from nominal is checked. Since there is no significant deviation from the nominal prediction, the $\not\!\!E_{\mathrm{T}}$ correction for isolated tracks is not a source of systematic uncertainty.

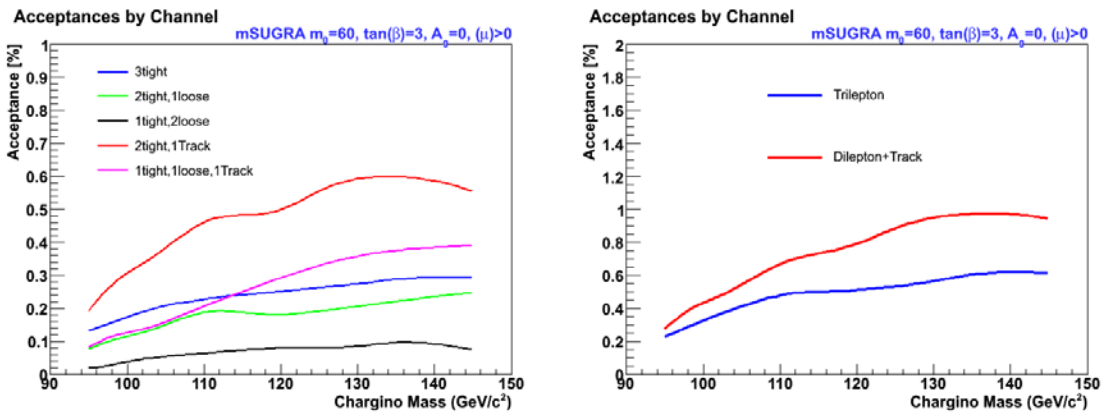

Figure 6.6: Signal acceptance by channel.

6.3 Background and Signal Predictions

Table 6.4 shows the final background predictions for the five analysis channels, along with the signal expectation for the nominal mSUGRA point[3] for an integrated luminosity of 2 fb^{-1}. For easy reference, the sum of the trilepton, and dilepton+track channels is also shown, although these sums are not used anywhere. Figure 6.6 shows the signal acceptance in each channel as a function of the chargino mass.

Channel	Background	Signal
$l_t l_t l_t$	0.49 ± 0.04(stat) ± 0.07(syst)	2.25 ± 0.13(stat) ± 0.26(syst)
$l_t l_t l_l$	0.25 ± 0.03(stat) ± 0.03(syst)	1.61 ± 0.11(stat) ± 0.19(syst)
$l_t l_l l_l$	0.14 ± 0.02(stat) ± 0.02(syst)	0.68 ± 0.07(stat) ± 0.08(syst)
Trilepton	0.88 ± 0.05(stat) ± 0.08(syst)	4.5 ± 0.2(stat) ± 0.3(syst)
$l_t l_t T$	3.22 ± 0.48(stat) ± 0.49(syst)	4.44 ± 0.19(stat) ± 0.52(syst)
$l_t l_l T$	2.28 ± 0.47(stat) ± 0.40(syst)	2.42 ± 0.14(stat) ± 0.28(syst)
Dilepton+Track	5.5 ± 0.7(stat) ± 0.6(syst)	6.9 ± 0.2(stat) ± 0.6(syst)

Table 6.4: Number of expected signal and background events and number of observed events for 2 fb^{-1} of data. Uncertainties are statistical (stat) and full systematics (syst).

[3] $m_0 = 60$ GeV/c^2, $m_{1/2} = 190$ GeV/c^2, $\tan\beta = 3$, $A_0 = 0$, $\mu > 0$.

Chapter 7

Results

In the last chapter we have discussed the final optmized analysis selections, and seen the final predictions of expected number of events from SM background sources, and from the signal for a sample mSUGRA point. In this chapter, we shall see the final results of this analysis. After discussing the observation in data, we shall then cover the interpretation of these results in terms of the mSUGRA model. Finally, we shall address the issue of presenting the results such that they are independent of the model considered.

7.1 Observation in Data

Channel	Background	Signal	Observed
$l_t l_t l_t$	0.49 ± 0.04 ± 0.07	2.25 ± 0.13 ± 0.26	1
$l_t l_t l_l$	0.25 ± 0.03 ± 0.03	1.61 ± 0.11 ± 0.19	0
$l_t l_l l_l$	0.14 ± 0.02 ± 0.02	0.68 ± 0.07 ± 0.08	0
Trilepton	0.88 ± 0.05 ± 0.08	4.5 ± 0.2 ± 0.3	1
$l_t l_t T$	3.22 ± 0.48 ± 0.49	4.44 ± 0.19 ± 0.52	4
$l_t l_l T$	2.28 ± 0.47 ± 0.40	2.42 ± 0.14 ± 0.28	2
Dilepton+Track	5.5 ± 0.7 ± 0.6	6.9 ± 0.2 ± 0.6	6

Table 7.1: Number of expected signal and background events and number of observed events for 2 fb^{-1} of data. Uncertainties are statistical first and then the full systematic.

Table 7.1 shows the observation of events in data for each of the independent channels. The trilepton channels have one event, in the $l_t l_t l_t$ channel. The dilepton+track channels have six events, 4 in the $l_t l_t T$ channel, and 2 in the $l_t l_l T$ channel. As seen from the table, the observations are completely consistent with the standard model predictions. No excesses are seen in the event counts.

Figures 7.1, 7.2, 7.3 show some distributions of final selections (Table 6.1) along with the observed events for the $l_t l_t l_t$, $l_t l_t T$, and $l_t l_l T$ channels respectively. The figures show that the distribution of the observed events agrees with the background predictions, and no unusual behavior is seen. In Table 7.2, some properties of the observed events are summarized.

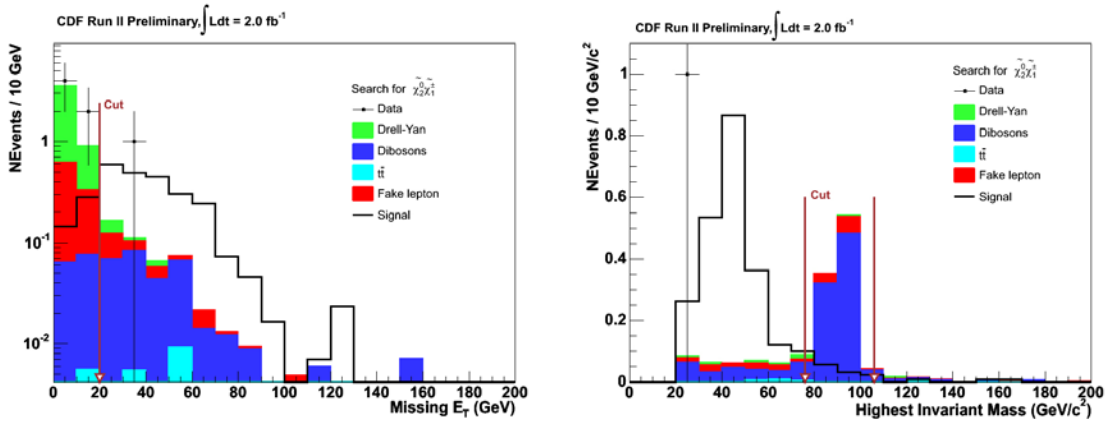

Figure 7.1: Signal and background $\not\!\!E_{\mathrm{T}}$ distribution on left and highest invariant mass (M_{os}^1) on right for $l_t l_t l_t$ channel. Background histograms are stacked. Signal distribution is shown in black open histogram. All samples are normalized to the data luminosity. We select events with $\not\!\!E_{\mathrm{T}} > 20$ GeV and outside the Z-window ($76 < M_{os}/\mathrm{GeV}/c^2 < 106$). Observed data events are shown as black points.

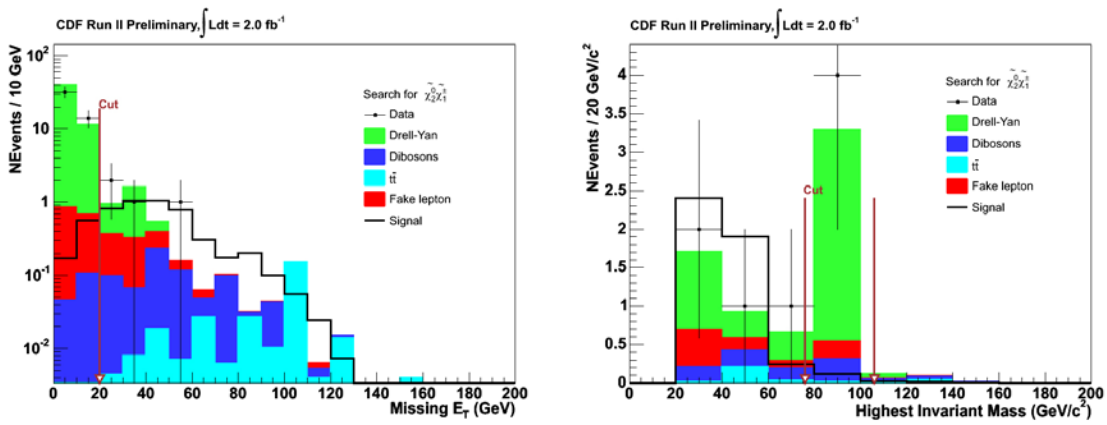

Figure 7.2: Signal and background $\not\!\!E_{\mathrm{T}}$ distribution on left and highest invariant mass (M_{os}^1) on right for $l_t l_t T$ channel. Background histograms are stacked. Signal distribution is shown in black open histogram. All samples are normalized to the data luminosity. We select events with $\not\!\!E_{\mathrm{T}} > 20$ GeV and outside the Z-window ($76 < M_{os}/\mathrm{GeV}/c^2 < 106$). Observed data events are shown as black points.

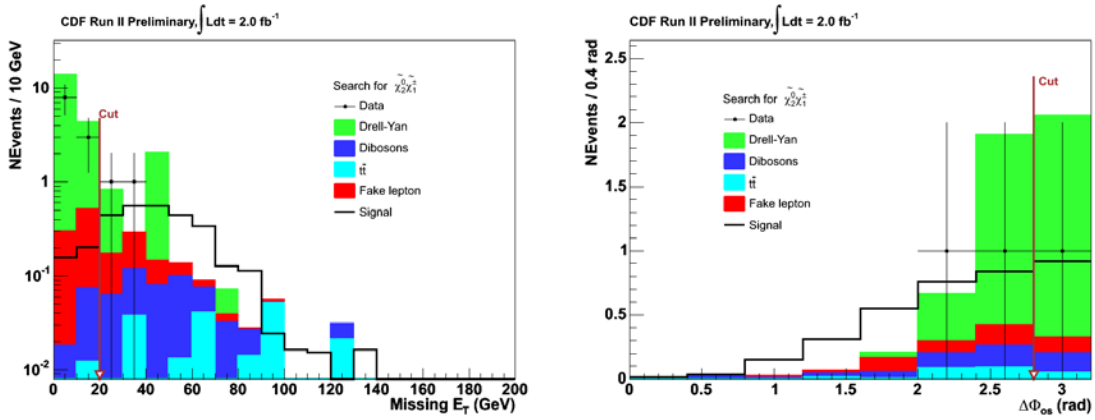

Figure 7.3: Signal and background $\not\!\!E_{\mathrm{T}}$ distribution on left and $\Delta\phi_{os}$ on right for $l_t l_l T$ channel. Background histograms are stacked. Signal distribution is shown in black open histogram. All samples are normalized to the data luminosity. We select events with $\not\!\!E_{\mathrm{T}} > 20$ GeV and with $\Delta\phi_{os} < 2.8$ rad. Observed data events are shown as black points.

Channel	Type	E_{T}^1	E_{T}^2	E_{T}^3	M_{os}^1	M_{os}^2	$\not\!\!E_{\mathrm{T}}$	Jet$^1 E_{\mathrm{T}}$
$l_t l_t l_t$	-TE +TE -TE	23.6	17.2	5.8	29.1	15.5	37.2	59.4
$l_t l_t T$	-TE +TE -IT	26.9	9.7	8.5	41.4	18.8	27.6	23.6
$l_t l_t T$	-TE -TE +IT	22.8	9.3	55.9	70.3	46.2	57.8	17.7
$l_t l_t T$	+UP -X -IT	33.7	6.2	9.2	32.9	28.3	20.4	21.4
$l_t l_t T$	-UP +X -IT	44.7	21.1	7.8	29.2	25.8	38.9	41.1
$l_t l_l T$	+UP -IO +IT	22.8	12.2	6.5	39.2	17.8	28.5	33.6
$l_t l_l T$	+UP -IO -IT	58.6	69.9	44.1	124.0	57.5	36.8	—-

Table 7.2: Table shows some characteristics of the events observed in data. The key is as follows: TE = tight electron; UP,X = CMUP, CMX = tight muon; IO = loose muon; IT = isolated track; +/- = charge of leptons. In case of muons and tracks, E_{T} is the p_{T} of the object.

7.2 Calculating Limits

The observation of events is consistent with the standard model predictions; this leads naturally to the question of how specific models can be constrained using these results. The standard approach is followed here. The predictions and observations are used to set limits on the cross-section×branching ratio ($\sigma\times$BR) of $p\bar{p} \rightarrow \widetilde{\chi}_1^{\pm}\widetilde{\chi}_2^0 \rightarrow 3l$. These limits can be then interpreted to exclude $\widetilde{\chi}_1^{\pm}$'s (or $\widetilde{\chi}_2^0$'s) below a specific mass.

The analysis has five exclusive channels. These channels are treated as five independent experiments and are combined using the "CL$_s$" method [47, 48] to calculate the limits on $\sigma\times$BR. A brief discussion of this method following Ref. [47] closely is given here.

7.2.1 CL_s method

The CL_s method is useful to combine independent searches with small statistics. This helps in improving the sensitivity significantly. The idea is to treat the search results as statistically independent bins and compute the combined exclusion confidence levels. Consider as a test statistic X which discriminates between signal-like and background-like outcomes, the likelihood ratio :

$$X = \prod_{i=1}^{n} \frac{e^{-(s_i+b_i)}(s_i+b_i)^{d_i}}{e^{-b_i} b_i^{d_i}} \tag{7.1}$$

where the estimated signal in the ith channel is s_i, the estimated background is b_i, and the number of observed candidates id d_i. The confidence level for excluding the $s+b$ hypothesis, i.e. the probability that the test statistic would be less than or equal to that observed in data, assuming signal and background at the hypothesized levels, is

$$\mathrm{CL}_{s+b} = P_{s+b}(X \leq X_{obs}) = \sum_{X(d_i^{'}) \leq X(d_i)} \prod_{i=1}^{n} \frac{e^{-(s_i+b_i)}(s_i+b_i)^{d_i^{'}}}{d_i^{'}!} \tag{7.2}$$

where $X(d_i)$ is the test statistic computed for observed events in each channel d_i, and the sum runs over all possible outcomes $d_i^{'}$ with test statistics less than or equal to the observed one. The confidence level $(1 - \mathrm{CL}_{s+b})$ is used to quote the exclusion limits. The sum in Eq. 7.2 is carried out by computing the probability distribution function (PDF) for the test statistic for a set of channels and convoluting with the PDF's of the test statistic of additional channels.

7.3 mSUGRA interpretation

There are various supersymmetric models that may be used as guidelines for an analysis to search for signs of supersymmetry (SUSY). The analysis presented here searched for the trilepton signature of the associated production of the $\widetilde{\chi}_1^{\pm}$ and $\widetilde{\chi}_2^0$. The task of interpreting the results within the vast suspersymmetric parameter space can be significantly simplified by working within the constrained MSSM or mSUGRA. mSUGRA (as described in

Section 2.3.1) is characterized by four parameters and one sign :

$$m_0,\ m_{1/2},\ A_0,\ \tan\beta,\ \mathrm{sign}(\mu)$$

In this study we focus on the two parameters which give the most dramatic changes in the event kinematics and event topology - m_0, and $m_{1/2}$. The other mSUGRA parameters are fixed as $\tan\beta = 3,\ A_0 = 0,\ \mu > 0$. Variation of $\tan(\beta)$ leads to a variation of $\widetilde{\tau}_1$ mass, leading to changing number of τ's in the final state. At higher values of $\tan(\beta)$, the decays of the $\widetilde{\chi}_1^{\pm}$ and $\widetilde{\chi}_2^0$ are dominated by τ's. Since this trilepton analysis allows only one 'lepton' from the hadronic decays of τ's[1], $\tan\beta$ is set to a low value to reduce the fraction of τ's in the final state. However, as described in Section 7.4, the dependence of final cross-section limits can be characterized by examining the τ content of the final state. The dependence of limits on $\tan\beta$ can be extracted by studying the break-down of limits by τ content of the final state.

7.3.1 Important mSUGRA features recap

It is worth refreshing some of the phenomenological details of the mSUGRA model. As described in Section 2.3.1, the mass of the $\widetilde{\chi}_1^{\pm}$ and $\widetilde{\chi}_2^0$ is nearly equal; the $\widetilde{\chi}_2^0$ is slightly more massive than the $\widetilde{\chi}_1^{\pm}$. The right-handed sleptons $\tilde{l}_R^{\pm}$ are lighter than the left-handed sleptons $\tilde{l}_L^{\pm}$. Among the sleptons, the $\widetilde{e}_R$ and $\widetilde{\mu}_R$ are mass degenerate. The $\widetilde{\tau}$ states are mixed, with the $\widetilde{\tau}_1$ being slightly lighter than the $\widetilde{e}_R$. The sneutrinos $\tilde{\nu}$'s are mass degenerate. The mass of the $\widetilde{\chi}_1^{\pm}$, $\widetilde{\chi}_2^0$ and $\widetilde{\chi}_1^0$ is primarily a function of $m_{1/2}$, with a slight dependence on other parameters. The mass of the $\tilde{l}^{\pm}$'s and $\tilde{\nu}$'s is a function of m_0 and $m_{1/2}$. A notable point is that the $\widetilde{\tau}$ mass depends on $\tan(\beta)$ as well. Figure 2.6 shows the $\sigma(p\bar{p} \rightarrow \widetilde{\chi}_1^{\pm}\widetilde{\chi}_2^0)$; it is a smooth function of $m_{1/2}$, i.e. of the $\widetilde{\chi}_1^{\pm}$ mass.

Figure 7.4 shows the branching ratio of $\widetilde{\chi}_1^{\pm}\widetilde{\chi}_2^0$ to trileptons. Before examining the features of this plot, it is worthwhile to refresh the relevant decays of the $\widetilde{\chi}_1^{\pm}$ and $\widetilde{\chi}_2^0$. The decays

[1] the isolated track selection

proceed via 3−body or 2−body decays. The 3−body decays are :

$\widetilde{\chi}_1^{\pm} \rightarrow l^{\pm}\nu\widetilde{\chi}_1^0$, and

$\widetilde{\chi}_2^0 \rightarrow l^{\pm}l^{\mp}\widetilde{\chi}_1^0$ where an intermediate virtual W or Z boson or a virtual slepton[2] is implied.

The 2−body decays proceed as follows :

$\widetilde{\chi}_1^{\pm} \rightarrow \tilde{l}^{\pm}\nu$, and

$\widetilde{\chi}_2^0 \rightarrow \tilde{l}^{\pm}l^{\mp}$ where in each case the slepton decays to a lepton and the LSP, $\tilde{l}^{\pm} \rightarrow l^{\pm}\widetilde{\chi}_1^0$.

Let us now examine the various regions of Figure 7.4.

- Region $\mathbf{m}(\widetilde{\chi}_1^{\pm})<\mathbf{m}(\tilde{l}_R^{\pm})<\mathbf{m}(\tilde{\nu})$: This is the region where mass of the sleptons is higher than mass of the $\widetilde{\chi}_1^{\pm}$. The decays of the $\widetilde{\chi}_1^{\pm}$ and $\widetilde{\chi}_2^0$ proceed through a virtual W, Z boson or virtual sleptons, and the branching ratios to the different flavors of leptons (e, μ, τ) are roughly equal.

- Region $\mathbf{m}(\tilde{l}_R^{\pm})<\mathbf{m}(\widetilde{\chi}_1^{\pm})<\mathbf{m}(\tilde{\nu})$: This is the region where mass of the right-handed sleptons ($\widetilde{e}_R, \widetilde{\mu}_R$, and $\widetilde{\tau}_1$) is now below mass of the $\widetilde{\chi}_1^{\pm}$. The 2−body decays through sleptons enhance the overall branching ratio to leptons. The decays of the $\widetilde{\chi}_2^0$ to the three flavors of sleptons are roughly similar, but the $\widetilde{\chi}_1^{\pm}$ decays preferentially to $\widetilde{\tau}_1$'s.

- Region $\mathbf{m}(\tilde{l}_R^{\pm})<\mathbf{m}(\tilde{\nu})<\mathbf{m}(\widetilde{\chi}_1^{\pm})$: In this region, the mass of the sneutrinos has also dropped below that of $\widetilde{\chi}_1^{\pm}$. The $\widetilde{\chi}_2^0$ can now also decay as follow $\widetilde{\chi}_2^0 \rightarrow \tilde{\nu}\nu$ which does not contribute to the trilepton signal.

7.3.2 Exclusion in m_0 and $m_{1/2}$ plane

Using the method described in section 7.2, $\sigma\times$BR limits at 95% C.L. are placed on the $p\bar{p} \rightarrow \widetilde{\chi}_1^{\pm}\widetilde{\chi}_2^0 \rightarrow 3l$ process. By varying m_0 and $m_{1/2}$, nearly 100 points in the mSUGRA parameter space are generated. For each point, the $\sigma\times$BR limits are calculated. These limits are shown in the m_0-$m_{1/2}$ plane in Fig. 7.5. The limits are good in regions of high acceptance (such as at higher m($\widetilde{\chi}_1^{\pm}$), and in the 3−body region). In the 2−body

[2]Or sneutrino in case of $\widetilde{\chi}_1^{\pm}$.

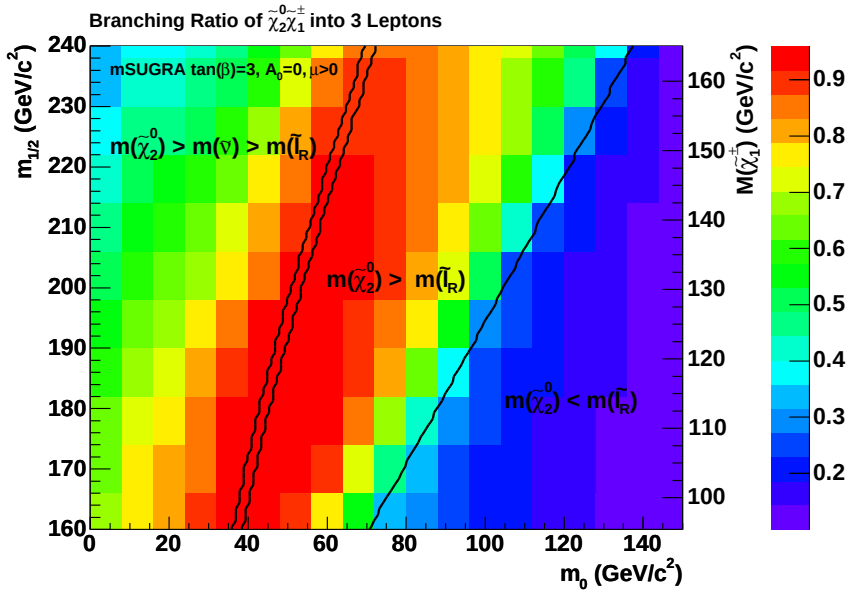

Figure 7.4: The figure shows the branching ratio to trileptons, BR($\widetilde{\chi}_1^\pm\widetilde{\chi}_2^0 \to 3l$) in the m_0-$m_{1/2}$ plane ($l = e, \mu, \tau$). The other mSUGRA parameters are kept constant at $\tan\beta = 3$, $A_0 = 0$, $\mu > 0$. The bin size is 10 GeV/c^2 $\times$ 10 GeV/c^2, although in certain places a finer grid is plotted.

region, an interesting sub-region is when m($\widetilde{\chi}_1^\pm$)−m($\tilde{l}^\pm$) is small. In this region, $\widetilde{\chi}_2^0 \to \tilde{l}^\pm l^\mp$ decay results in a lepton that is below the detection threshold of this analysis. The signal acceptance is reduced, and thus the limits worsen.

The results shown in Fig. 7.5 can be combined with the theory $\sigma\times$BR to obtain an excluded region in the mSUGRA parameter space. This is done by first plotting the difference between theory $\sigma\times$BR and observed $\sigma\times$BR limits, as shown in Fig. 7.6 for the generated signal points. Then Delaunay triangulation (as documented in Ref. [49]) is used to interpolate between the points and locate the zeros. The positive values represent regions which are excluded at 95% C.L., the negative values show non-excluded regions. The exclusion contour is then the locus of the zero difference between theory and observed 95% limits, i.e. the edge of exclusion region. This exclusion contour is shown in Fig. 7.7, where there are two 'lobes' of exclusion.

The right lobe [Region A, with m($\tilde{l}_R^\pm$)>m($\widetilde{\chi}_1^\pm$)] is in the region dominated by 3−body decays of $\widetilde{\chi}_1^\pm\widetilde{\chi}_2^0$. The left lobe [Region B, with m($\tilde{l}_R^\pm$)<m($\widetilde{\chi}_1^\pm$)] is in the region dominated

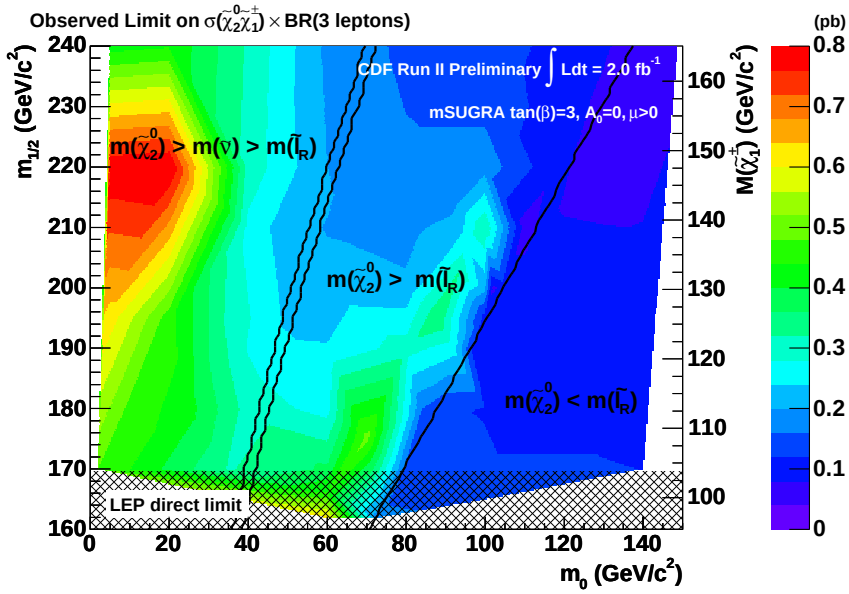

Figure 7.5: The figure shows the $\sigma\times$BR limits obtained in the plane defined by m_0 and $m_{1/2}$. The regions are described in the text.

by 2−body decays. The line representing small mass difference between $\widetilde{\chi}_1^{\pm}$(or $\widetilde{\chi}_2^0$) and $\tilde{l}_R^{\pm}$'s is also shown. Moving closer to this line from Region B towards Region A, the sleptons get closer to the $\widetilde{\chi}_1^{\pm}$ in mass. The 2−body decay of the $\widetilde{\chi}_2^0$ ($\widetilde{\chi}_2^0 \rightarrow \tilde{l}^{\pm}l^{\mp}$) leads to a soft lepton. This causes the acceptance of the analysis to worsen and thus this region cannot be presently excluded. At the left edge of the left lobe, the mass of $\tilde{\nu}$'s is getting smaller. This opens up the invisible decay of the neutralino ($\widetilde{\chi}_2^0 \rightarrow \tilde{\nu}\nu \rightarrow \nu\nu\widetilde{\chi}_1^0$). Hence the analysis acceptance drops and this region cannot be excluded.

7.3.3 Mass Limits

The exclusion limits can also be examined further by fixing m_0 in addition to $\tan\beta$, A_0, and sign(μ), and varying $m_{1/2}$ to obtain exclusion limits as a function of m($\widetilde{\chi}_1^{\pm}$). Figure 7.8 shows the expected and observed limits for $m_0 = 60$ GeV/c^2, in the region dominated by 2−body decays of the $\widetilde{\chi}_1^{\pm}$ and $\widetilde{\chi}_2^0$. In this case, $\widetilde{\chi}_1^{\pm}$'s with mass below approximately 145 GeV/c^2 are excluded where the theory and experimental curves intersect. Figure 7.9 shows the expected and observed limits for $m_0 = 100$ GeV/c^2 in the region dominated by

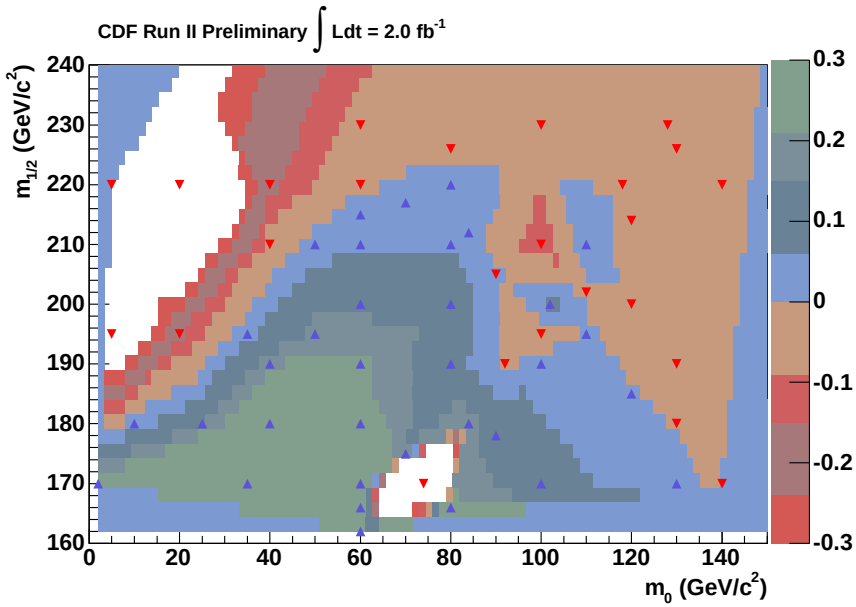

Figure 7.6: The figure shows theory($\sigma\times$BR)$-$Observed limits on $\sigma\times$BR (in pb). The positive values represent excluded regions at 95% C.L., and the negative values show non-excluded regions. Alternatively, the blue vertical triangles show excluded points, and the red upside-down triangles show the non-excluded points.

3$-$body decays of the $\widetilde{\chi}_1^{\pm}$ and the $\widetilde{\chi}_2^0$. At chargino mass of $\sim$ 130 GeV/c^2, the slepton becomes lighter than the $\widetilde{\chi}_1^{\pm}$. The $\widetilde{\chi}_2^0$ decays via the $\tilde{l}^{\pm}$ ($\widetilde{\chi}_2^0 \rightarrow \tilde{l}^{\pm}l^{\mp}$) giving a soft lepton below the analysis thresholds. The acceptance, and thus the limits worsen. The limits improve once the lepton is harder than the threshold. For this case, $\widetilde{\chi}_1^{\pm}$'s with mass below approximately 127 GeV/c^2 in this case.

7.3.4 Comparison with previous results

It is worthwhile to compare the results presented here with the published results from CDF [18]. The method used in the previous results is summarized below.

- The trilepton final state $\widetilde{\chi}_1^{\pm}\widetilde{\chi}_2^0 \rightarrow 3l + \not{E}_{\mathrm{T}}$ was split in to channels based on the final state lepton flavors. Thus, possible channels were eee, $\mu\mu e$, $e\mu\tau$, and so on. In practice, the channels considered were eeX, eeT, $\mu\mu X$, $e\mu X$, where X= e, μ. The $\mu\mu X$ channel was further split in to two based on the trigger path used, with slightly different event selections. The $e\mu X$ channel was also split in to two based on whether

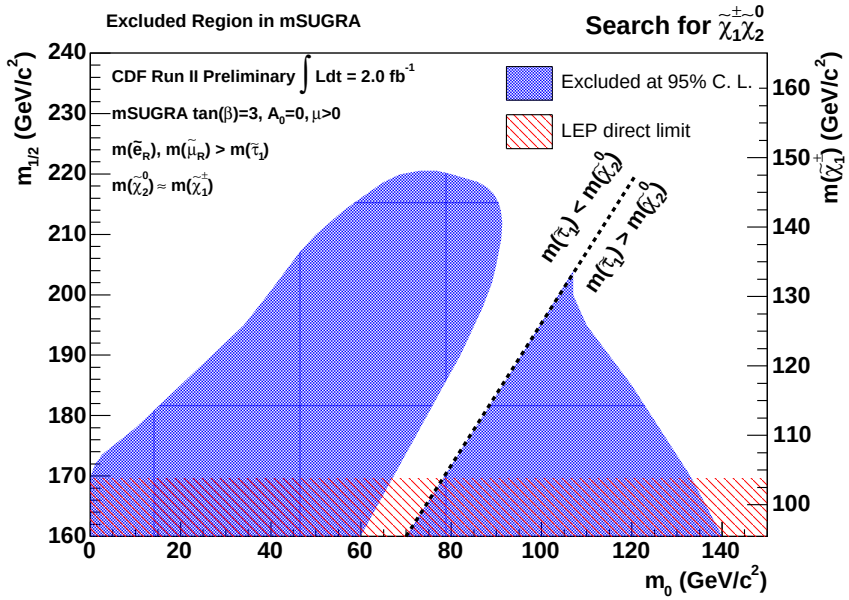

Figure 7.7: Figure shows exclusion region from this analysis in the $m_0 - m_{1/2}$ plane, with other mSUGRA parameters fixed as described. The LEP direct limit on chargino mass is also shown, along with lines representing significant mass relations. See text for more details.

the hardest lepton was the electron or the muon. The eeT channel required an isolated track as the third object.

- The different final states were combined to obtain exclusion limits on $\tilde{\chi}_1^{\pm}\tilde{\chi}_2^0$ production. However, this presents a formidable challenge, simply because the final analysis channels are not exclusive. Before the combination takes place, this overlap must be dealt with.

The approach used in this dissertation is significantly different from the published CDF result. This results in improved sensitivity of the analysis in terms of expected limits. In numerical terms, the method used here corresponds to a 25% improved sensitivity in terms of data; i.e. the previous method would require 2.5 fb^{-1} of data to achieve this same result.

7.4 Model-independent interpretation

The ideas and results that I shall discuss in this section have been presented in Ref. [50].

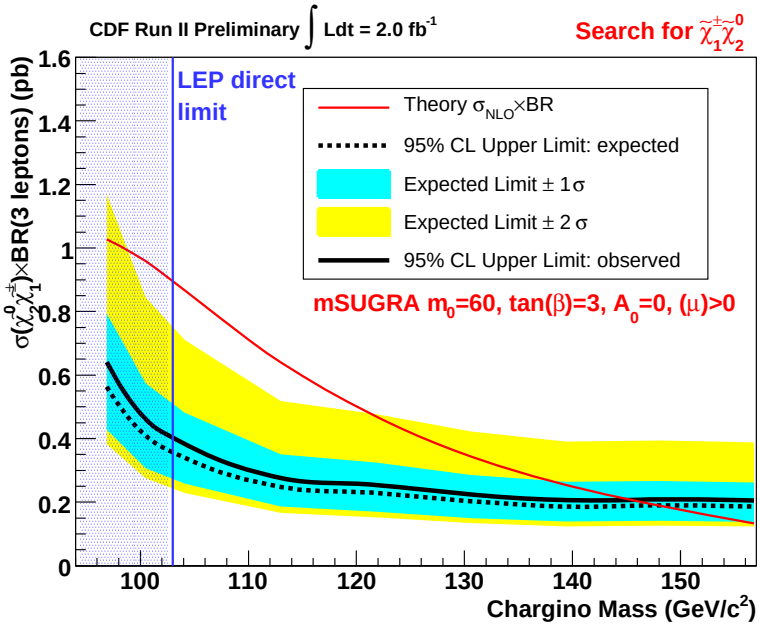

Figure 7.8: Figure shows the expected and observed limits for $m_0 = 60$ GeV/c^2 with other mSUGRA parameters fixed as described in the text. The red curve shows the theory $\sigma\times$BR. The black dashed curve shows the expected limit from this analysis (1 σ error in cyan, 2 σ error in yellow). The black solid curve shows the observed limit. We exclude chargino masses below 145 GeV/c^2 in this specific scenario.

The results presented in the previous sections have been shown in the m_0-$m_{1/2}$ plane of mSUGRA, with other mSUGRA parameters fixed as $\tan\beta = 3$, $A_0 = 0$, and $\mu > 0$. This leads naturally to the question of the applicability of the results when these fixed parameters are varied. In fact, the choice of parameters itself could be modified; a more "natural" choice of parameters are the physical masses which determine the exclusion or limits.

The cross section limits on $p\bar{p} \rightarrow \tilde{\chi}_1^{\pm}\tilde{\chi}_2^0 \rightarrow 3l$ within the framework of a certain model depend on two factors

- The expected background for a given integrated luminosity.
- The acceptance of signal events.

The expected background is fixed once the analysis selections are fixed. Usually, the background selections will roughly scale with luminosity. The signal acceptance on the other

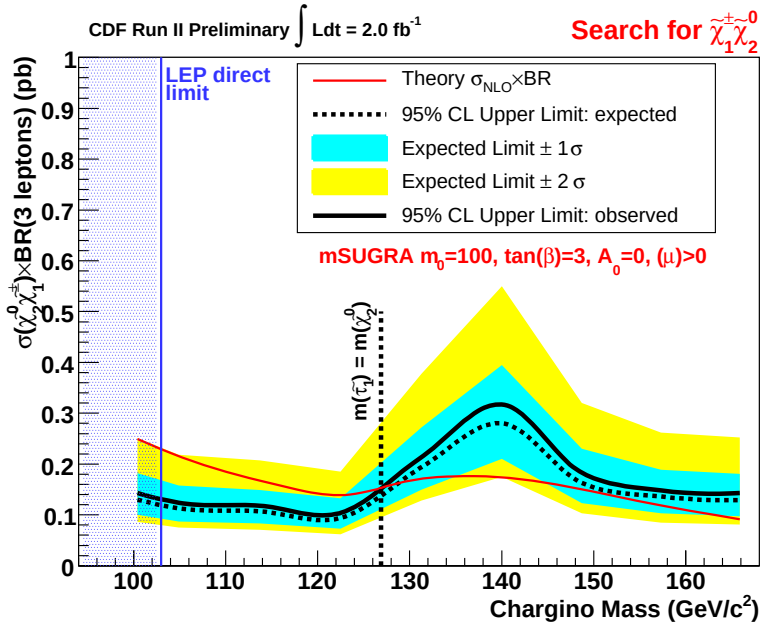

Figure 7.9: Figure shows the expected and observed limits for $m_0 = 100$ GeV/c^2. The red curve shows the theory $\sigma\times$BR. The black dashed curve shows the expected limit from this analysis (1 σ error in cyan, 2 σ error in yellow). The black solid curve shows the observed limit. We exclude chargino masses below 127.0 GeV/c^2 in this specific scenario.

hand will vary based on the model considered.

Consider the specific case of the analysis presented in this dissertation. The SM backgrounds are calculated and are shown in Table 7.1. The observation in data is consistent with these backgrounds. The only missing piece in determining whether a specific supersymmetry model is ruled out or not is the signal acceptance for that model.

Usually, the signal acceptance is determined by generating dedicated simulation samples. While this method will give accurate results, it is time-consuming. It would be more useful if one could determine exclusion based on simple characteristics of the model. The trilepton analysis acceptance depends on a few kinematic parameters : the mass of the $\widetilde{\chi}_1^{\pm}$ and $\widetilde{\chi}_2^0$, the mass difference of the $\widetilde{\chi}_1^{\pm}$, $\widetilde{\chi}_2^0$ and the LSP, and the masses of the intermediate sparticles[3]. These parameters are immediately obtained from the model considered without any generation of samples.

[3]If they are relevant in the decay chain

An added complication for the trilepton acceptance comes from the fact that e, μ acceptance is greater than τ acceptance; stated differently, the trilepton acceptance depends strongly on the number of τ's in the final state. This complication is dealt with in the following way. The trilepton acceptance is categorized in to four exclusive and collectively exhaustive final states based on the presence of a τ in the final state ($l = e, \mu$):

- lll, i.e., 0τ : There are no τ's in the final state.
- $ll\tau$, i.e. 1τ : There is a single τ in the final state. This happens when the $\widetilde{\chi}_1^{\pm}$ decays to $\tau\nu\widetilde{\chi}_1^0$.
- $l\tau\tau$, i.e. 2τ : There are two τ's in the final state. This happens when the $\widetilde{\chi}_2^0$ decays to $\tau\tau\widetilde{\chi}_1^0$.
- $\tau\tau\tau$, i.e. 3τ : All three leptons in final state are τ's.

The total acceptance of the analysis A_T is then given by

$$A_T = \sum_{n=0}^{3} A_n \cdot F_n \tag{7.3}$$

where A_n is the acceptance in the final state with n τ's [4], and F_n is the fraction of trilepton events in the n τ final state[5].

The notable point here is that A_n and F_n are now independent of each other. A_n is the acceptance which depends on the kinematic parameters mentioned above; F_n depends on the model.

The task of parametrizing A_n is now accomplished by making use of the mSUGRA model. The analysis selections are implemented in PYTHIA-based simulations to obtain the acceptances. A number of mSUGRA points are obtained by varying m_0, $m_{1/2}$ and $\tan\beta$ and keeping A_0 and sign(μ) constant. The trilepton events are split in to four subsamples

[4] $A_n = \frac{\text{Events with } n\tau\text{'s passing all selections}}{\text{Events with } n\tau\text{'s}}$

[5] $F_n = \frac{\text{Events with } n\tau\text{'s}}{\text{Total trilepton events}}$

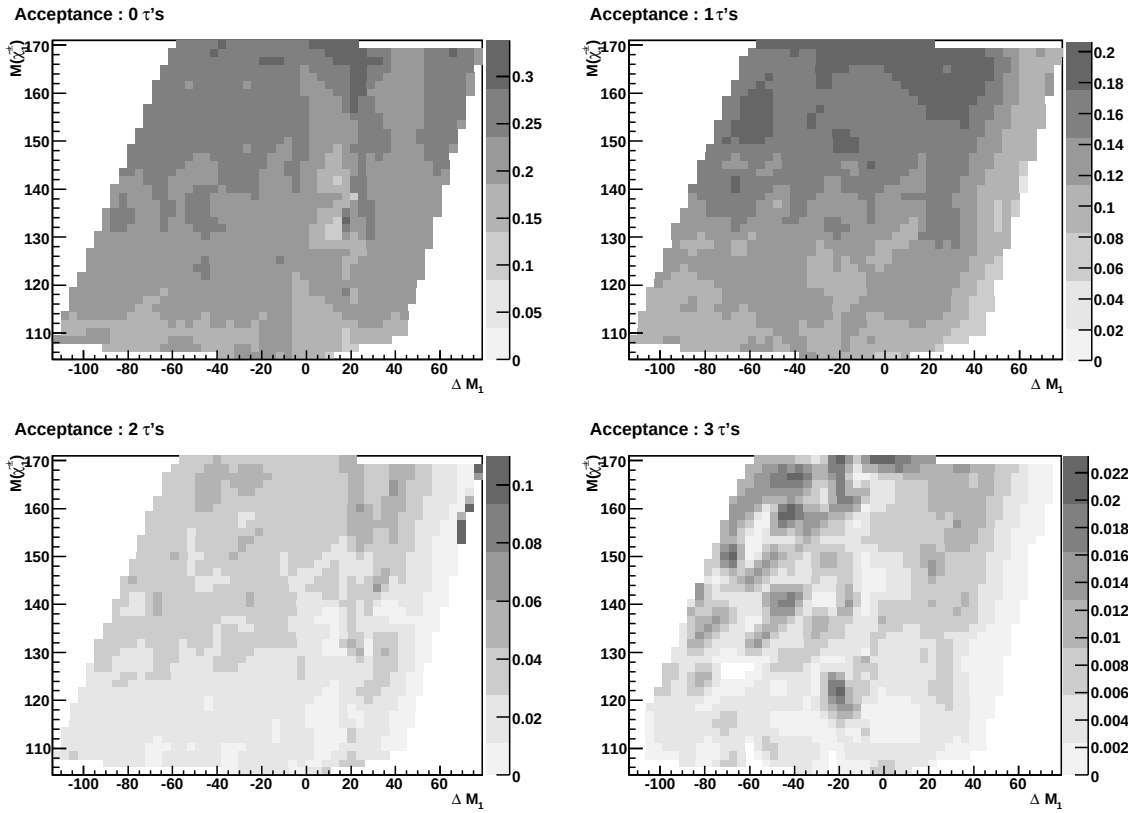

Figure 7.10: We show the acceptance as a function of m($\widetilde{\chi}_1^{\pm}$) and ΔM_1 = m($\widetilde{\chi}_1^{\pm}$) − m($\widetilde{\tau}$) for the four subsamples with different number of τ's in the final state.

according to the number of τ leptons in the final state. Figure 7.10 shows the acceptance as a function of m($\widetilde{\chi}_1^{\pm}$) and ΔM_1 = m($\widetilde{\chi}_1^{\pm}$)-m($\widetilde{\tau}_1$) in each subsample. To simplify the illustration of the principle, we choose the regions of smooth acceptance :

m($\widetilde{\chi}_1^{\pm}$)> 104 GeV/c^2, to remain above constraints from LEP experiments,

m($\widetilde{\chi}_1^{\pm}$)<m($\tilde{\nu}$),

$\Delta M_1 < -2$ GeV/c^2 or $\Delta M_1 > 15$ GeV/c^2, where ΔM_1 = m($\widetilde{\chi}_1^{\pm}$) − m($\widetilde{\tau}_1$).

The acceptance A_n is fit in each subsample

$$A = p_0 + p_1 \frac{m(\widetilde{\chi}_1^{\pm})}{100 \text{ GeV}/c^2} + p_2 \left(\frac{m(\widetilde{\chi}_1^{\pm})}{100 \text{ GeV}/c^2}\right)^2 \tag{7.4}$$

The parameters of these fits are shown in Table 7.3; they approximate the acceptance to within 20%. The fits are tested for various points in mSUGRA space (by now varying four parameters), and the results are shown in Table 7.4. A couple of examples of applying these

results to specific cases is shown in Ref. [50].

Subsample	p_0	p_1	p_2
0τ's	-0.19	0.49	-0.14
1τ's	-0.044	0.14	0
2τ's	-0.12	0.19	-0.055
3τ's	-0.008	0.01	0

Table 7.3: The values of the parameters for the acceptance fits in the different subsamples. The acceptance is given by Eq. 7.4.

m_0	$m_{1/2}$	A_0	$\tan\beta$	Actual Acc.	Calc. Acc.
60	190	0	3	0.08810	0.08000
60	190	-200	3	0.07840	0.07160
60	190	200	3	0.10260	0.08869
70	190	0	5	0.07750	0.06921
70	190	-200	5	0.06450	0.05459
70	190	100	5	0.08040	0.07532
70	180	0	10	0.03210	0.03066
70	180	-100	10	0.02960	0.02600
70	180	200	10	0.03880	0.03801
120	180	0	3	0.12080	0.11649
120	180	-200	3	0.12760	0.12108
120	180	200	3	0.11590	0.11322
120	180	0	5	0.11340	0.11719
120	180	-200	5	0.12850	0.12183
120	180	200	5	0.11180	0.11242
120	180	0	10	0.11070	0.11226
120	180	-200	10	0.10960	0.11398
120	180	200	10	0.10550	0.10923
1000	200	0	10	0.15890	0.15250
1000	200	-200	10	0.16300	0.15421
1000	200	200	10	0.16160	0.15250

Table 7.4: The comparison of the actual acceptance from Pythia (Actual Acc.) with the acceptance calculated using the fits (Calc. Acc.) is shown for a set of mSUGRA points. $\mu > 0$ for all points.

7.4.1 Improvements

The results described above were obtained within the framework of mSUGRA. Thus, the mass relation between $\widetilde{\chi}_1^{\pm}$ and $\widetilde{\chi}_1^0$ was fixed at m($\widetilde{\chi}_1^{\pm}$)≈2m($\widetilde{\chi}_1^0$).

The next step is to vary the mass difference $\Delta M_2 = \mathrm{m}(\widetilde{\chi}_1^{\pm}) - \mathrm{m}(\widetilde{\chi}_1^0)$. In cases where the decay is 2−body, the mass of the slepton is also relevant. This is accounted for by

the variable $\Delta M_1 = \mathrm{m}(\widetilde{\chi}_1^{\pm}) - \mathrm{m}(\tilde{l}^{\pm})$. Figure 7.11 shows the acceptance in the 0τ and 1τ final states as a function of $\mathrm{m}(\tilde{l}^{\pm})-\mathrm{m}(\widetilde{\chi}_1^0)$ for different values of $\mathrm{m}(\widetilde{\chi}_1^{\pm})$. $\mathrm{m}(\widetilde{\chi}_1^0)$ is fixed at 70 GeV/c^2. $\mathrm{m}(\widetilde{\chi}_1^{\pm})$ varies from 110 GeV/c^2 for the red curve with least acceptance to 160 GeV/c^2 for the green curve in increments of 5 GeV/c^2. Plots such as this one will be used to parametrize the trilepton acceptance in terms of $\mathrm{m}(\widetilde{\chi}_1^{\pm})$, $\mathrm{m}(\widetilde{\chi}_1^{\pm})-\mathrm{m}(\widetilde{\chi}_1^0)$, and $\mathrm{m}(\tilde{l}^{\pm})$. Further updates of Ref. [50] will contains full details.

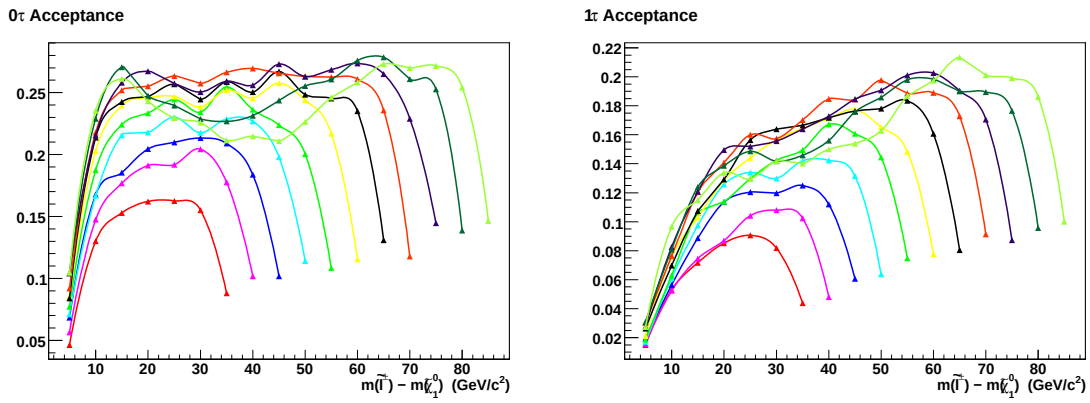

Figure 7.11: The acceptance as a function of $\mathrm{m}(\tilde{l}^{\pm})-\mathrm{m}(\widetilde{\chi}_1^0)$ for different values of $\mathrm{m}(\widetilde{\chi}_1^{\pm})$. $\mathrm{m}(\widetilde{\chi}_1^0)$ is fixed at 70 GeV/c^2. $\mathrm{m}(\widetilde{\chi}_1^{\pm})$ varies from 110 GeV/c^2 for the red curve with least acceptance to 160 GeV/c^2 for the green curve in increments of 5 GeV/c^2.

7.5 Conclusions

In this dissertation, I have described a supersymmetry search performed using data collected at the CDF experiment at the Tevatron $p\bar{p}$ collider. An integrated luminosity of 2 fb^{-1}was used to search for the trilepton decay of chargino-neutralino associated production. The standard model backgrounds were calculated using a variety of methods including simulated samples, and data-driven estimates.

The results indicate no signs of new physics. These null results are used to constrain the mSUGRA model of supersymmetry. An exclusion region in the m_0-$m_{1/2}$ plane is presented which extends beyond the results obtained from the LEP experiments. A mass limit on the $\widetilde{\chi}_1^{\pm}$'s is also obtained; with a favorable choice of parameters, $\widetilde{\chi}_1^{\pm}$'s with mass less than 145 GeV/c^2 are ruled out.

Appendix A

Trigger Efficiency

In this chapter, we shall discuss the measurement of the trigger efficiency of the dielectron trigger mentioned in Section 4.1.

The combined (L1-L2-L3) lepton trigger efficiencies are used as individual event weights in the trilepton analysis. The efficiency measurement for the L1_CEM4_PT4, L2_CEM4_PT4_CES2, L2_CEM4_PT4_CES3, and L3_CEM4 triggers is presented here.

A.1 Sample

Unbiased electrons from a single 8 GeV electron triggered dataset to use for trigger efficiency measurement. The integrated luminosity of the sample used for the described measurement is about 505 $\text{pb}^{-1}$and the sample has about 31.8 million events. This dataset is a lepton calibration dataset; it is dynamically prescaled and has three paths to accept electrons

- Path A has all three levels (1,2,3) included with $E_{\text{T}} \geq 8$ GeV and XFT $p_{\text{T}} \geq 8$ GeV at levels 1,2,3.
- Path B has no level 2 requirements, just a prescale of 100.
- Path C has no level 2,3 requirements, just level 1 and a prescale of 1000.

A.1.1 Trigger Bias Removal

Trigger bias is removed by using the following algorithm for probe electron selection :

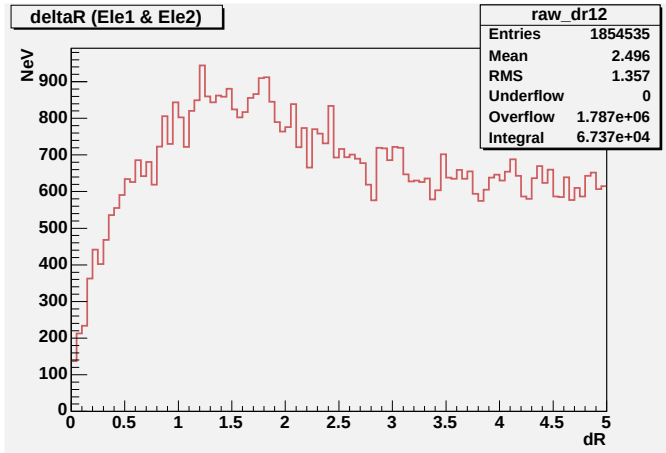

Figure A.1: Figure shows the ΔR distribution between leading and next-to leading electron. A cut of $\Delta R \geq 0.5$ is applied.

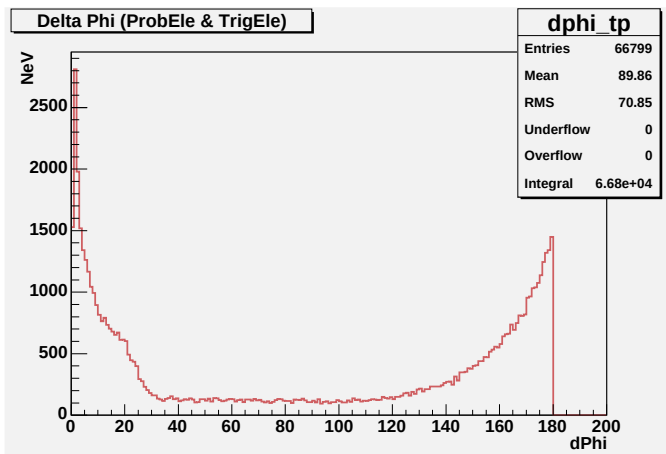

Figure A.2: Figure shows the $\Delta\phi$ distribution between trigger and probe electron.

If Ele^1 $>$ 8 GeV AND Ele^1 passes the 8 GeV trigger requirements Ele^2 is the probe electron and vice versa.

Both electrons are required to pass all offline identification requirements as listed in Table 3.1 for tight electrons. In addition probe electrons are required to have fractional isolation $E_{\mathrm{T}}^{iso}/E_{\mathrm{T}} \leq 0.1$. The probe and trigger electrons are also required to be physically separated by requiring $\Delta R_{\eta\phi} \geq 0.5$ between trigger and probe electron. The probe electrons are then matched to trigger objects at Levels 1,2,3. The details for matching at each level are described in the respective sections for the trigger efficiency.

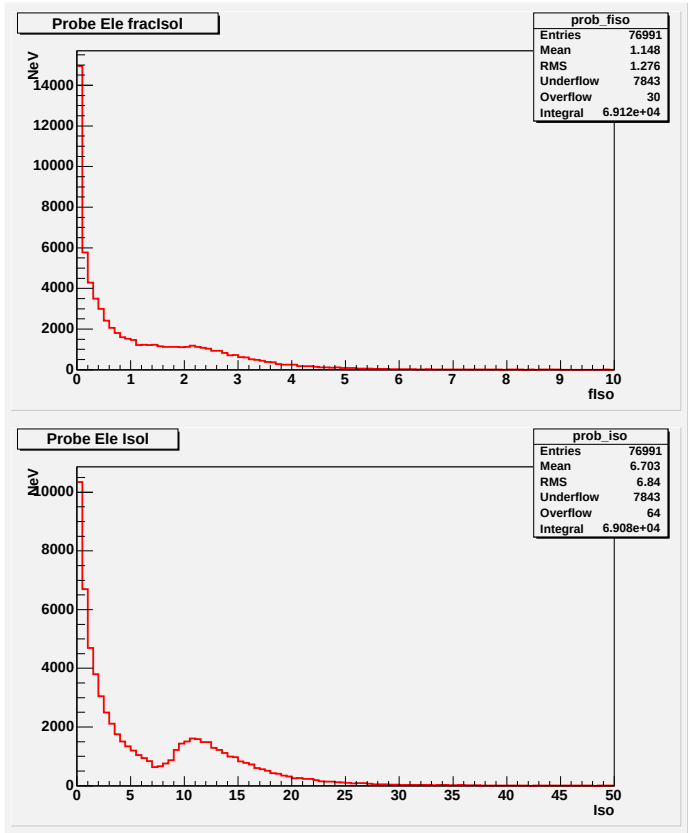

Figure A.3: Figure shows the fractional isolation of probe electron. $E_{\mathrm{T}}^{iso}/E_{\mathrm{T}} \leq 0.1$ is required.

A.2 L1_CEM4_PT4 Efficiency

A.2.1 Trigger Implementation

Requirements :

- Trigger should find a single trigger tower which has Tower $E_{\mathrm{T}} > 4GeV$.
- Trigger should find that $E^{HAD}/E^{EM} \leq 0.125$.
- Trigger should find an XFT track with $p_{\mathrm{T}}^{XFT} > 4GeV$
- This XFT track should match the trigger tower selected above[1].

[1]It should be noted that this XFT track - trigger tower matching is done only in ϕ as the XFT tracks have only ϕ information and no η information.

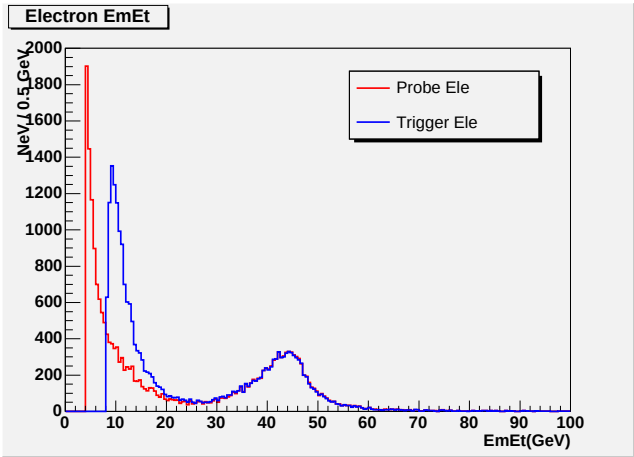

Figure A.4: Figure shows the E_{T} distribution of trigger and probe electrons.

A.2.2 How we measure efficiency

Efficiency is measured by checking whether the offline electron selected by the method described in previous sections would have passed the L1_CEM4_PT4 trigger. In other words, all electrons selected previously after all identification and isolation etc. cuts are the denominator and of those, the electrons which pass the Level 1 requirement form the numerator. The ratio as a function of offline electron E_{T} is taken as the Level 1 efficiency. First the Level 1 objects (viz. Trigger tower and XFT track) corresponding to the offline electron are found.

Matching to XFT track

Tl2D-level information [51] is used to obtain paramters of the XFT tracks. XFT tracks which match the offline electron's track are selected by extrapolating the XFT and offline track to the four axial superlayers and comparing their positions [52]. If the two tracks are separated by less than ten pixels at a particular superlayer, then the tracks are considered matched at that superlayer. For a full match, tracks must match at least at three out of four possible superlayers (for 4-layer XFT tracks) or at three out of three superlayers (for 3-layer XFT tracks). It is possible to find more than one XFT track which matches the offline track. In this case all such matched tracks are saved and then the track which passes

all trigger requirements is picked[2].

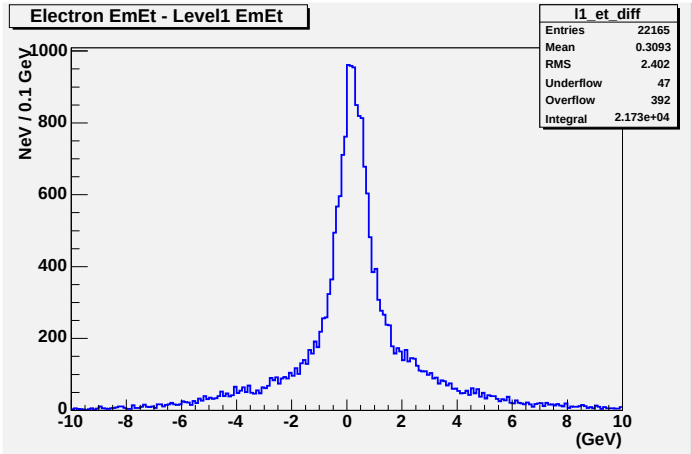

Figure A.5: This is a plot of offline EmE_{T} − L1 E_{T} .

Matching to trigger tower

The offline electron's seed η and ϕ indices are used to match to a trigger tower's $\eta - \phi$ indices. The trigger tower EM and HAD energy for these $\eta - \phi$ indices is then extracted from the DCAS data bank. The XFT track selected above is then matched to the trigger tower using the ϕ indices of each. In the unlikely event that more than one such XFT track matched, the one with highest p_{T} is chosen.

The matching trigger tower and XFT track are then tested for passing the trigger requirements. Thus the denominator events are those where an offline electron passing all (clean-up, ID) requirements exits, and the numerator are events where the offline electron is matched to level 1 objects AND these objects pass the trigger requirements.

A.2.3 Efficiency

Figure A.6 shows the Level 1 efficiency as a function of the offline E_{T} .

[2]It should be noted that this mimicks the trigger behaviour.

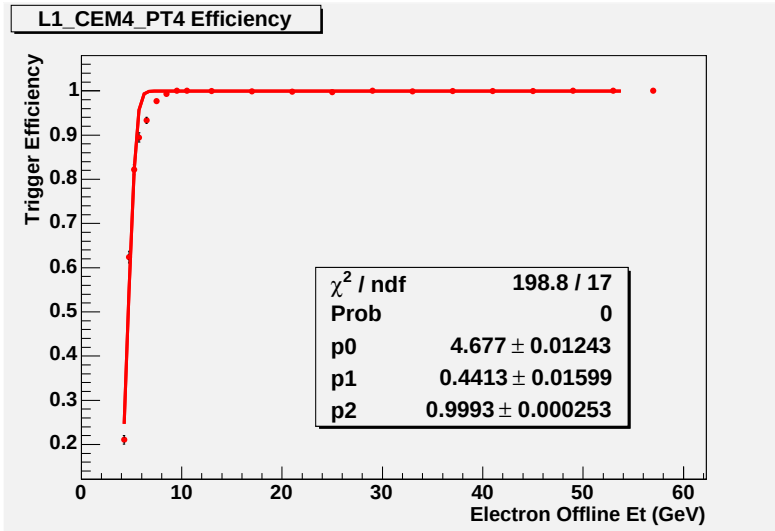

Figure A.6: The L1_CEM4_PT4 Efficiency as a function of the offline E_{T} . The fit is $\epsilon = 0.5p_2 \cdot (1 + erf(t))$, where $t = (E_{\mathrm{T}} - p_0)/2p_1$ and p_2 is the asymptotic efficiency.

A.3 L2_CEM4_PT4_CES2 Efficiency

The level 2 trigger requirements are similar to level 1 requirements but with much improvements.

A.3.1 Trigger implementation

Requirements :

- Trigger should find an EM cluster with $E_{\mathrm{T}} > 4$ GeV
- Trigger should find $E^{HAD}/E^{EM} \leq 0.125$.
- Trigger should find CES $E_{\mathrm{T}} > 2$ GeV or CES $E_{\mathrm{T}} > 3$ GeV
- Trigger should find an XFT track with $p_{\mathrm{T}}^{XFT} > 4GeV$
- Trigger requires that the XFT track should match a CES wire cluster

The same XFT track information from Level 1 is propagated for use in Level 2. The energy measurement, however, is more accurate because the resolution is 0.25 GeV as opposed to 0.5 GeV at Level 1. The other important piece at Level 2 is that it uses the

CES detector to trigger on electrons. Instead of EM tower E_{T}, the EM cluster E_{T} is available and it is used as a trigger requirement.

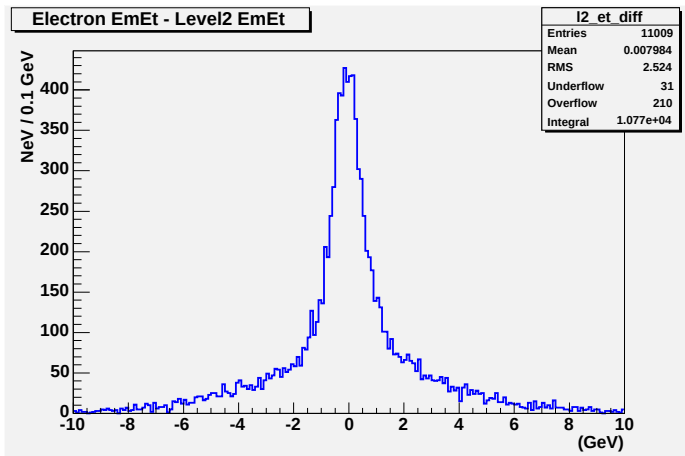

Figure A.7: This is a plot of offline EmE_{T} − L2 E_{T} .

A.3.2 How we measure efficiency

All electron candidates that pass Level 1 requirement form the denominator for the Level 2 efficiency measurement. Those which pass the L2 requirements as listed above form the numerator and the ratio as a function of offline electron E_{T} is taken as the Level 2 efficiency.

Matching to trigger cluster

To find the Level 2 EM cluster, the seed η-ϕ indices of the offline electron are once again matched with the Level 2 cluster η-ϕ indices. The indices are allowed to be different by as much as 1 unit in η and/or ϕ to account for boundary effects.

Simulation of trigger decision for CES

The CES cluster E_{T} is reconstructed from the wire energies. Due to zero suppression at level 2 readout, a complete reconstruction is not possible. To add to the difficulty of the task, the ntuple-maker zeroes wire ADC readout whenever it is below 55 counts. However, it is expected that the average pedestal of an ADC count for each wire is 48. Also, for a

signal electron, the ADC count is expected to be above 100. Therefore each zeroed channel (either due to online readout or ntuple-maker cut) is filled with an ADC readout 48 and the trigger decision is simulated. This method is used in other trigger simulation programs as well and is a standard CDF procedure. The difference in efficiency due to this procedure is taken as a systematic error in the efficiency.

The XFT track is propagated to the CES detector (radius of 184.15 cm) and a match to the cluster in ϕ is performed in a local distance of ± 2.5 cm. The information of wires that are lit are stored in a word called "hitbit".

A.3.3 Efficiency

The level 2 trigger efficiency is flat as a function of electron E_{T}. The fitted efficiency is shown in Figure A.8 and Figure A.9.

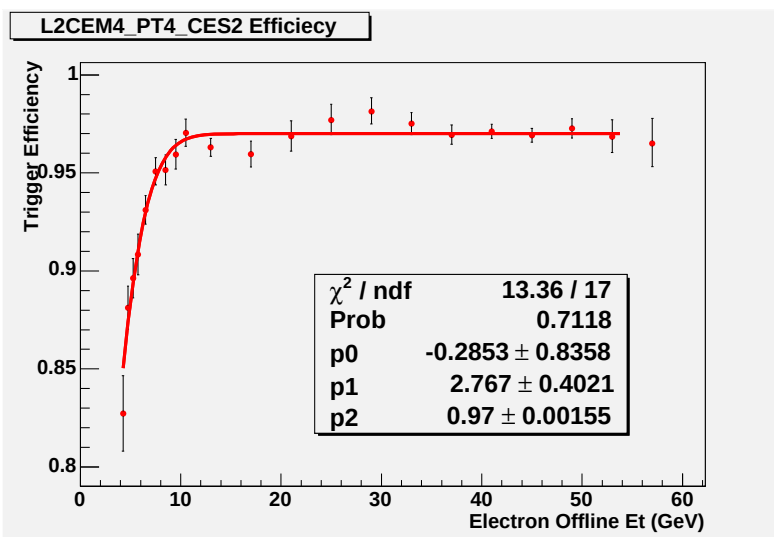

Figure A.8: The L2_CEM4_PT4_CES2 Efficiency as a function of the offline E_{T} . The fit is $\epsilon = 0.5p_2 \cdot (1 + erf(t))$, where $t = (E_{\mathrm{T}} - p_0)/2p_1$ and p_2 is the asymptotic efficiency.

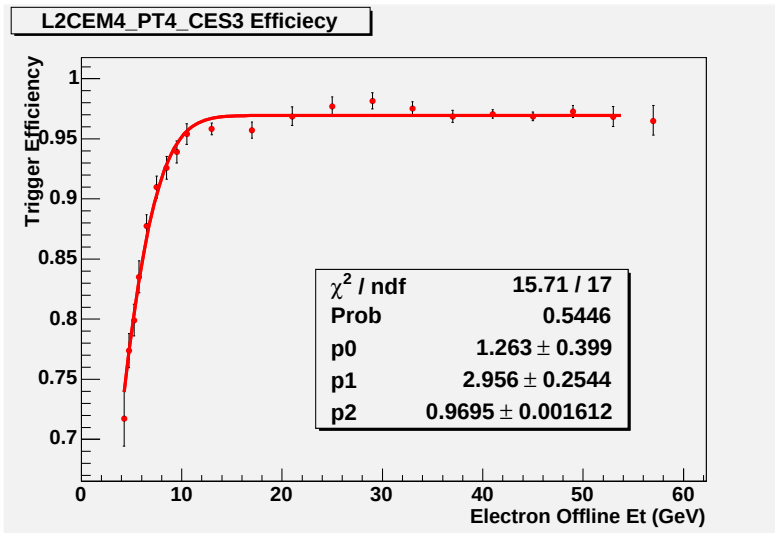

Figure A.9: The L2_CEM4_PT4_CES3 Efficiency as a function of the offline E_{T} . The fit is $\epsilon = 0.5p_2 \cdot (1 + erf(t))$, where $t = (E_{\mathrm{T}} - p_0)/2p_1$ and p_2 is the asymptotic efficiency.

A.4 L3_CEM4_PT4 Efficiency

A.4.1 Trigger implementation

At Level 3, nearly all corrections(if any) have been applied and most of the reconstruction is already done. The triggers are expected to be highly efficient.

Requirements :

- $E_{\mathrm{T}} > 4GeV$, $p_{\mathrm{T}} > 2GeV$, $E^{had}/E^{EM} \leq 0.125$
- $|\Delta z| \leq 8cm$
- $\chi^2 \leq 20$, $L_{shr} \leq 0.2$

A.4.2 How we measure efficiency

The offline electron is matched to the Level 3 EM objects found in the L3SummaryBlock; a summary of all Level 3 trigger objects available offline. The closest Level 3 EMobject to the offline electron in $\eta - \phi$ space is selected. This matched L3 EM object is then tested for the trigger requirements. Here the denominator events are those which pass Level 2

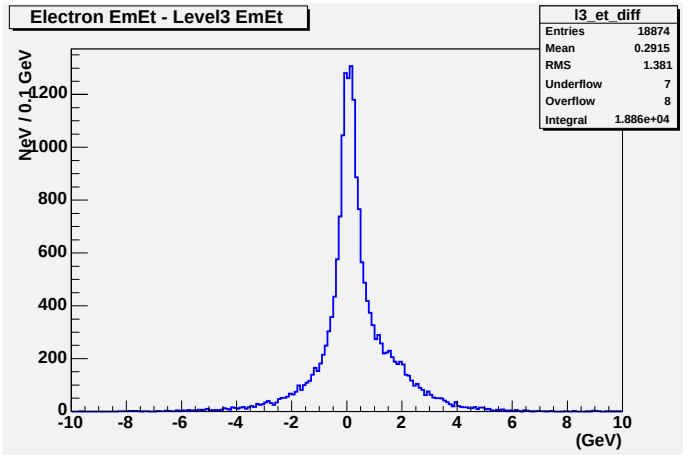

Figure A.10: This is a plot of offline EmE_{T} − L3 E_{T} .

requirements, and the numerator events are those events which pass Level 2 AND Level 3 requirements.

A.4.3 Efficiency

Figure A.11 shows the Level 3 efficiency as a function of the offline E_{T} with Level 2 CES3 requirement.

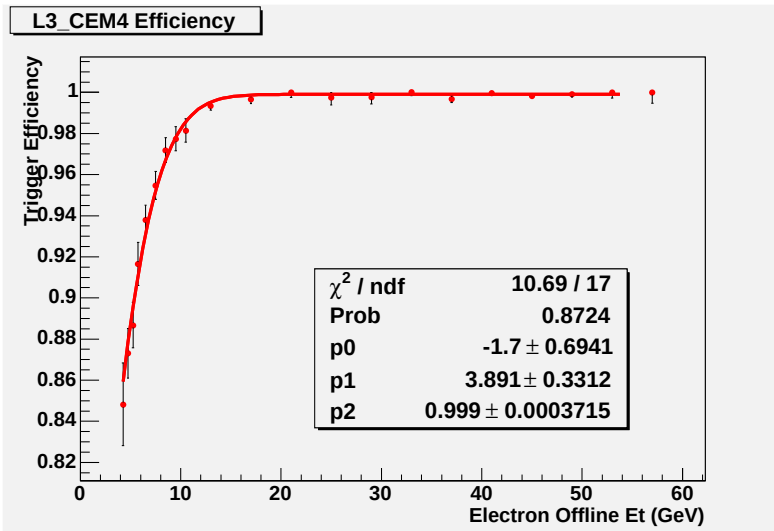

Figure A.11: The L3_CEM4_PT4 Efficiency as a function of the offline E_{T} . The fit is $\epsilon = 0.5p_2 \cdot (1 + erf(t))$, where $t = (E_{\mathrm{T}} - p_0)/2p_1$ and p_2 is the asymptotic efficiency. This is efficiency for case where Level 2 has CES 3 GeV requirement.

A.5 Total Efficiency

The total efficiency as a function of offline E_{T} is shown in Fig A.12 for CES2 at Level 2 and Fig A.13 for CES3 at Level 2. The results of the efficiencies for each level are given in Table A.1. The total trigger efficiency at plateau is 95.6±0.2(stat)% (Refer Figure A.12) .

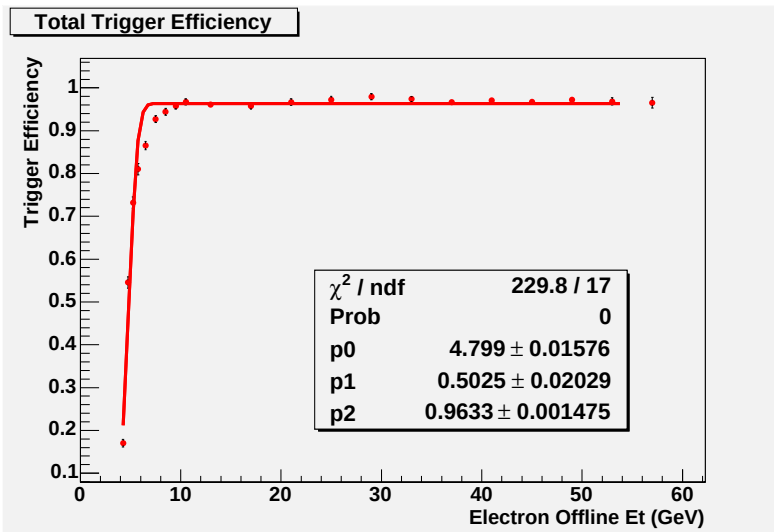

Figure A.12: The total CEM4_PT4 efficiency as a function of the offline E_{T} . The fit is $\epsilon = 0.5p_2 \cdot (1 + erf(t))$, where $t = (E_{\mathrm{T}} - p_0)/2p_1$ and p_2 is the asymptotic efficiency. This is efficiency for case where Level 2 has CES 2 GeV requirement.

Level	Efficiency
Level 1	99.9±0.1%
Level 2 CES2	97.0±0.1%
Level 2 CES3	97.0±0.1%
Level 3	99.9±0.1%
Total wih CES2	96.3±0.1%
Total wih CES3	96.2±0.1%

Table A.1: The efficiency for Level 1, Level 2, and Level 3 and total trigger efficiency.

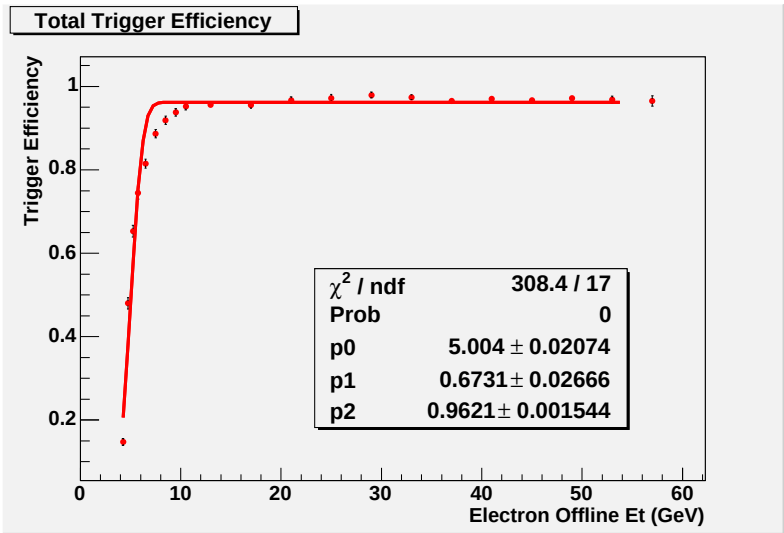

Figure A.13: The total CEM4_PT4 efficiency as a function of the offline E_{T} . The fit is $\epsilon = 0.5p_2 \cdot (1 + erf(t))$, where $t = (E_{\mathrm{T}} - p_0)/2p_1$ and p_2 is the asymptotic efficiency. This is efficiency for case where Level 2 has CES 3 GeV requirement.

Appendix B

Electron Identification Scalefactors

The electron identification scale-factor between data and Monte Carlo (MC) is a requisite measurement for the susy trilepton analyses. Using low E_{T} electrons ensures a higher acceptance for this analysis. Hence a low E_{T} efficiency study is vital to obtain a scale-factor between data and MC. This scale-factor will be essential to estimate the expected number of signal and background events in data.

Unbiased electrons from the single-electron calibration dataset are used. The method of obtaining the unbiased sample is decribed in section B.1. The identification (ID) and isolation (Iso) scale-factors are measured separately, and then combined to obtain a total scale-factor between data and MC. Note that a previous such study has been described in Ref. [33]

B.1 Samples

B.1.1 DATA samples

Drell-Yan (DY) events are used to measure the electron ID/Iso efficiency. A sample of unbiased electrons is obtained using the electron calibration data sample. This sample is triggered on a single electron with $E_{\mathrm{T}} > 8$ GeV, and $p_{\mathrm{T}} > 8$ GeV.

Removing trigger bias for measuring efficiency

Removing trigger bias is an important step as ignoring this could lead to artificially high efficiencies for data electrons and an incorrect scale-factor.

The trigger has an 8 GeV requirement on electron E_{T} and p_{T} . Every event must have one electron with $E_{\mathrm{T}} \geq 8$ GeV and $p_{\mathrm{T}} \geq 8$ GeV, passing all requirements in Table B.1 and isolation requirements(Table B.3). If such an electron is found, it is called as trigger electron and the 'other' electron in the event (as defined by conditions in Table B.2) is called probe electron. The 'other' electron is required to pass the baseline cuts in Table B.1.

Base cuts
$E_{\mathrm{T}} \geq 8$ GeV
$p_{\mathrm{T}} \geq 2$ GeV
trk $\lvert z_0 \rvert \leq 60$ cm
CES Fiducial Ele

ID variables
$E/p \leq 2.0$
HadE/EmE $\leq$(0.055 + 0.00045$\times E_{\mathrm{T}}$)
-3.0 cm$\leq$ CES Signed Δx $\leq$1.5 cm
CES $\lvert \Delta z \rvert \leq 3$ cm
CES $\chi^2_{strip} \leq 10$
Lshr ≤ 0.2
Axial Seg(5 hits) ≥ 3
Stereo Seg(5 hits) ≥ 2

Table B.1: The left table shows the baseline cuts. The right table shows the ID variables for which efficiency is measured.

Thus if an event has two electrons which are trigger electrons, then their partners are probe electrons, and the event has two probe electrons. If there is only one trigger electron in the event, then its partner is a probe electron. In addition, the requirements in Table B.2 are also enforced.

B.1.2 Monte Carlo samples

The $Z \rightarrow ee$ samples are used to measure the ID/Iso efficiency for MC electrons. The MC includes the off-shell Z contribution as well. The MC samples have a generator-level cut on the invariant mass of the two electrons, $M_{ee} \geq 20$ GeV/c^2.

B.2 Method

The electron ID efficiency/scale-factor and isolation efficiency/scale-factor are measured separately and then multiplied to obtain the total scale-factor. This is done by measuring the ID and isolation cut efficiency as 'all-but-one' efficiencies - for the ID efficiency, the isolation cut is applied while forming the denominator and then the ID criteria are applied to obtain the numerator. Thus the ID efficiency is measured with respect to the isolation. The same procedure is repeated to measure isolation efficiency viz. the ID criteria are applied to obtain the denominator and then isolation is applied to obtain the numerator and thus the efficiency.

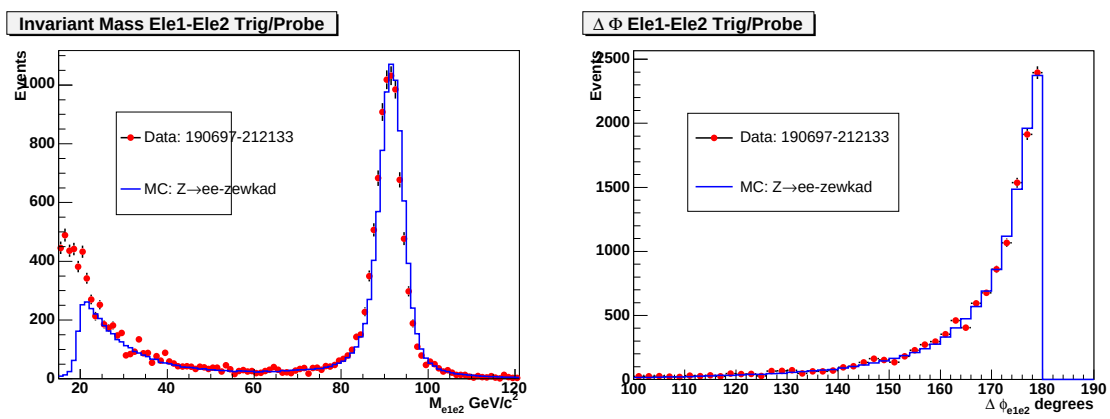

Figure B.1: Figure shows the invariant mass and $\Delta\phi$ distribution of the trigger and probe electrons. Same-sign events are subtracted in both. The mass distribution is normalized to number of events between 76 and 106 GeV/c^2. The $\Delta\phi$ distribution is normalized to number of events between 160 and 180 degrees. The $\Delta\phi$ distribution is plotted after requiring invariant mass $\geq$ 20 GeV/c^2.

Drell-Yan (DY) electrons ($\Delta\phi_{ee} > 160$ degrees) are used to do the measurement. The background is estimated using same-charge electrons. The background thus estimated is about 20% for data electrons with 8 $\leq E_{\mathrm{T}}$ /GeV$\leq$ 20 and about 2% for MC electrons. By doing the 'all-but-one' procedure, the backgrounds can be controlled much better. The validity of this procedure has been crosschecked by measuring efficiencies in MC of all cuts at once instead of 'all-but-one'. MC events have very little background, and thus the combined efficiency of all ID and Iso is expected to be equal to the product of the 'all-but-one' ID

and Iso efficiencies. The results of this check are shown in Ref. [32].

The scale-factor for electrons with $E_{\mathrm{T}} > 20$ GeV can also be measured using the Z resonance. Since this method is used for obtaining blessed numbers(cdf7309,cdf7950,cdf8274), we also use the same method for electrons with $E_{\mathrm{T}} > 20$ GeV to crosscheck results obtained by using DY($\Delta\phi_{ee} > 160$ degrees) electrons. Events with invariant mass (M_{ee}) in the window 76 to 106 GeV/c^2 are selected. These electrons are used to measure the ID/Iso efficiencies in data and MC. For electrons with $E_{\mathrm{T}} \geq 20$ GeV, the background is less than 1% for both data and MC electrons.

It should be noted that there is an implicit cut $E^{HAD}/E^{EM} \leq 0.125$ while reconstructing a CDF EM object. Thus the efficiency we measure is over and above this E^{HAD}/E^{EM} cut.

Drell Yan Selection
$\Delta\phi_{trig-prob} \geq 160$ degrees
Invariant Mass $M_{trig-prob} \geq 20$ GeV/c^2

Table B.2: Selection criteria for Drell-Yan electrons. The invariant mass requirement is imposed to remove J/Ψ, Υ resonances and to match the generation requirement of the MC sample.

Electron E_{T}	Isolation Requirement
$E_{\mathrm{T}} \leq 20$ GeV	Electron $E^{isol} \leq 2$ GeV
$E_{\mathrm{T}} \geq 20$ GeV	Electron $\frac{E^{isol}}{E_{\mathrm{T}}} \leq 0.1$

Table B.3: Isolation Requirements on the electron.

B.3 Results

Figure B.1 shows the invariant mass and $\Delta\phi$ distributions of the trigger and probe electrons. Figure B.2 shows the probe electron E_{T} distribution before and after ID requirements. The

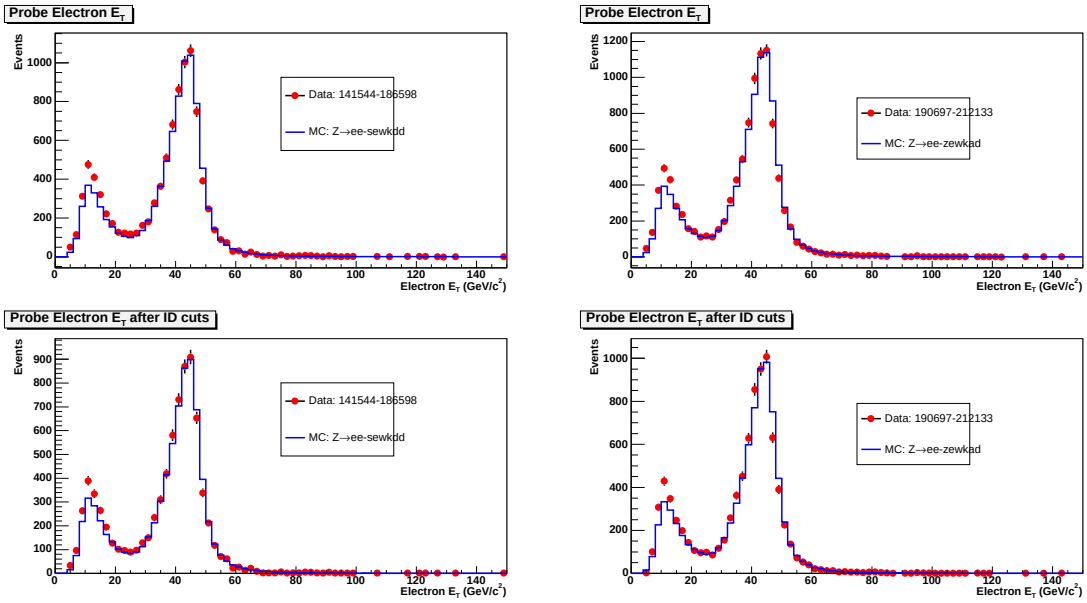

Figure B.2: Figure shows the E_{T} distributions before (top) and after(bottom) ID requirements on probe have been made in two subsamples of data and MC. Same-sign events are subtracted in both. The E_{T} distributions are normalized to number of events between 30 and 60 GeV. Invariant mass ≥ 20 GeV/c^2 and $\Delta\phi \geq 160$ degrees have already been required.

ID efficiency/scale-factor for different E_{T} bins is shown in Table B.4, B.5 with the combined numbers in Table B.6.

E_{T} GeV	Data ϵ_{ID}	MC ϵ_{ID}	SF
8 - 20	0.848±0.008	0.836±0.001	1.015±0.01
$\geq$ 20	0.847±0.004	0.837±0.001	1.012±0.005

Table B.4: The ID efficiency/scale-factor for different E_{T} bins.

After evaluation of systematic uncertainties (Table B.7) as described in Ref. [32], the final scalefactor for $8 < E_{\mathrm{T}} < 20$ is : SF $= 1.0102 \pm 0.0122(\mathrm{stat}) \pm 0.0242(\mathrm{syst})$.

E_{T} GeV	Data ϵ_{Iso}	MC ϵ_{Iso}	SF
8 - 20	0.914±0.007	0.918±0.001	0.995±0.007
$\geq$ 20	0.979±0.002	0.977±0.001	1.002±0.002

Table B.5: The Iso efficiency/scale-factor for different E_{T} bins.

E_{T} GeV	Data ϵ	MC ϵ	SF
8 - 20	0.7753±0.0092	0.7674±0.0013	1.0102±0.0122
$\geq$ 20	0.8292±0.0042	0.8176±0.0005	1.014±0.0053

Table B.6: The complete (ID/Iso) efficiencies and scalefactor (SF)

Source	Error (%)
Effect of "all-but-one"	1.7
Effect of isolation	1.7

Table B.7: Sources and systematic errors considered.

Appendix C

Trigger Efficiencies

The efficiency of the SUSY dielectron trigger is obtained by first calculating the efficiency of a single electron based on its E_{T} . Then two such electrons are required, and their combined efficiency is calculated as $\epsilon_1 \times \epsilon_2$. The single electron term is given by

$$\epsilon = 0.5 \times p_2 \times (1 + Erf(0.5\frac{E_{\mathrm{T}} - p_0}{p_1})) \tag{C.1}$$

with $p_0 = 3.924$, $p_1 = 1.515$, and $p_2 = 0.9692$, and errors $\delta p_0 = 0.139$, $\delta p_1 = 0.099$, and $\delta p_2 = 0.0015$.

In a similar way, one term of the dimuon trigger efficiency is given by

$$\epsilon = \frac{p_0^i}{1 + e^{p_1^i - \frac{p_{\mathrm{T}}}{p_2^i}}} \tag{C.2}$$

where i is the Level and with the parameters as follows

for CMU muons at Level 1: $p_0 = 0.956, p_1 = 1.938, p_2 = 0.784$, Level 2: $p_0 = 0.994, p_1 = 0.883, p_2 = 0.780$, Level 3: $p_0 = 1.002, p_1 = 3.174, p_2 = 0.402$. The efficiency at each level is multiplied to obtain the total efficiency. The CMX parameters are at Level 1: $p_0 = 0.968, p_1 = 0.461, p_2 = 0.977$, Level 2: $p_0 = 0.999, p_1 = 2.362, p_2 = 1.783$, Level 3: $p_0 = 1, p_1 = -0.656, p_2 = 0.626$. There is a 5% error on the total efficiency of each term.

The High p_{T} electron trigger efficiency is given by

$$\epsilon_{level2} = 1 - 59106 \times e^{-0.7E_{\mathrm{T}}} \tag{C.3}$$

with $\epsilon_{level3} = 1.0$, and $\epsilon_{tracking} = 0.98$. The total efficiency is the product of the three terms.

The High p_{T} muon trigger efficiency is $\epsilon_{CMUP} = 0.9073 \pm 0.005$, and $\epsilon_{CMX} = 0.9050 \pm 0.005$. These efficiencies have been corrected for dynamic prescales.

All the efficiency numbers are obtained from various measurements described in Ref. [30].

References

[1] W.-M. Yao *et al. J. Phys. G* **33** (2006).

[2] *Quarks and Leptons.* John Wiley and Sons, Inc., 1984.

[3] *Gauge Theories of the Strong, Weak, and Electromagnetic Interactions.* Addison-Wesley, Reading, MA, 1983.

[4] R. Cahn *Rev. Mod. Phys* **68**.

[5] *Supersymmetry in Particle Physics.* Cambridge University Press, Cambridge, UK, 2007.

[6] S. P. Martin, "A Supersymmetry Primer," `hep-ph/9709356`.

[7] H. Haber and G. Kane *Phys. Rept.* **117**.

[8] G. Farrar and P. Fayet *Phys. Lett. B* **76**.

[9] A. Chamseddine, R. Arnowitt, and P. Nath, "Locally Supersymmetric Grand Unification," *Phys. Rev. Lett.* **49** (1982).

[10] V. Barger *et al.*, "Report of the SUGRA Working Group for Run II of the Tevatron," `hep-ph/0003154`.

[11] H. Baer *et al.* `hep-ph/0312045`.

[12] W. Beenakker *et al. Phys. Rev. Lett.* **83** (1999).

[13] J. Glatzer, "Probing msugra with a search for chargino-neutralino production using trileptons," Master's thesis, Rutgers Univeristy, 2008.

[14] J. Zhou *et al.*, "Searches for Chargino-Neutralino Production in mSUGRA Model in a Dielectron + Track Channel." CDF internal note, cdf7478.

[15] D. Hooper, T. Plehn, and A. Valinotto, "Neutralino Dark Matter and Trilepton Searches in the MSSM," `hep-ph/0801.2539`.

[16] LEP SUSY Working Group. `http://lepsusy.web.cern.ch/lepsusy/`.

[17] A. Lipniacka, "Can SUSY be found at Tevatron Run II?," `hep-ph/0112280`.

[18] T. Aaltonen *et al.*, "Search for Chargino-Neutralino production in $p\bar{p}$ collisions at $\sqrt{s} = 1.96$ TeV," *Phys. Rev. Lett.* **99** (2007).

[19] V. Abazov *et al.*, "Search for Supersymmetry via Associated Production of Charginos and Neutralinos in Final States with Three Leptons," *Phys. Rev. Lett.* **95** (2005).

[20] **DØ** Collaboration, "Public results." `http://www-d0.fnal.gov/Run2Physics/WWW/results/np.htm`.

[21] **CDF II** Collaboration, R. Blair *et al.*, "The CDF II detector: Technical design report,". FERMILAB-PUB-96-390-E.

[22] **CDF** Collaboration, A. Abulencia *et al. J. Phys. G: Nucl. Part. Phys.* (2007).

[23] **CDF** Collaboration, A. A. Affolder *et al.*, "CDF central outer tracker," *Nucl. Instrum. Meth.* **A526** (2004) 249–299.

[24] S. Kuhlmann *et al.*, "The CDF calorimeter upgrade for Run IIB," *Nucl. Instrum. Meth.* **A518** (2004) 39–41, `physics/0310155`.

[25] A. Artikov *et al.*, "Design and construction of new central and forward muon counters for CDF II," *Nucl. Instrum. Meth.* **A538** (2005) 358–371, `physics/0403079`.

[26] **CDF** Collaboration, D. Acosta *et al.*, "The CDF Cherenkov luminosity monitor,".

[27] G. Gomez-Ceballos *et al.*, "Event Builder and Level 3 at the CDF Experiment," *Nucl. Instrum. Meth.* (2004).

[28] W. Sakumoto, "Event $|z_{vtx}| < 60$ Cut Acceptance for Run 2." CDF internal note, cdf8318.

[29] **CDF** Collaboration, A. Bhatti *et al.*, "Determination of the jet energy scale at the Collider Detector at Fermilab," *Nucl. Instrum. Meth.* **A566** (2006).

[30] "PerfIDia." `http://ncdf70.fnal.gov:8001/PerfIDia/PerfIDia.html`.

[31] S. Dube *et al.*, "Low E_{T} electron ID efficiency and scale-factors using J/Ψ." CDF internal note, cdf7379.

[32] S. Dube *et al.*, "Medium E_{T} electron identification efficiency and scale-factors." CDF internal note, cdf8321.

[33] G. Manca *et al.*, "Central Electron ID Efficiencies at Medium Energy." CDF internal note, cdf7233.

[34] C. Hill *et al.*, "Electron Identification in Offline Release 5.3." CDF internal note, cdf7309.

[35] C. Mills *et al.*, "Electron Identification in Offline Release 6.1.2." CDF internal note, cdf7950.

[36] V. Rekovic *et al.*, "Low p_{T} Muon Isolation Efficiency and Scale Factors." CDF internal note, cdf7432.

[37] V. Martin, "High-Pt Muon ID Cuts and Efficiencies for use with 5.3.1 Data and 5.3.3 MC." CDF internal note, cdf7367.

[38] E. Lytken *et al.*, "Intermediate pt muon ID efficiencies with the 1 fb^{-1} dataset." CDF internal note, cdf8336.

[39] A. Attal and A. Canepa, "Photon Conversion Removal Efficiency." CDF internal note, cdf8073.

[40] CDF Data Quality Monitoring, "Goodrun list v18." `http://www-cdf.fnal.gov/internal/dqm/goodrun/good.html`.

[41] T. Sjöstrand *et al.*, "High-energy physics event generation with PYTHIA," *Comput. Phys. Commmun.* **135** (2001).

[42] F. Maltoni and T. Stelzer *J.High Energy Phys.* **0302**.

[43] R. Brun and F. Carminati *CERN Program Library Long Writeup W5013* (1993).

[44] **CTEQ** Collaboration, H. Lai *Eur. Phys. J. C* **12**.

[45] S. Hsu *et al.*, "Search for ZZ in the 4 lepton and dilepton + MET channel and update of WZ in the trilepton +MET." CDF internal note, cdf8924.

[46] B. Jayatilaka *et al.*, "Measurement of the top quark mass in the dilepton channel with the Matrix-Element Method." CDF internal note, cdf9098.

[47] T. Junk *Nucl. Instrum. Methods A* **434** (1999).

[48] A. Read *J. Phys. G* **28** (2002).

[49] "ROOT TGraphDelaunay Class." `http://root.cern.ch/root/html508//TGraphDelaunay.html`.

[50] S. Dube, J. Glatzer, S. Somalwar, and A. Sood, "An Interpretation of Tevatron SUSY Trilepton Search Results in mSUGRA and in a Model-independent Fashion," `hep-ph/0808.1605`.

[51] W. Badgett *et al.*, "The CDF Run II Event Structure." CDF internal note, cdf4152.

[52] A. Safonov *et al.*, "Measurement of the electron trigger efficiencies for Level 1 and Level 2 8 GeV triggers." CDF internal note, cdf6257.

Vita

Sourabh Dube

Education

2002-2008	Ph.D. in Physics Rutgers, the State University of New Jersey New Brunswick, New Jersey
1998-2001	B.Sc. in Physics Fergusson College Pune, India

Significant publications

1. CDF collaboration, "Search for Supersymmetry in $p\bar{p}$ Collisions at $\sqrt{s} = 1.96$ TeV using the Trilepton Signature of Chargino-Neutralino Production", submitted to Phys. Rev Lett. August 2008, arXiv:0808.2446 [hep-ex].

2. **Sourabh Dube**, Julian Glatzer, Sunil Somalwar, Alexander Sood, "Interpretation of Tevatron SUSY trilepton results in mSUGRA and in a model-independent fashion", arXiv:0808.1605 [hep-ph].

3. CDF collaboration, "Search for Chargino-Neutralino Production in $p\bar{p}$ Collisions at $\sqrt{s} = 1.96$ TeV", Phys.Rev.Lett. **99**, 191806